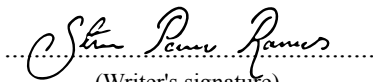




University of
Stavanger

Faculty of Science and Technology

MASTER'S THESIS

Study program/ Specialisation: Mathematics and Physics/ X-ray physics	Spring semester, 2016 Open access
Writer: Stian Penev Ramsnes	 (Writer's signature)
Faculty supervisors: Gunnar Thorkildsen, Helge Bøvik Larsen	
Thesis title: Aspects of X-Ray Diffraction Using <i>Mathematica</i>	
Credits (ECTS): 60 points	
Key words: X-ray diffraction phase transition data processing thiourea-ferrocene <i>Mathematica</i> reticular merohedry structure analysis	Pages: 76 + enclosure: 38 Stavanger, 15th June 2016

Abstract

A specialised *Mathematica* package has been launched, which is intended to become a valuable tool in our line of work. Old and new code has been compiled to a single, organised and flexible package, featuring a neat documentation on usage.

Theoretical foundations of X-ray diffraction and structural analysis has been examined in the thesis and connected with experimental data. A function has been written to make calculations of structure factors and quantities relevant to the dynamical theory of diffraction as accessible as possible. Comparison with the crystallographic literature has verified the output to be in accordance with the selected sources.

The thesis has largely been devoted to an investigation of thiourea-ferrocene inclusion compounds subjected to cold temperatures. An initial analysis, involving only data at room temperature, was conducted in order to obtain accurate parameters of the diffractometer's instrument model, which was used in the following analyses.

A systematic investigation of the reciprocal space of the thiourea-ferrocene crystals has been carried out, in addition to solving the structure of both ferrocene and thiourea-ferrocene.

Preface and acknowledgements

The work with my thesis has given me broader understanding of the dynamics and terminology of the field, and I have gained experience with treatment of data from diffraction experiments and encountered some of the challenges that comes with this line of work. Many hours have also been devoted to the development of an X-ray themed *Mathematica* package, which is an extension of earlier work by professors Gunnar Thorkildsen and Helge Bøvik Larsen combined with my own code for the various topics met so far.

Dynamical theory has mainly been learned from the book of Authier^[1]. For convenience, equations taken from his book have two labels – one referring to his book and another for this thesis.

For clarity, a styling convention has been adopted throughout the text where names of software are in italics, numbers from calculations are typed in the *Latin Modern Roman* font (default in L^AT_EX) and programming code in the *Courier* font. Quotes and special remarks are enclosed in guillemets, while double quotes are used for ironic or imprecise wordings. Finally, references to menus and tabs inside software are printed in their own formatted environments.



I am immensely grateful for professor Thorkildsen's fantastic guidance and inspiring dedication to the subject, and whose expertise and advice has been invaluable. I have also had the enviable opportunity to visit the synchrotron facility in Grenoble, France, for which I am thankful to the University of Stavanger. The trip would never had been the same without the company of Larsen, Thorkildsen and David Graham Nicholson, all of whom it has been an absolute joy to work together with.

Gratitude is also in order for Nils Henrik Kolnes and Dan Erik Ramsnes for showing genuine interest in my thesis and helping out with proofreading.

Nevertheless, the most important person has always been my fiancée, Lena Marie Sola, whose love, support, kindness and sincere concerns for my well-being has always been greatly appreciated.

Table of contents

Abstract	ii	3.5 Crystal 4	59
Preface and acknowledgements	iii	3.5.1 Investigation of the reciprocal space . . .	60
Table of contents	iv	3.5.2 Solving the thiourea-ferrocene structure .	61
1 Introduction	5	3.6 Crystals 7 and 8	64
2 Theory	6	3.7 Crystal 9	65
2.1 Scattering and the structure factor	6	3.7.1 Investigation of the reciprocal space . . .	65
2.1.1 The kinematical theory of diffraction . .	7	3.7.2 Solving the thiourea-ferrocene structure .	67
2.2 The dynamical theory of diffraction	9	4 Discussion	68
2.2.1 Fundamental equations	10	4.1 Challenges with <i>CrysAlis</i>	68
2.2.2 The two-beam case	11	4.2 Thiourea-ferrocene	69
2.2.3 Pendellösung and Darwin width	13	4.2.1 Temperature's impact on parameters . . .	69
2.3 Data acquisition and relevant software	16	5 Conclusion	75
2.3.1 Structure analysis	16	5.1 Future work	76
2.3.2 Instrumentation setup	21	6 Appendices	77
2.3.3 An overview of the <i>CrysAlis</i> software . . .	25	6.1 Appendix A – <i>Mathematica</i> documentation	77
2.4 Ferrocene and thiourea-ferrocene	29	StructureFactorTable	79
2.4.1 Ferrocene	29	ReflectionConditionCheck	86
2.4.2 Thiourea-ferrocene	30	RefinedValues	93
3 Analysis	32	6.2 Appendix B – Details of the <i>CrysAlis</i> procedures .	95
3.1 Silicon data	32	6.2.1 Silicon data processing	95
3.1.1 Comparing calculations with literature .	32	6.2.2 Room temperature data treatment	97
3.1.2 Intensity comparison	35	6.2.3 Investigation of crystals 1 and 4	98
3.2 Thiourea-ferrocene room temperature analysis . .	38	6.3 Appendix C – Miscellaneous	100
3.3 Ferrocene	41	6.3.1 Alternative silicon intensities	100
3.3.1 Further inspection of crystal 3	43	6.3.2 ReflectionConditionCheck . .	101
3.3.2 Structure solution	45	List of symbols	103
3.4 Thiourea-ferrocene – crystal 1	47	List of figures	105
3.4.1 Room temperature reconstructions	49	List of tables	106
3.4.2 Twinning of crystal 1	50	References	107
3.4.3 Low temperature inspection	52	Index	112
3.4.4 Finer sampling of reciprocal space	54		
3.4.5 The modulation patterns	55		

Chapter 1

Introduction

Starting out with the title «*n*-beam diffraction using *Mathematica*», the thesis was at the outset about combining dynamical theory of X-ray diffraction with use of the computation program *Mathematica* by Wolfram Research. The first months were committed to building a thorough theoretical understanding along with a numerical treatment of experimental data on silicon crystals.

X-ray diffraction data previously gathered at the *European Synchrotron Radiation Facility* (ESRF) was provided for analysis with the *CrysAlis^{Pro}* software by Rigaku Oxford Diffraction[†]. This served in part as a preparation for my visit to the facility in November 2015 where I joined professors Thorkildsen, Larsen and Nicholson in the studies of encapsulated ferrocene and multiple-beam diffraction. I was primarily involved in assisting with the latter experiment, which aim was to study coherent multiple beam interactions in light-atom organic crystals and determine its chirality by studying intensity perturbations during an emulated ψ -scan.

Some challenges arose in the multiple-beam project. The Glycyl-L-alanine crystals appeared to be twinned, rendering them unfit for the project. Emulating the desired ψ angle from the three available rotations on the instrument also proved to be a mechanical difficulty. Furthermore, a night's worth of data collection was lost due to a technical computer error. On the other hand, we had obtained great results from the first thiourea-ferrocene project. After returning from Grenoble November 10th 2015, focus has been on these data sets.

This thesis consists of three main parts:

- I. **Dynamical theory of diffraction** – An introduction to key concepts in connection with analysis of silicon.
- II. **Structural analysis of thiourea-ferrocene**
- III. **X-ray computation package** – Useful tools and functions have been developed and organised into a robust *Mathematica* package.

The thesis starts with a theoretical chapter, with an introduction intended mainly for a review of central quantities and notation. Thereafter comes a section on fundamental dynamical theory of X-ray diffraction. The purpose of this element is to shine light at characteristic observations related to highly perfect crystals and the underlying physical mechanisms. The last theoretical sections are concerned with the framework of structure analysis, as well as background information on the thiourea-ferrocene compound. The relevant observations and descriptions of what has been done are to be found in the analysis chapter.

The common thread in the thesis is structure analysis via X-ray diffraction. We measure intensities and proceed to calculate structure factors either in the dynamical or kinematical regime. The temperature varying thiourea-ferrocene experiment falls in the category of standard diffraction experiment. This compound has been studied since the 1970's and the crystal structure determined, but there haven't been any substantial crystallographic studies that follow the cooling processes.^[2, p. 236] Detailed calorimetric studies have been undertaken by Sorai et. al^[3] in 1981 that revealed six phases of thiourea-ferrocene in the temperature range 120 K to 240 K. The intention with our studies is to investigate the effect of cooling from a crystallographic point of view.

[†] Agilent Technologies used to have a part in *CrysAlis*.

Chapter 2

Theory

2.1 Scattering and the structure factor

X-rays are electromagnetic waves with wavelength in the order of 1 \AA . The radiation interacts with matter by exciting the electrons, effectively making them oscillate and behave like dipoles. When a crystalline medium is subjected to a time-varying external electromagnetic field, a time-varying polarisation is induced. Since an oscillating charge gives rise to so-called electric dipole radiation we have what is termed a scattering process.^[4]

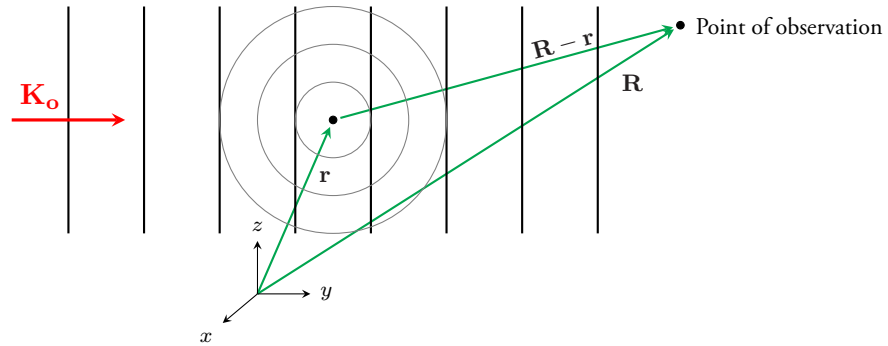


Figure 2.1: An incoming plane wave in the \mathbf{K}_o direction interacts with a point scatterer at position \mathbf{r} and a secondary spherical wave with the same frequency emerges (for elastic scattering). This re-radiated wave was called a *wavelet* by Ewald.^[5] $|\mathbf{R}| = R$ measures the radial distance from the scattering centre.

For N point scatterers the individual scattered waves are superimposed at the point of observation:

$$\Phi_h = \Phi_o \frac{\zeta}{R} \sum_{n=1}^N \exp(2\pi i \mathbf{k} \cdot \mathbf{r}_n). \quad (2.1)$$

Φ_h and Φ_o are the amplitudes of the scattered and incoming plane waves, respectively. ζ is the *scattering length*, a measure of the interaction and the physical process generating the new wave. It depends on the nature of radiation, and is in the case of electric dipole radiation given by:^[4]

$$\zeta = -r_e C, \quad (2.2)$$

where r_e is the classical electron radius and C the polarisation factor. The minus sign indicates a 180° phase shift with respect to the incoming wave. The *scattering vector*, \mathbf{k} , is defined by:

$$\mathbf{k} = \mathbf{K}_h - \mathbf{K}_o. \quad (2.3)$$

Figure 2.2 shows the geometrical construction of \mathbf{k} .

The sum in (2.1) is in principle over every scatterer within the crystal. Since (perfect) crystals have a regularly repeated structure, we basically need to consider the *unit cell* and its constituents only. The position vector in real

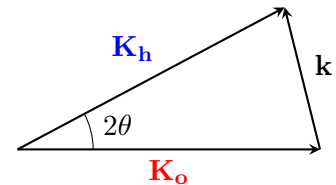


Figure 2.2: The scattering geometry. Note that the triangle is isosceles if we have elastic scattering. θ is the Bragg angle.

space \mathbf{r}_n will therefore be decomposed into

$$\mathbf{r}_n = \mathbf{r}_k + \underbrace{n_1 \mathbf{a} + n_2 \mathbf{b} + n_3 \mathbf{c}}_{\text{all the unit cells}}, \quad (2.4)$$

where \mathbf{r}_k represents all the scattering centres within the unit cell, n_1 , n_2 , and n_3 are arbitrary integers, and \mathbf{a} , \mathbf{b} and \mathbf{c} are the basis vectors of the Bravais lattice. To describe the scattering from the unit cell we further define:

$$F_H = \sum_{n=1}^N f_n \exp(2\pi i \mathbf{h} \cdot \mathbf{r}_n) = \int_{\text{unit cell}} \rho_n(\mathbf{r}) \exp(2\pi i \mathbf{h} \cdot \mathbf{r}) dV. \quad (2.5)$$

as the *structure factor*, where \mathbf{h} is the *reciprocal lattice vector* associated with reciprocal lattice node H . The so-called *atomic scattering factor* (or *atomic form factor*), f_n , has also been introduced, and is a measure of the scattering ability associated with the n 'th of the N atoms or constituents in the unit cell. In view of the probabilistic nature of quantum mechanics, the electrons are not simply confined to single points. We therefore replace the point scatterers in the unit cell with an *electron density distribution* $\rho_n(\mathbf{r})$, associated with atom n . Also note from (2.5) that the structure factors are related to the electron density by inverse Fourier transformations.

The structure factor is generally a complex quantity;

$$F_H = |F_H| \exp(i\phi_H). \quad (2.6)$$

$|F_H|$ denotes the amplitude and ϕ_H the phase characterised by the lattice node H . It is a function that is essential to the description of scattering from crystal structures as its amplitude is directly related to the diffracted intensities we measure. It is either directly proportional to the modulus of the structure factor, $|F_H|$, or its square, $|F_H|^2$, depending on the underlying diffraction theory.

In short, the amplitude of a diffracted wave depends on the number of electrons in an atom, and the phase depends on where the atom is positioned in the unit cell.^[6] Since the X-ray detectors do not measure the relative phases, the experimental data are incapable of assembling a complete picture of the diffraction. Several methods have been developed to overcome this problem and a brief account on this is given in section 2.3.

2.1.1 The kinematical theory of diffraction

Max von Laue is known for the discovery of X-ray diffraction. He argued that since the wavelength of X-rays were close to the lattice parameters in size, interference due to diffraction would occur in a manner similar to light interferences in optical gratings. This was verified experimentally in 1912 by Paul Knipping and Walter Friedrich, thus providing evidence for the lattice arrangement of atoms in crystals.^[5]

In Laue's *kinematical theory of diffraction* (or *geometrical theory*), it is assumed that the incoming photons are only scattered once, and that the interactions between the diffracted waves and the crystalline matter may be neglected. Therefore, we may further assume that the amplitude incident on every atom is the same (see Figure 2.7a).^[5] By taking the Fourier transform of the density distribution of scattering centres (in direct space), we get the distribution of the diffracted amplitudes in reciprocal space.^[7] The term *kinematical approximation* is used to emphasise that the theory is an approximation of the scattering phenomenon. It is in fact a first Born approximation, i.e. the scattered wave amplitude is considered to be negligible compared to that of the incoming wave, and the subsequent rescattered waves even more so.^[8]

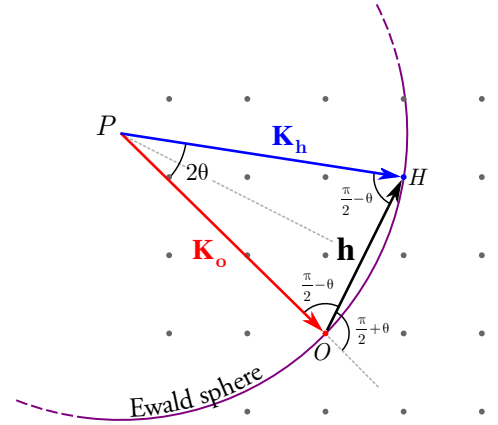


Figure 2.3: A two-dimensional cross section of the Ewald sphere corresponding to the scattering plane, which is defined by \mathbf{K}_o and \mathbf{K}_h . O defines the origin of the reciprocal space, and H is the reciprocal lattice node associated with reflection hkl . P is the tie point in the dynamical theory (see the next section). The radius of the sphere is equal to $1/\lambda$.

Although Laue derived an expression for the amplitude of the wave diffracted from an arrangement of atoms, the Braggs derived a simpler equation, known as *Bragg's law*, for describing the condition for producing a diffraction pattern. In essence, Bragg's law states that if the relation between the lattice spacing and orientation of the incident radiation is such that waves are in phase when reflected off a family of parallel lattice planes, constructive interference occurs and the diffraction patterns emerge. The requirement for constructive interference can also be seen geometrically through *Ewald's construction*. We have constructive interference when the incident and diffracted wave vectors are situated in reciprocal space in a way such that the scattering vector equals a reciprocal lattice vector in contact with the Ewald sphere (see Figure 2.3). If this is fulfilled, then $\mathbf{k} = \mathbf{h}$. Considering the isosceles triangle *OHP* in Figure 2.3 we may find:

$$|\mathbf{K}_o + \mathbf{h}|^2 = |\mathbf{K}_h|^2 \implies 2d_{hkl} \sin \theta = n\lambda. \quad (2.7)$$

This is *Bragg's law*. d_{hkl} is an *interplanar spacing* of the crystal, λ is the wavelength, and θ is called the *Bragg angle*, which is the angle between the wave vector of the incident plane wave and the lattice planes (see Figure 2.4). Since the phase differences between the scattered waves have to be an integer multiple of the wavelength for constructive interference to happen, we include an *order of reflection*, n , in Bragg's law.

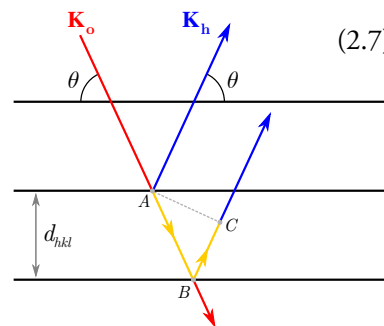


Figure 2.4: Bragg diffraction in direct space. The incoming radiation is represented by a beam \mathbf{K}_o which is scattered at *A* and *B*. In order for the two reflected beams to be in phase (and interfere constructively) the path $AB + BC$ must equal an integer multiple of the wavelength.

Diffraction

The ability to resolve optical details is fundamentally limited by diffraction, with less diffraction being preferable (narrower diffraction pattern). The crystal, which effectively acts as a diffraction grating, has to be irradiated using a wavelength comparable to the interatomic distances. This fundamental limitation can be seen with Ewald sphere – since the radius decreases as the wavelength increases, there will be a certain wavelength making the sphere so small that no neighbouring reciprocal lattice nodes fall within it, preventing Bragg's condition to be fulfilled. This wavelength corresponds to the maximum interplanar distance in the crystal. The arrangement of atoms make up the scattering planes, illustrated in Figure 2.4.

It seems logical that gamma rays with even shorter wavelengths would be suitable for this task. These are, however, «difficult to produce in large numbers, difficult to focus, and interact too strongly with matter, producing particle-antiparticle pairs.»^[9] If one hopes that gamma rays will enable us to “see” atoms, another point to take into consideration is that «the illumination intensity required to see the individual atoms in a molecule is a many orders of magnitude larger than the energy required to evaporate the sample.»^[10, p. 3042]

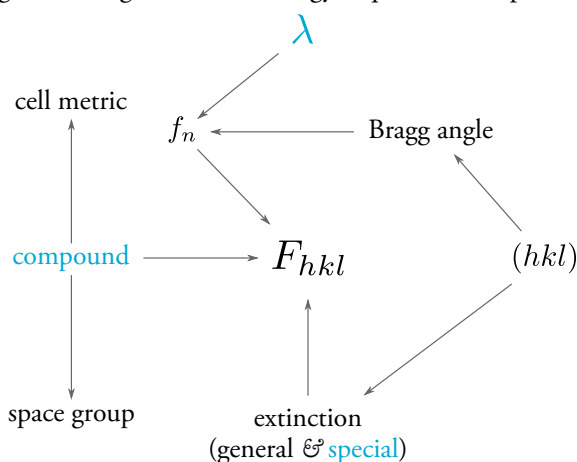


Figure 2.5: A schematic diagram showing what quantities are involved in the structure factor computation. In order to make the function as versatile as possible, the quantities in blue will be input variables. The other information will be collected from data files (included in the *Xray* package) or calculated in the process.

Mathematica function

It is convenient to have a function in *Mathematica* that calculates theoretical values of the structure factor. Such a function would require the input information shown in Figure 2.5. There are also some quantities that are of importance in dynamical theory, including the *Pendellösung distance* and *Darwin width*. These will also be calculated along with the structure factor, but further remarks on this function will be on hold until these concepts are introduced in subsection 2.2.2.

2.2 The dynamical theory of diffraction

Key differences between the kinematical- and the dynamical theory of diffraction

The difference between the two theories is that so-called *multiple scattering* is neglected in the kinematical approximation, or at least considered to add incoherently.^[8, p. 95] If the crystal is regular over a sufficiently large volume, a wave reflected off a given plane may be re-reflected off another plane, giving rise to multiple scattering. In the kinematical theory, the reflected waves will not experience any further interactions. Still, the incoming waves experience absorption in both theories. In the dynamical theory we may have realisation of the phenomena called *primary* and *secondary extinction* (see more on page 14). The kinematical theory is nevertheless a useful approximation for small crystals and when the interaction between the incident and the scattered waves can be neglected which is the case with very thin crystals, surface scattering and diffuse scattering.^{[11] [12, p. 72]}

The kinematical approximation also holds for so-called *mosaic crystals*, in which the grains are slightly tilted from another (see Figure 2.6). We denote a crystal as *ideally imperfect* when misorientation is large enough for the kinematical theory to be valid. The successive crystallites or blocks must be shifted enough for each of them to diffract different portions of the incident beam.^[1] If we irradiate large and highly perfect crystals, the amplitude of the diffracted waves become comparable with that of the incident beam, resulting in an interchange of energy between them that requires the use of dynamical theory.^[13] Real crystals may be in a condition that corresponds to a combination of the two theories, but usually the scattering comply very closely with one or the other extremes.^[8, p. 95]

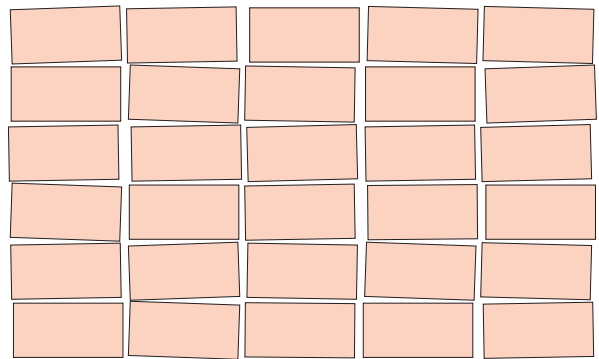


Figure 2.6: Visualisation of the grains or crystallites in a crystal making a mosaic.

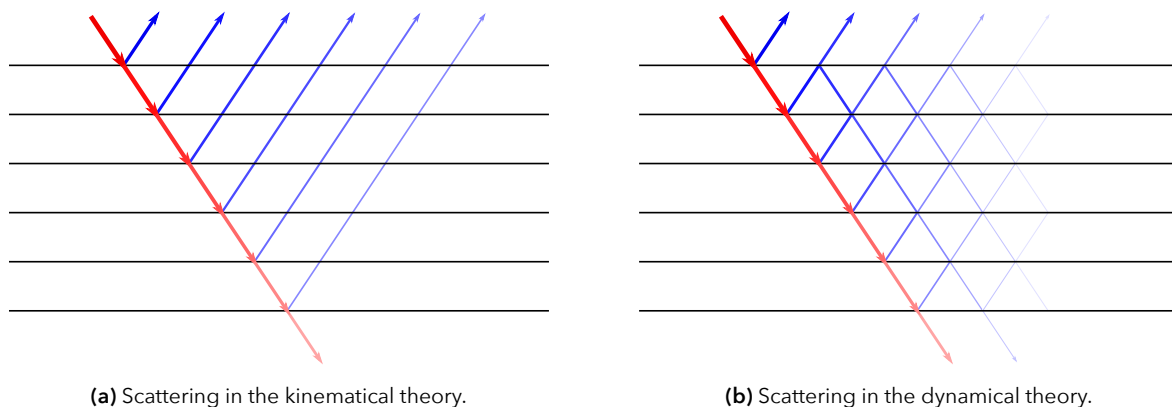


Figure 2.7: Conceptual predictions of how an X-ray beam would be transmitted through the lattice planes of a crystal in **(a)** the kinematical/geometrical theory and **(b)** the dynamical theory. We see that in the dynamical theory the reflected waves may be diffracted multiple times, which corresponds to there being multiple nodes on the Ewald sphere simultaneously (besides the origin).^[1] Notice that attenuation of the incident beam happens in both theories due to absorption, but that further reduction of the intensity is possible in the dynamical theory by rescattering of waves. The region of rediffraction shown in **(b)** will for trace out a triangle referred to as the *Borrmann fan*.

A shortcoming of Laue's original kinematical theory is that conservation of energy is not fulfilled, because the amplitude of the incoming wave does not attenuate from diffraction as it propagates through the crystal planes, even though reflected waves emerge from each plane. In fact, this theory predicts that if the crystal were infinitely large, the diffracted intensities would accumulate and become infinitely large as well.

2.2.1 Fundamental equations of the dynamical theory

Ewald's *dynamical theory of X-ray diffraction* is a continuation of his doctoral thesis, while Laue's dynamical theory is a reformulation from 1931.^[5]

When an electromagnetic plane wave impinges on a crystal, the incoming field sets the electrons into oscillation, effectively turning them into dipoles that are assumed to be in a three-dimensional array. The oscillating dipoles emit spherical waves, called *wavelets* by Ewald, and each wavelet contributes to the excitation of the other dipoles. The total wave propagating inside the crystal turns out to be a superposition of plane waves, and was called the *optical field* by Ewald and the *wave field* by Laue.^{[5][14]} Some authors also use «wave field» to refer to a single plane wave in the unified field.^{[13][15]}

Owing to the dipole-interaction, the phase velocity of the wave field differs from that of the wavelets (which propagate with the speed of light), and there appears an index of refraction.^[5] Authier^[1] states that «the aim of the theory is to find the possible positions of the *tie points* and therefore the wave vectors and the possible values of the index of refraction of the waves propagating in the crystal, as well as their amplitudes.» For now, it suffices to say that a tie point characterises the wave field.

In Laue's reformulation of Ewald's theory, the discrete distribution of single-point dipoles is replaced by a *continuous* distribution of electric charge throughout the crystal, being overall neutral. Additionally, the local electric charge and current densities are zero. As Tanner^[13] writes, our aim is now that «we require a solution of Maxwell's equations in a periodic medium matched to solutions which are plane waves outside the crystal.» Proceeding with Laue's method, one first derives the following propagation equation from Maxwell's equations:^[5]

$$\Delta \mathbf{D} + \text{curl curl } \chi \mathbf{D} + 4\pi^2 k^2 \mathbf{D} = 0, \quad (\text{Authier 2.55}) \quad (2.8)$$

where Δ is the Laplacian, \mathbf{D} the electric displacement, χ the dielectric susceptibility, and $k = 1/\lambda$ the wave number in vacuum. The reason for using the electric displacement field \mathbf{D} instead of the electric field \mathbf{E} , is because the divergence of \mathbf{D} is always zero, contrary to that of the electric field. This simplifies the description of the polarization states of the field inside the crystal.^[16] The electric displacement is also triply periodic and can be expanded in a Fourier series:

$$\mathbf{D} = \sum_{\mathbf{h}} \mathbf{D}_{\mathbf{h}} e^{-2\pi i \mathbf{K}_{\mathbf{h}} \cdot \mathbf{r}}, \quad \mathbf{K}_{\mathbf{h}} = \mathbf{K}_{\mathbf{o}} + \mathbf{h}. \quad (\text{Authier 4.6}) \quad (2.9)$$

The indexed \mathbf{D} 's are Fourier components of the electric field displacements, the indexed \mathbf{K} 's are *wave vectors* in the reciprocal space, and \mathbf{r} is a position vector. The summation is over all reciprocal lattice vectors (\mathbf{h} , \mathbf{g} etc.), and the common origin of the wave vectors is the tie point, P . Consequently we have that $\mathbf{K}_{\mathbf{o}} = \overrightarrow{PO}$, $\mathbf{K}_{\mathbf{h}} = \overrightarrow{PH}$, $\mathbf{K}_{\mathbf{g}} = \overrightarrow{PG}$ etc.^[1] † (see Figure 2.8b).

(2.9) is the solution of the wave equation (2.8). We can see that a given term in the summation is a plane wave multiplied by a periodic function – often defined as a *Bloch wave*. In this case the Bloch wave \mathbf{D} describes the wave field that propagates in the crystal, and may in principle consist of an infinite number of plane waves $\mathbf{D}_{\mathbf{h}}$.^[17]

The *dielectric susceptibility* χ can also be expanded in a Fourier series:

$$\chi = \sum_{\mathbf{h}} \chi_{\mathbf{h}} e^{-2\pi i \mathbf{h} \cdot \mathbf{r}}, \quad (\text{Authier 2.36}) \quad (2.10)$$

where $\chi_{\mathbf{h}}$ is the Fourier component of the dielectric susceptibility and is associated with reciprocal lattice vector \mathbf{h} ,

† It is to be noted that these definitions of the wave vectors are reversed in comparison with Authier's^[1] notation. The reason for this is to keep the notation in accordance with the definitions from subsection 2.1.1 and Ewald's construction. As a consequence, the minus sign of the $\mathbf{K}_{\mathbf{h}}$'s in (2.9) have been removed.

and is given by

$$\chi_h = -\frac{r_e \lambda^2 F_H}{\pi V}, \quad (\text{Authier 2.37}) \quad (2.11)$$

with V denoting the unit cell volume and λ the wavelength. Also, the summation in (2.10) is over all the reciprocal lattice nodes.

Substituting the series expansions (2.10) and (2.9) into (2.8), the result is an equation with an infinite sum of terms, which can be shown to be equivalent to a an infinite system of linear equations.^[1] Thus, the amplitudes \mathbf{D}_h satisfy a set of equations

$$\mathbf{D}_h = \frac{K_h^2}{K_h^2 - k^2} \sum_{h'} \chi_{h-h'} \mathbf{D}_{h'[h]}, \quad (\text{Authier 5.4}) \quad (2.12)$$

where the summations is over all reciprocal lattice vectors h' . The symbols represent the following:

- \mathbf{D}_h amplitude of a given wave, belonging to the wave field, with associated reciprocal lattice vector h ,
- K_h magnitude of the reflected wave vector,
- k wave number in vacuum (equal to $1/\lambda$),
- $\chi_{h-h'}$ Fourier coefficient of the polarisability associated with reciprocal lattice vector $h - h'$,
- $\mathbf{D}_{h'[h]}$ denotes the projection of $\mathbf{D}_{h'}$ onto the plane perpendicular to \mathbf{K}_h .

These equations relate the amplitude of a given wave in the wave field with the others, and have been called *fundamental equations of dynamical theory* by Laue.^[1]

In (2.12), the terms

$$\frac{1}{K_h^2 - k^2} \quad (2.13)$$

were called the *resonance factors* by Ewald. It is clear that in order for the terms in the wave field expansion (2.9) to have a non-negligible amplitude, the resonance factors must be such that $K_h^2 \approx k^2$. Geometrically, this corresponds to points in reciprocal space that are close to the Ewald sphere, or alternatively, the (tie) points that the wave vectors converge to if they are drawn *from* points on the Ewald sphere.

Going back to (2.8), we see that the propagation equation is a second order partial differential equation with a periodic interaction coefficient accounted for by the polarisability, which is a periodic function in the lattice. As mentioned, its solution is given by (2.9). From this we infer that the wave field is a superposition of plane waves with amplitude \mathbf{D}_h and wave vectors \mathbf{K}_h .^[7]

2.2.2 The two-beam case and the dispersion surface

If there are precisely two reciprocal lattice nodes in contact with the Ewald sphere simultaneously, where one of them defines the origin through the incident wave, we refer to it as a *two-beam case*. Then there are two waves that propagate inside the crystal and interfere to generate standing waves:^[5] the diffracted wave \mathbf{K}_h and the refracted wave \mathbf{K}_o . In context with (2.12), this corresponds to there being two significant resonance factors associated with the two nodes that simultaneously lie on the Ewald sphere. The fundamental equations reduce to the coupled equations:

$$\mathbf{D}_o = \frac{K_o^2}{K_o^2 - k^2} (\chi_o \mathbf{D}_o + \chi_h \mathbf{D}_h), \quad (2.14a)$$

$$\mathbf{D}_h = \frac{K_h^2}{K_h^2 - k^2} (\chi_h \mathbf{D}_o + \chi_o \mathbf{D}_h). \quad (2.14b)$$

This system of two linear and homogeneous equations has a non-trivial solution if and only if the determinant is zero. It can be shown that after rearranging and using $K_o \approx k$ and $K_h \approx k$, the determinant of these equations yields an equation for the so-called *dispersion surface*:^[1]

$$X_o X_h = \frac{k^2 \chi_h \chi_o}{4}, \quad (\text{Authier 4.15}) \quad (2.15)$$

where

$$\begin{aligned} X_o &\equiv \frac{K_o^2 - k^2}{2k} - \frac{k\chi_o}{2} \approx K_o - k \left(1 + \frac{\chi_o}{2}\right), \\ X_h &\equiv \frac{K_h^2 - k^2}{2k} - \frac{k\chi_h}{2} \approx K_h - k \left(1 + \frac{\chi_h}{2}\right). \end{aligned} \quad (\text{Authier 4.12, 4.13}) \quad (2.16)$$

Thus, the equations in (2.12) represent a set of eigenvalue equations. From (2.14) and (2.15), one may derive useful expressions such as the ratio of the amplitudes of the two waves in the wave field and coordinates of the tie points. A geometrical representation of the dispersion surface is shown in Figure 2.8.

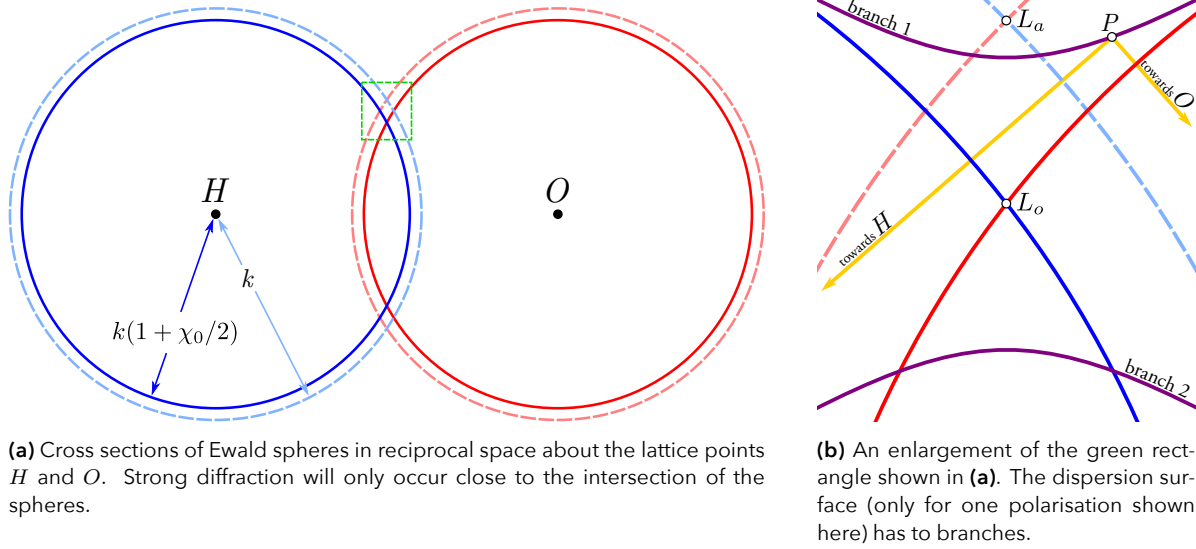


Figure 2.8: The tie point P is the common extremity of the wave vectors (in the two-beam case: \mathbf{K}_o and \mathbf{K}_h). L_a and L_o in (b) denote the so-called *Laue-* and *Lorentz points*, respectively. In the n -beam case, there will be $2n$ branches; two for each direction of polarisation.^[1] The solid and dashed lines correspond to σ - and π -polarisation, respectively. Based on figures by Authier^[1].

Exactly at the Bragg condition, the tie point P is situated on either of the apexes of the dispersion surface.^[18, p. 28]

The absolute *index of refraction*, n , is defined by:^[19]

$$n \equiv \frac{c}{v} = \sqrt{\frac{\varepsilon\mu}{\varepsilon_0\mu_0}}, \quad (2.17)$$

where c is the speed of light in vacuum, $v = \nu\lambda$ the *phase velocity*, ε the *permittivity*, and μ the *permeability* (subscript zero for vacuum). Neglecting magnetic interactions, $\mu \approx \mu_0$, and using the fact that χ is typically on the order of 10^{-5} to 10^{-6} , the index of refraction can be approximated with a Taylor series:^[1]

$$n \approx \sqrt{\frac{\varepsilon}{\varepsilon_0}} = \sqrt{1 + \chi_o} \approx 1 + \frac{\chi_o}{2}, \quad (2.18)$$

which is slight smaller than unity as χ is negative. As a result, the two concentric spheres (for each node) illustrated in Figure 2.8 have radii nk (innermost sphere) and k (outermost sphere). Refraction at the crystal surfaces arises due to interactions between the propagating wave and the matter.^[1] In the single-wave solution, i.e. when only a single plane wave in (2.12) has a significant amplitude, the fundamental equation will give us that $|\mathbf{K}_o| = nk$.^[20, p. 1115]

An infinitely large and perfect crystal should, in the kinematical theory, give rise to a single diffraction spot, due to its inverse relationship with crystal size. This is the Laue point in Figure 2.8b. The Lorentz point is the corresponding point for the waves with wave number nk . For an infinitely weak reflection, the dispersion surface would shrink to this point.

The position of the tie point P determines the direction of propagation as well as the relative ratios of amplitudes of the waves in the wave field. [1, p. 80]

2.2.3 Pendellösung and Darwin width

Crystal shape and the scattering geometry dictate the boundary conditions for the waves. [18, p. 29] Traditionally, there are two cases that we consider. See Figure 2.9 below.

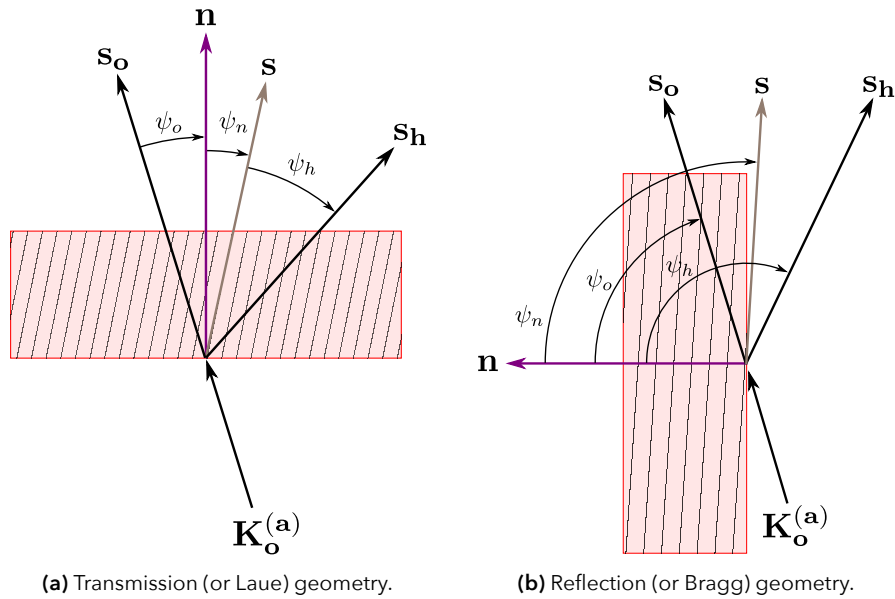


Figure 2.9: In the transmission geometry shown in (a) the reflected wave s_h is directed inwards to the crystal, and both branches of the dispersion surface are intersected. In the reflection geometry in (b), the reflected wave is directed away from the crystal, and intersects only branch at a time. [1]

The ψ 's in Figure 2.9 are angles as indicated. Note that the normal vector \mathbf{n} is in either case defined as being normal to the crystal surface, but directed inwards. s_o and s_h are the unit vectors in the incident and reflected directions. s is a unit vector parallel to the lattice planes. We define the *asymmetry ratio* as

$$\gamma = \frac{\gamma_h}{\gamma_o} = \frac{\cos(\psi_n - \theta)}{\cos(\psi_n + \theta)}. \quad (\text{Authier 4.24}) \quad (2.19)$$

We may recognise the geometry by noting that γ and γ_h are positive in the transmission geometry and negative in the reflection geometry. [1, p. 84]

In the Bragg geometry, we have the possibility of no tie points being excited, which corresponds to no intersection with either of the branches of the dispersion surface. If we don't consider absorption, the wave experiences total reflection. [20] The angular range where this happens is shown as a flat *Darwin plateau* in the reflection profile. The full width at half maximum of this peak is what we call the *Darwin width*, and is dependent on the *Pendellösung distance*,[†] Λ_o , defined by:

$$\Lambda_o = \frac{\pi V \sqrt{\gamma_o |\gamma_h|}}{r_e \lambda C \sqrt{F_H F_H^*}}, \quad (\text{Authier 4.26}) \quad (2.20)$$

[†] The quantity is called «Pendellösung distance» in the transmission geometry, and *extinction distance* in the reflection geometry.

where the symbols represent the following:

Λ_o	Pendellösung distance (or extinction distance)
V	unit cell volume
γ_o	cosine of the angle between the inward normal to the crystal surface and the incident direction
γ_h	cosine of the angle between the inward normal to the crystal surface and the reflected direction
r_e	classic electron radius
λ	wavelength
C	polarisation factor [†]
F_H	structure factor associated with reciprocal lattice node hkl
$F_{\bar{H}}$	structure factor associated with reciprocal lattice node $\bar{h}\bar{k}\bar{l}$

We now introduce:

$$\delta_{os} = \frac{\lambda}{\Lambda_o} \frac{|\gamma_h|}{\sin(2\theta)}, \quad (\text{Authier 4.26}) \quad (2.21)$$

with the real part of $2\delta_{os}$ being the Darwin width. It is the full width at half maximum of the rocking curve in the transmission geometry, and the width of the total reflection domain in the reflection geometry.^[1] In a perfect infinite crystal, dynamical theory predicts finite widths of the Bragg peaks instead of being delta functions. In the full dynamic limit, the intensities of the reflections are proportional to the Darwin widths instead.^[21]

In the Laue geometry, the beams are restricted within the Borrmann triangle (see Figure 2.7b). Shuffling of intensity back and forth between the forward transmitted beam and reflected beam give rise to a so-called *Pendellösung effect*.^[22]

Extinction

The Darwin width is named after Sir Charles Galton Darwin who also developed a dynamical theory of diffraction in 1914 and came up with the mosaic crystal model in 1922.^{[23]‡} In early experimentation on reflection of X-ray the observed intensities were always greater than expected from calculation. It was also found that disorienting a “fairly deep layer” of crystallites by polishing the crystal could increase the Bragg reflection.^[24] On page 9 it was mentioned that diffraction of mosaic crystals is not described by dynamical theory, because the slight misalignment of the mosaic blocks will inhibit the occurrence of multiple scattering. Thus we need highly perfect crystals to observe this effect. Darwin showed that the ideally imperfect mosaic crystal would be at least forty times as intense as a perfect crystal. In practice, crystals are in between the two extremes, but most crystals are comparatively imperfect.^[24]

Attenuation of the X-ray due to the photoelectric effect, incoherent (Compton) scattering and pair production are attributed to absorption, while intensity lost due to rescattering falls under extinction. If the mosaic blocks are significantly larger than the Pendellösung distance, the incident beam may be scattered more than once within the same block, i.e. multiple scattering effects, and we have what is called *primary extinction*. If we consider multiple blocks within the crystal that are very close to being parallel, the incident intensity will be less for the blocks further “down” the direction of transmission. This is referred to as *secondary extinction* and can mistakenly appear as photoelectric absorption.^[25, p. 182] Primary extinction diminishes the reflected beam because the rescattered waves tend to interfere destructively with the first beam.^[24] In an ideally imperfect crystal, both primary and secondary extinction is negligible. Crushing the crystal into a powdered form can prevent extinction effects altogether. Extinction tends to be observable for strong, low-angle reflections from crystals with a small degree of mosaicity. An indication of dynamical effects in play is that observed intensities are lower than those calculated from the proposed structure, especially for strong reflections.^[26, p. 117] The extinction distance is also of importance, as it limits the diffracting volume of the crystal.

[†] $C = 1$ (σ -polarisation; orthogonal component) or $C = \cos(2\theta)$ (π -polarisation; planar component).

[‡] Supposedly, it was Ewald who first suggested the name «mosaic». Darwin had used the term «conglomerate of crystalline blocks». ^[1, p. 8]

***Mathematica* function**

The function that is to calculate F_H , Λ_o , and $2\delta_{os}$ should have the following features:

1. Be able to generate an appropriate list of reflections.
2. Filter out reflections from said list that do not comply with the reflection conditions, also taking special rules into account.
3. Identify symmetry equivalent reflections, as they will all share the same value for the structure factor.
4. Delete impossible reflections that correspond to $\sin \theta > 1$.
5. Calculate the desired quantities for the remaining reflections.

With this in mind, `StructureFactorTable` has been created. Documentation on usage is found in appendix A. Please see subsection 3.1.1 for an example and comparison of computed values with literature.

2.3 Data acquisition and relevant software

2.3.1 Structure analysis

Diffraction data

The *Laue classes* are the 11 centrosymmetric point groups out of the total 32 crystallographic point groups. An important property of these classes is that all the non-centrosymmetric point groups are subgroups of these. Adding the symmetry operation of inversion to any point group will make it equivalent to one of the Laue classes.^[27] This is also a feature in every diffraction pattern, as long as the X-ray energy is not close to matching any absorption edges. If we also assume that all atoms diffract with the same relative phase, *Friedel's law* holds, i.e. the modulus of the structure factor associated with Miller indices hkl is equal to that with indices $\bar{h}\bar{k}\bar{l}$. When this is true, the symmetry of a diffraction pattern we may only distinguish between the 11 Laue classes. A general reflection (not lying on a symmetry element) may be used to generate all symmetry equivalent reflections by applying the symmetry operators of the Laue class point group.^[28] The process of determining the reciprocal cell parameters from the diffraction pattern is called *indexing*.^[29]

The further out the X-rays scatter (larger Bragg angles θ), the higher the *resolution* of the data set becomes. For a given maximum scattering angle θ_{\max} , there corresponds a minimum interplanar spacing d_{\min} that we can resolve in a diffraction pattern. From Bragg's law (2.7) we find:

$$d_{\min} = \frac{\lambda}{2 \sin \theta_{\max}} \quad (2.22)$$

The resolution is normally in the range from 0.5 Å to 3.0 Å[†]. Resolution is in theory limited by the wavelength of the X-rays; In practice by the crystal quality. The portion of the structure that is ordered for the longest range throughout the crystal will cause the reflections farthest from the axis of the incoming X-ray beam. Conversely, disorder in the crystal will lower the maximum scattering angle observed, thus also lowering the resolution. A drawback to high-resolution reflections is that intensity falls off at higher diffraction angles.^[30]

When symmetry equivalent reflections are merged we are left with a list of the *unique reflections*. Symmetry equivalence is defined by the Laue class. In diffraction experiments we define *completeness* as the percentage of unique reflections measured out of all possible. We also denote the average number of times each unique reflection (whether single or merged) has been measured as the *redundancy*,^[31] which may take a value up to the reflection multiplicity of the Laue class of the crystal. The term *outlier* is used to describe reflections that deviate significantly in intensity compared to symmetry equivalents. These may be removed or given lower weights in the refinement process.^[29]

Reciprocal lattice nodes are called *reflections* in association with diffractograms. Ideally, the scattering centres of the crystal would be aligned perfectly in planes, and would literally become points when Fourier transformed to the reciprocal space. In the real case, however, crystals are comprised of domains which are slightly misaligned with each other, usually in the range from 0.2° to 0.4° for a good crystal sample.^[32] This will basically keep certain lattice planes in reflection condition over some rotation interval about a goniometer axis, and the corresponding reflections appear elongated in the diffraction pattern. Assuming the orientations to follow a Gaussian distribution, a measure of this misalignment, the *mosaicity*, is normally assigned as its standard deviation.^[33] If the increment of the rotational angle is set to be greater than the effective mosaicity, the data sets are said to be *thick* or the slicing is *coarse*. Conversely, if the slicing is smaller than the width of a reflection it is called *fine*, and the data sets are called *thin*.^{[34][35]} We also describe the reflections in such circumstances as *partial* or *partially recorded*, and *fully recorded* if the spot comes entirely within a single diffractogram. Finer slicing is preferred as larger rotation steps result in increased X-ray background of the image as well as more saturated pixels and spatial overlaps of reflections.^[34]

[†] Lower numerical values for d_{hkl} are better and correspond to a higher (finer) resolution.

Phase transitions

The term *phase transition* is used to express the restructuring of a substance by varying external conditions such as temperature, pressure, magnetic field etc. A thorough study on the subject is out of the scope of this thesis, but the most relevant technical terms will be discussed briefly. A phase transformation is classified into either *first-* or *second order*. A first-order transition is a transition with latent heat and exhibits a discontinuity in the first derivative of the Gibbs free energy, which is reflected in thermodynamic quantities such as enthalpy and entropy.^[36] A fair amount of heat is either absorbed or released while the temperature of the system remains constant, with the melting of solids or vaporisation of liquids being familiar examples.^{[37][38]} A second-order transition (also known as *continuous phase transitions*) does not involve latent heat, but has discontinuities in the heat capacity (second derivative of Gibbs free energy).^[36] Common examples are the ferromagnetic transition to the paramagnetic state and transformation to and from chemical ordered state.^[38]

Some compounds, like Cu₃Au or brass (CuZn), can have the constituents occupying random lattice points (disordered structure) at a high-temperature phase, regardless of element type. If cooling causes the distinct elements to occupy the lattice points in a regular manner (ordered structure), we call it a *order–disorder transition*.^{[36][38]}

If displacements in the fundamental structure follow a periodic atomic displacement field, we have a *modulated crystal structure*. A modulation with a longer period than that of the underlying lattice gives rise to so-called *satellite reflections* around the fundamental reflections. Modulations with longer but still an integral number of the fundamental period may create a so-called *superlattice*.^[38]

Phase transitions can lead to a new structure whose periodicity cannot be expressed as an integral ratio of the original structure's periodicity. We then label the new structure as *incommensurate*.^[38]

Structure determination and direct methods

The process of determining the positional coordinates of the scatterers within the unit cell is called «structure determination» or «solving the structure», and usually includes describing the chemical structure as well as anisotropic displacement parameters.^[39] The measured intensities I_{hkl} are corrected for various effects from the geometry of measurement:

$$|F_{hkl}|^2 = I_{hkl} (y \cdot k \cdot Lp \cdot A)^{-1} \quad (2.23)$$

where y is an *extinction factor*, k a scaling factor, Lp the *Lorentz-polarisation correction*, and A the *absorption factor*. Effects related to multiple beam scattering are ascribed to the extinction factor. Reflections that spend a longer time crossing the Ewald sphere will be attributed a higher intensity, and an equalisation of this is the purpose of the Lorentz factor.^[40] Radiation will be partially polarised on reflection from a monochromator crystal and its intensity reduced by some factor that depends on the Bragg angle. At synchrotron beamlines, the polarisation is exclusively in the plane. The Lorentz and polarisation factors are normally applied as a single correction factor, Lp .

The best way to handle absorption would be to first identify the crystal faces and dimensions, then apply corrections after calculating the various path lengths through the crystal. Spherical crystals have the advantage of having a more uniform absorption correction.^{[40][41]} There are also numerical solutions that are based on the intensity variation of certain intense Bragg reflections during a rotation experiment.^[40, p. 65] In contrast to the absorption corrections of the raw data, extinction corrections are usually incorporated as part of the structure refinement.^[26, p. 127] Other factors to bear in mind are the decay of the synchrotron beam over time and potential degeneration of the crystal.

The notorious phase problem in crystallography is in practice circumvented by techniques such as statistical methods or iterative refinement, collectively known as *direct methods*. Another tool of historical importance is the *Patterson function*:

$$P(\mathbf{r}) = \frac{1}{V} \sum_H |F_H|^2 \exp(-2\pi i \mathbf{h} \cdot \mathbf{r}), \quad (2.24)$$

which is a Fourier series based on the intensities rather than the structure factors. The distances from the origin to the peaks in the Patterson map correspond to interatomic distances in the unit cell[†]. The Patterson function consists of N^2 terms (with N of them at the origin), each carrying a weight proportional to the products of the two atomic form factors involved in the given separation vector.^[42, p. 836] Therefore, any heavy atoms present in the unit cell will dominate the Patterson map. Using the phase of the largest vector of the Patterson map as a first approximation to the structure factor of the heaviest atom, followed by recalculation of the electron density, constitutes the iterative *Fourier method*^[42, p. 838], also known as *Patterson synthesis*.^[26, p. 131] Positions of certain atoms can sometimes be ascertained entirely from symmetry considerations.

Dual space methods involve successive use of Fourier- and inverse Fourier transformations of the electron density. For each iteration adjustments are made to the density. In the method of *charge flipping*, an initial set of random phases are generated (only at the first iteration) associated with the observed intensities. The structure factors are created and the electron density calculated by Fourier transformation. The density is then divided into two regions by a small, positive threshold value. A new density is constructed by subtracting the lower region from the upper. Temporary structure factors are next calculated by an inverse Fourier transform, and the actual structure factors are constructed with the phases of these, as long as the reflections are within the resolution sphere with radius $|\mathbf{h}|_{\max} = 1/d_{\min}$. The cycle is completed by computing the new electron density, and repeated until a convergence of the structure. Charge flipping is based on the assumption that the unit cell is mostly empty.^[43]

for how well the modelled structure agrees with experimental values

SHELX and structure refinement

SHELX is a renowned program suite for solving and refining crystal structures developed mainly by the British chemist George Michael Sheldrick. Three of the program components are of interest: *SHELXS* employs classical direct methods for solving the structure; *SHELXL* is concerned with structure refinement, mainly for small-molecule structures,^[44] and the final component, *SHELXT*, is a fairly recent addition that employs a novel dual-space algorithm to solve the phase problem.^[45] The *SHELX* programs are normally implemented in a more user-friendly software program such as *WinGX* or *Olex2*.^[46]

The level of agreement between the modelled structure and experimental values is indicated by various *R-factors*[‡]. One of them, the *merging residual value*, measures the internal consistency of data and is defined by:

$$R_{\text{int}} = \sum_j \left[\frac{\sum_i |F_{\text{obs}}^2 - \langle F_{\text{obs}}^2 \rangle|}{\sum_i |F_{\text{obs}}^2|} \right] \quad (2.25)$$

where the inner summations are over each reflection i in a symmetry equivalent set j , F_{obs}^2 denotes an intensity calculated from the data reduction and $\langle F_{\text{obs}}^2 \rangle$ is the average intensity of a set of equivalents. The outer sum is over all sets of reflections containing at least two symmetry equivalent reflections. The quality of the observed structure factors is also quantified by the ratio:

$$R_{\text{sigma}} = \sum_j \left[\frac{\sum_i \sigma_{\text{int}}(F_{\text{obs}}^2)}{\sum_i F_{\text{obs}}^2} \right] \quad (2.26)$$

where the summation is as in (2.25), but with $\sigma_{\text{int}}(F_{\text{obs}}^2)$ signifying the calculated *standard uncertainty* of the intensity of the merged reflection;^[47]

$$\sigma_{\text{int}}(F_{\text{obs}}^2) = \sqrt{\sum_i \frac{(F_{\text{obs}}^2 - \langle F_{\text{obs}}^2 \rangle)^2}{N_{\text{red}}}}, \quad (2.27)$$

where N_{red} is the number of redundant reflections. The standard uncertainties are calculated during the stage called

[†] Although \mathbf{r} are spatial coordinates of direct space, they are not related to the positions in the electron density of (2.5).

[‡] Synonyms for *R-factor*: *reliability index residual factor* and *discrepancy index*.

data reduction, which is when the raw intensities from the detector are translated into $|F_{\text{obs}}|^2$.^[44, p. 7] *CrysAlis* predicts reflection positions based on the orientation matrix and reconstruct their profiles across the frames. Partial reflections that are split across frames are also treated at this stage. The Lorentz and absorption corrections in (2.23) are applied as well as calculation of the standard deviations given by (2.27). Note that only observed quantities are required to calculate R_{int} and σ_{int} .

Once the atoms of the asymmetric unit have been located[†] and the proposed structure is in reasonable agreement with the observed data (and the iterative methods described give no significant changes), the model parameters are adjusted through non-linear least-squares refinement, with iterations until convergence of refinement.^[26, p. 138] The function to be minimised is usually one of the following:

$$M_{\text{abs}} = \sum_i w_i (|F_{\text{obs}}| - |F_{\text{calc}}|)^2 \quad (2.28)$$

$$M_{\text{square}} = \sum_i w_i (F_{\text{obs}}^2 - F_{\text{calc}}^2)^2 \quad (2.29)$$

where w_i denotes individual weights for each reflection (where applicable) and F_{calc} the calculated structure factor from the current model. The quality of the refinement is assessed!!!! by the R -factors:

$$R = R_1 = \frac{\sum_i ||F_{\text{obs}}| - |F_{\text{calc}}||}{\sum_i |F_{\text{obs}}|} \quad (2.30)$$

$$R_w = wR_2 = \sqrt{\frac{M_{\text{square}}}{\sum_i w_i F_{\text{obs}}^2}} \quad (2.31)$$

$$\text{Goof} = S = \sqrt{\frac{M_{\text{square}}}{N_{\text{ind}} - N_{\text{par}}}} \quad (2.32)$$

where N_{ind} is the number of independent reflections and N_{par} is the number of refined parameters. «Goof» stands for «goodness of fit» and should be close to 1.^[48] As for the R -factors; the merging factor R_{int} should generally be below 10 % and $R < 5$ % is considered good.^[48, p. 24]

The weights are usually based on the standard uncertainty, for example:

$$w = \frac{1}{\sigma_{\text{int}}(F_{\text{obs}})} \quad (2.33)$$

$$w = \frac{1}{\sigma_{\text{int}}^2(F_{\text{obs}})^2} \quad (2.34)$$

$$w = \frac{1}{\sigma_{\text{int}}^2(F_{\text{obs}}^2) + (\text{extra terms})} \quad (2.35)$$

where the «extra terms» could be functions of the structure factors, Bragg angle etc.^[26, p. 139] *SHELX* uses the following weighting scheme, which can have up to six parameters a, \dots, f :

$$w = \frac{q}{\sigma_{\text{int}}^2(F_{\text{obs}}^2) + (aP)^2 + bP + d + e \sin(\theta)/\lambda}, \quad (2.36a)$$

$$P = f \max(0, F_{\text{obs}}^2) + (1 - f) \cdot F_{\text{calc}}^2, \quad (2.36b)$$

$$q = \begin{cases} 1 & c = 0 \\ \exp\left[c \left(\frac{\sin \theta}{\lambda}\right)^2\right] & c > 0 \\ 1 - \exp\left[c \left(\frac{\sin \theta}{\lambda}\right)^2\right] & c < 0 \end{cases} \quad (2.36c)$$

[†] Hydrogen atoms are normally not included at this stage.

It is prompted by the `WGHT` command in the `.ins` file, and the default parameters are $a = 0.1$, $f = 1/3$ and the rest zero. Sheldrick recommends keeping them until all atoms have been found and the structure has practically converged to a solution.^[49] A different weighting scheme can be applied to improve the goodness of fit. *Olex2* uses only the two parameters a and b by default, and suggested values for these are provided by the refinement program *SHELXL*.^[50]

The data reduction in *CrysAlis* produces six output files:^[47] [51, p. 65] The `.cif` files contain detailed information on the structure (description of data collection, cell and space group, fractional coordinates of atoms); The `.hkl` files contain columns of hkl and the corresponding values for observed intensities F_{obs}^2 and standard deviations $\sigma_{\text{int}}(F_{\text{obs}}^2)$; The `.ins` files contain commands for the *SHELX* programs (see figure X); The `.p4p` files are alternative parameter files; Finally, a log of the data reduction procedure by *CrysAlis* is given in a `.sum` file.

<code>.cif</code>	crystallographic information file
<code>.cif_od</code>	Oxford Diffraction formatted <code>.cif</code>
<code>.hkl</code>	<i>SHELX</i> reflection data file
<code>.ins</code>	<i>SHELX</i> instruction file
<code>.p4p</code>	<i>XPREP</i> [†] data collection parameter file
<code>.sum</code>	summary file of data reduction procedure

Table 2.1: Data reduction output files from *CrysAlis*.

Normally, a couple of data reduction output files mentioned above are needed as input files in structure solution and refinement software. *Olex2* requires the `.hkl` and `.ins` files.

[†] *XPREP* is another *SHELX* program component.

2.3.2 Instrumentation setup

All data have been collected with a diffractometer based on the first generation of the DECTRIS PILATUS 2M area detector.^[52] The instrument is located at the *Swiss-Norwegian beamline* (SNBL) at the ESRF. In order to control the experiment a special software called *Pylatus* is used. Data is collected by the *rotation method*; the crystal is rotated about one of the goniometer axes and diffractograms are recorded and stored in the form of *crystallographic binary files* (`.cbf`). The set of all such files from a single experiment will be referred to as a *data set*[†]. For each data set an initial parameter file (`.par`) containing instrument and sample information has to be created with the application called *Crysis* found in the *SNBL ToolBox*. Finally, the data can be read and processed in *CrysAlis*.

This subsection will cover the necessary definitions of the instrument parameters involved in *CrysAlis*. The diffracting geometry is to a high extent based on a paper by Paciorek, Meyer and Chapuis.^{[53] [54]}

The orientation matrix

The *orientation matrix* \mathbf{UB} describes the crystal orientation with respect to the orientation of the diffractometer angles. It is the product of an *orthogonal rotation matrix* \mathbf{U} and an *orthonormalisation matrix* \mathbf{B} . The matrix \mathbf{B} transforms crystallographic coordinates in reciprocal space to Cartesian coordinates local to the crystal. The standard way of constructing the latter system is to first let its x -axis, $\mathbf{e}_x^{\mathbf{B}}$, coincide with the reciprocal unit cell vector \mathbf{a}^* . Then, the $\mathbf{e}_y^{\mathbf{B}}$ -axis is set so that it is normal to the $\mathbf{e}_x^{\mathbf{B}}$ -axis in addition to lying in the $\mathbf{a}^*\mathbf{b}^*$ plane. Finally, the $\mathbf{e}_z^{\mathbf{B}}$ -axis completes a right-handed coordinate system.^[55] From this we obtain an upper triangular \mathbf{B} matrix with element B_{ij} being the projection of $\mathbf{e}_j^{\mathbf{C}^*}$ onto $\mathbf{e}_i^{\mathbf{B}}$, where the superscript \mathbf{C}^* refers to the crystallographic coordinate system of the reciprocal unit cell and the indices denote the natural place of the i 'th or j 'th basis direction[‡]. The exact definition of the orientation matrix can depend on the actual diffractometer. For our setup we get from Busing and Levy:^[56]

$$\mathbf{B} = \begin{bmatrix} a^* & b^* \cos \gamma^* & c^* \cos \beta^* \\ 0 & b^* \sin \gamma^* & -c^* \sin \beta^* \cos \alpha \\ 0 & 0 & 1/c \end{bmatrix}, \quad (2.37)$$

Note that \mathbf{B} only depends on the unit cell parameters. Any coordinate vector \mathbf{h} in a reciprocal crystallographic reference frame will have a magnitude given by the standard norm, $\|\mathbf{h}\| = \sqrt{\langle \mathbf{h}, \mathbf{h} \rangle}$. By transforming to Cartesian coordinates first, we get the magnitude to be:

$$\|\mathbf{h}\| = \sqrt{\langle \mathbf{B}\mathbf{h}, \mathbf{B}\mathbf{h} \rangle} = \sqrt{(\mathbf{B}\mathbf{h})^{\mathbf{T}} \mathbf{B}\mathbf{h}} = \sqrt{\mathbf{h}^{\mathbf{T}} \mathbf{B}^{\mathbf{T}} \mathbf{B}\mathbf{h}}. \quad (2.38)$$

From this we may define the *reciprocal space metric tensor*:^[55]

$$\mathbf{G}^{-1} \equiv \mathbf{B}^{\mathbf{T}} \mathbf{B} \quad (2.39)$$

Since this is a symmetric and positive definite matrix, we may recognise \mathbf{B} as its Cholesky factor.

Next we need to transform from the Cartesian crystal frame to the Cartesian laboratory coordinate system. This is done by the use of Euler angles and is in practice represented by a product of three elementary rotations:^[53]

$$\mathbf{U} = \mathbf{R}_z(\phi_z) \mathbf{R}_y(\phi_y) \mathbf{R}_x(\phi_x), \quad (2.40)$$

where \mathbf{R}_i denotes the clockwise rotation matrix about axis i . The ϕ_x , ϕ_y and ϕ_z angles are the `r1`, `r2` and `r3` angles in *CrysAlis*.^[47]

The two matrices, \mathbf{U} and \mathbf{B} , are also regarded as QR factors where \mathbf{U} is the orthogonal matrix ($\mathbf{U}^{\mathbf{T}} = \mathbf{U}^{-1}$) and \mathbf{B} is an upper triangular matrix.^[53] It can also be noted that the orthonormalisation matrix \mathbf{B} does not have to be defined by (2.39).

[†] In cases where it is natural to associate multiple data sets to the same experiment (such as temperature development of a particular sample) the term *data subset* has been used instead. The whole collection of subsets for a given experiment then make up a «data set».

[‡] $i \in \{x, y, z\}$ and $j \in \{\mathbf{a}^*, \mathbf{b}^*, \mathbf{c}^*\}$. For example, element B_{23} contains the projection of \mathbf{c}^* onto the y -axis.

The orientation matrix is defined for the setting with all diffractometer angles set to zero and relates any reflection vector \mathbf{h} with a position vector \mathbf{r} in the Cartesian laboratory frame:^[55, p. 55]

$$\mathbf{r} = \mathbf{U}\mathbf{B}\mathbf{h}. \quad (2.41)$$

The right-hand side of (2.41) may be further expanded with misorientation matrices to correct for deviations about the laboratory axes.^[57]

To summarise:

1. A reciprocal lattice vector \mathbf{h} is defined according to the crystallographic directions of the reciprocal unit cell.
2. The coordinate system of the reciprocal unit cell is orthogonalised by the matrix \mathbf{B} .
3. A transformation between this system and the orthonormal laboratory frame is realised with \mathbf{U} .

Parameters in the instrument model

For the PILATUS 2M detector each `.cbf` file corresponds to a 1475×1679 image approximately 2.5 MB in size. The images are generated from an 8×3 array of modules at 487×195 pixels each with an intermodule gap of 7×17 pixels.^[54] Our data have been collected using a Huber 515 series κ -goniometer where the crystal has been rotated about the ϕ axis only.[†]^[58]

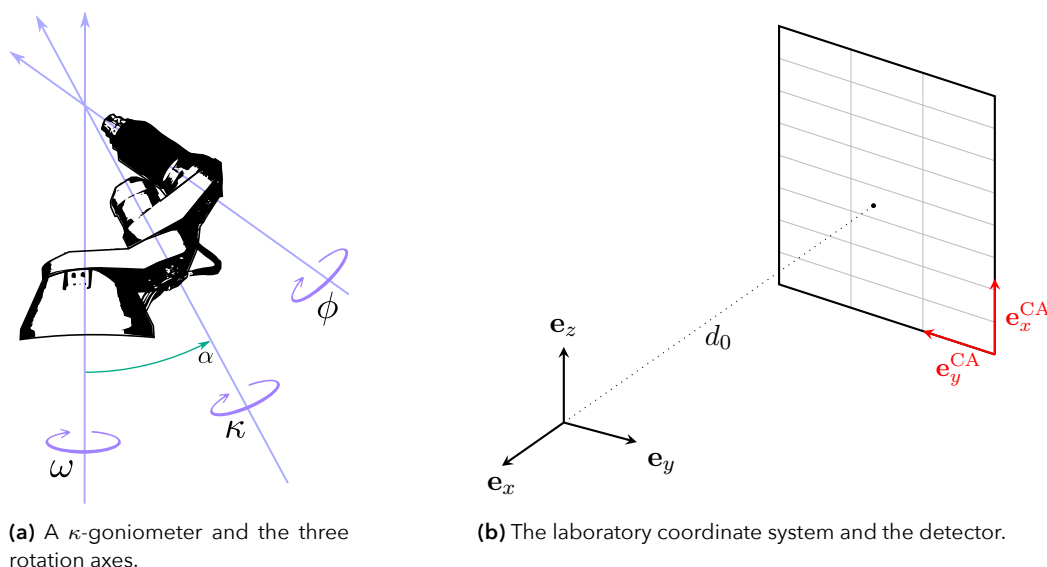


Figure 2.10: (a) A sketch of the goniometer (based on a figure by Brockhauser et al.^[59]). The sample is positioned in the ω - κ - ϕ intersection, which corresponds to the e_x - e_y - e_z intersection in (b) and is also called the *instrument centre*.^[60] The latter coordinate system, called the *laboratory frame*, is defined with e_x pointing towards the X-ray source; e_z coinciding with the ω -rotation axis, and e_y completing the right-hand coordinate system.^[53] e_x^{CA} and e_y^{CA} show the detector coordinate system used by *CrysAlis*. The plate in (b) represents the PILATUS detector screen with the array of modules.

The laboratory reference frame is shown in Figure 2.10b above. Note that the rotation axes of the goniometer use a left-hand system. If we were to swing the goniometer equipment shown in Figure 2.10a about the κ -axis back into alignment with ω ($\kappa = 0^\circ$), the goniometer angle β would ideally become zero as the ϕ -axis coincides with the ω -axis, but can be included to model any misalignment. Preliminary adjustments are done to centre the sample to the origin of the laboratory reference system.

The three angles $r1$, $r2$ and $r3$ are rotations of the crystal lattice with respect to the laboratory frame. The “wobbling” parameters shown in Table 2.2 can be used to account for any wobbling of the crystal as it rotates during data collection. Detector rotations $d1$, $d2$ and $d3$ refer to rotations of the detector screen.

The origin of the laboratory system is also taken to be the origin both of the crystal and the abstract Ewald sphere. The point where the incoming X-ray beam would intersect the sphere marks the origin of the reciprocal space.

	<i>CrysAlis</i> symbol	Description	Unit
Crystal	r1	crystal rotation about e_x -axis	[°]
	r2	crystal rotation about e_y -axis	
	r3	crystal rotation about e_z -axis	
	w1	crystal wobbling about e_x -axis	
	w2	crystal wobbling about e_y -axis	
	w3	crystal wobbling about e_z -axis	
Goniometer	b2	beam rotation about e_y -axis	[°]
	b3	beam rotation about e_z -axis	
	a1	goniometer angle α	
	be	goniometer angle β	
	o0	goniometer software zero ω	
	t0	goniometer software zero θ	
	k0	goniometer software zero κ	
	p0	goniometer software zero ϕ	
Detector	d1	detector rotation about e_x -axis	[°]
	d2	detector rotation about e_y -axis	
	d3	detector rotation about e_z -axis	
	x0	detector offset of e_x^{CA} -axis	[px]
	y0	detector offset of e_y^{CA} -axis	[px]
	dd	distance from goniometer to detector	[mm]

Table 2.2: *CrysAlis* symbols associated with the parameters of the instrument model and short descriptions.

[†] The ϕ -axis may be visualised as the axis that “impales” the sample.

Contribution of the background radiation decreases with the square of the distance, so a longer crystal-to-detector distance may be preferable.^[34] The resolution of individual reflections, however, decreases with increasing crystal-to-detector distance (as they span fewer pixels). A shorter detector distance will allow for greater θ_{\max} , thus increasing the resolution of the data set.

The exposure time also needs to be set to an optimal value, as too short exposure time results in noisy images with poor resolution, and too much exposure leads to saturated spots.^[61] It is also important to centre the crystal correctly for it to have a constant amount of volume in the X-ray beam (thus providing a constant diffracting power).^[26, p. 128]

An advantage with pixel area detector systems is that they record many reflections simultaneously, not just regions around certain reciprocal lattice points, and we their profiles are effectively three-dimensional.^[26, p. 127] The diffraction pattern is also recorded directly on the detector surface by charge-coupled devices (CCD) – radiation sensitive semi-conductor capacitors that convert light into a digital signal.^[40, p. 64] The use of such detectors together with synchrotron radiation enables us to collect vast amounts of data in the matter of minutes or hours. It is also easier to acquire complete diffraction patterns at a high degree of redundancy.

2.3.3 An overview of the *CrysAlis* software

For single-crystal diffraction experiments, *CrysAlis* is used to handle and analyse data. Primary tasks include determining the unit cell and checking the crystal quality.

The main window of *CrysAlis* is shown in Figure 2.12 below, along with its **Lattice wizard** to the right.

The «Setup» comprises, for our purposes, any pre-setting of the instrument model parameters or polarisation factor and can be reached from the **Command shell** or the **Lattice wizard**.

The next step is the crucial «Peak hunt». Here the data from the X-ray diffraction experiment is processed to determine which reflections are present. The *peak table* is a list of *hkl* values assigned to the observed reflections with the corresponding coordinates and intensity. As the screenshot in Figure 2.13 shows, there are three build-in methods to choose from; an automatic threshold method, a traditional peak hunt, and a smart peak hunt. There is also another automatic peak hunting method called «Auto analyse unit cell», see Figure 2.14.

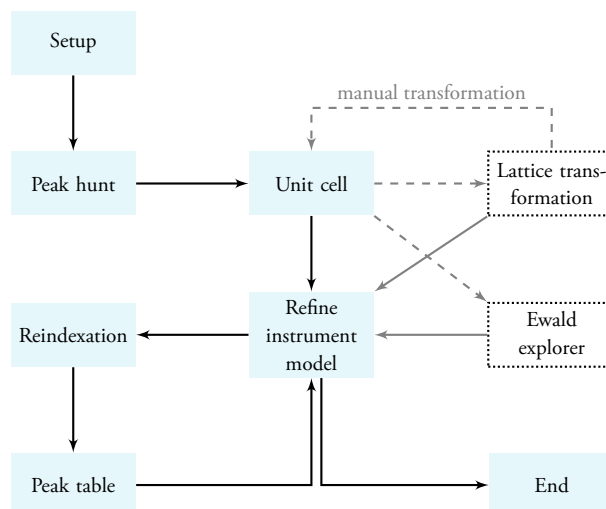
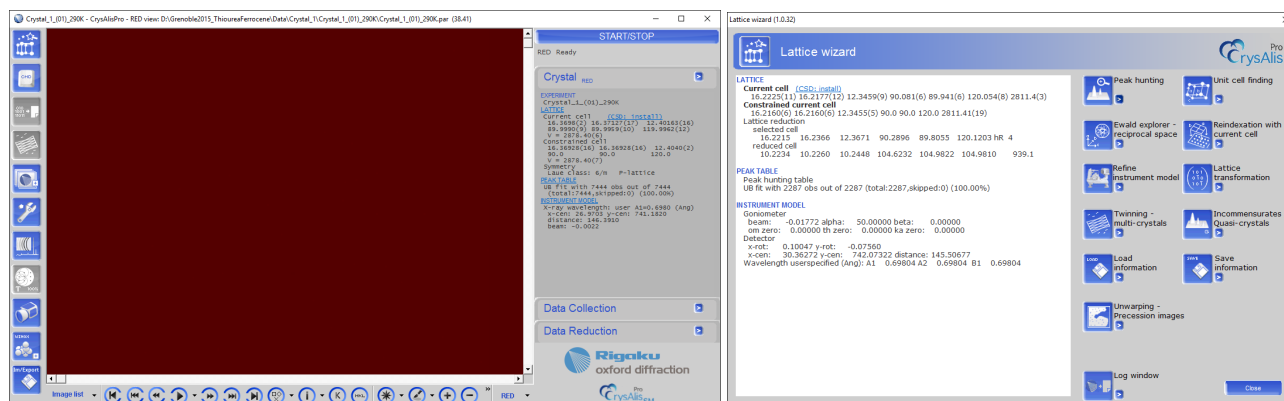


Figure 2.11: *CrysAlis* flowchart of the initial procedures for unit cell determination and refinement. Elaboration on the steps involved are presented in the text. Any data reduction and structure analysis comes after.



(a) The main window of *CrysAlis*.

(b) The **Lattice wizard**.

Figure 2.12: (a) The main window of *CrysAlis*. The two top buttons to the left open the **Lattice wizard** and **Command shell**. We can also see details about the unit cell in the «Crystal» tab to the right. In this case, we are looking at the data subset *Crysta1_1_(01)*. (b) The **Lattice wizard**, which contains the necessary tools for data treatment. These screenshots are from the *Crysta1_4_(01)* data subset.

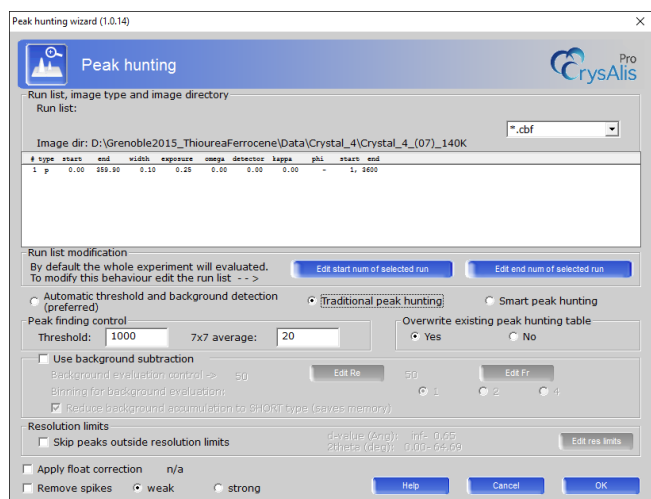


Figure 2.13: The peak hunting wizard. Three main methods for finding peaks are presented.

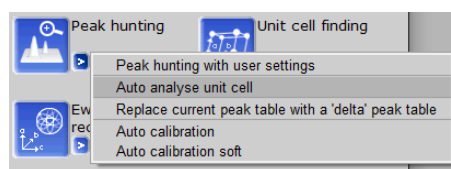


Figure 2.14: The preferred automatic peak hunt method.

The different peak searching algorithms make *CrysAlis* more versatile, but finding the optimal settings can be a challenge. Ideally, one would try all possibilities and choose the method that resulted in finding the largest amount of peaks. Too many peaks, however, could be the result of a background threshold being too low, and a majority of the peaks would not fit the lattice anyway. The «auto analyse unit cell»-method takes some extra

time, but has the benefit of being more thorough, at least seemingly. It has also proved to be consistent in regards to reproducing the same peak table for the same data sets. The purpose of the peak table is to construct an orientation matrix as accurate as possible, which will, for instance, be employed in the data reduction.

After determining the peaks comes the task of assigning a unit cell to them. This is usually done automatically by *CrysAlis*, but the user may influence the decision by setting the cell constants (if known), orientation matrix or other constraints. The unit cell obtained from analysing the data does not necessarily correspond to the Bravais lattice.^[62] *CrysAlis* does, however, provide a list of closely-related cells that may be used instead. Whether “wrongly” determined unit cells imply an inaccurate peak table, wrong program settings or simply a correct but unexpected cell, is hard to say.

In addition to the amount of peaks found, one may judge the peak table quality by viewing them in *Ewald explorer*, shown in Figure 2.15. This application gives a three-dimensional overview of the peaks, revealing obvious faults such as substantial voids[†] of reflections or concentric shells of reflections, which is the case with non-crystalline samples. Inspection for twinning can also be done here.

The next step is to refine the parameters of the diffractometer (see Table 2.2). Depending on the symmetry of the unit cell (known or apparent from the previous steps), constraints on the lattice parameters may be specified at this stage; see Figure 2.16 below. Only checked quantities will be run through least-square refinements.

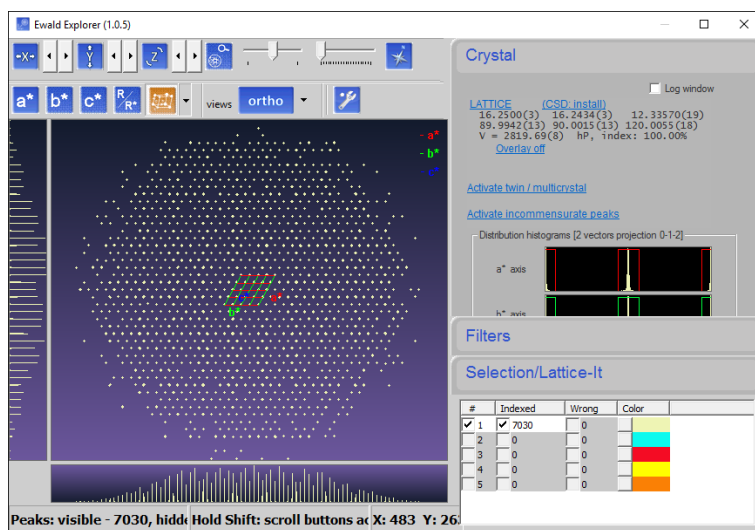


Figure 2.15: The *Ewald explorer* provides a three-dimensional overview of the peaks, here in the c^* direction.



Figure 2.16: The *Refine instrument model*. In this example with a hexagonal lattice, the only free lattice parameters are a and c .

the progress in *CrysAlis* and gathering files that may be of use, such as peak table data or the project log file. The log files are very useful as the instrument parameters and various matrices are contained in them. Extraction of the latest refined values can be done with the `RefinedValues` function in the *Xray* package.

[†] Voids could result from the nature of the experiment.

[‡] This residual factor, which concerns the refinement of the instrument model, is not to be confused with the R -factors in (2.25) or (2.30).

The so-called `Unwarp` feature of *CrysAlis*, found in the `Lattice wizard`, allows one to create images of the reciprocal space at a desired orientation and resolution. This process uses all the relevant image data. Although it is unaffected by any manipulation of the peak table, an accurate orientation matrix is crucial. With this tool, thousands of cross sections of reciprocal space have been generated. The purpose of this is to gain insight to the structure, indirectly, by revealing any characteristic features in the reciprocal space.

This window in Figure 2.17 shows the step where the specific properties of a layer is defined. A list of layers may be generated with `UnwarpLayerList` in the `Xray` package.

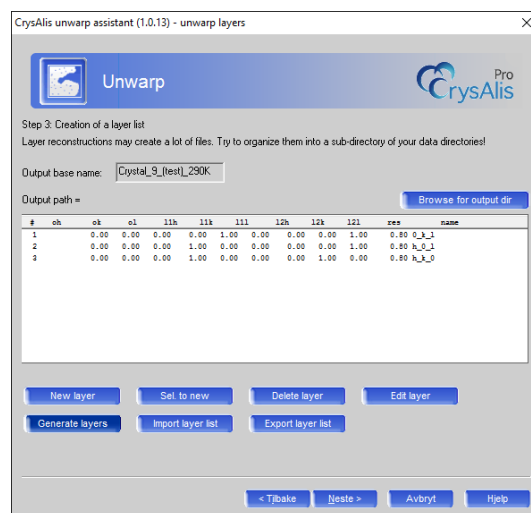
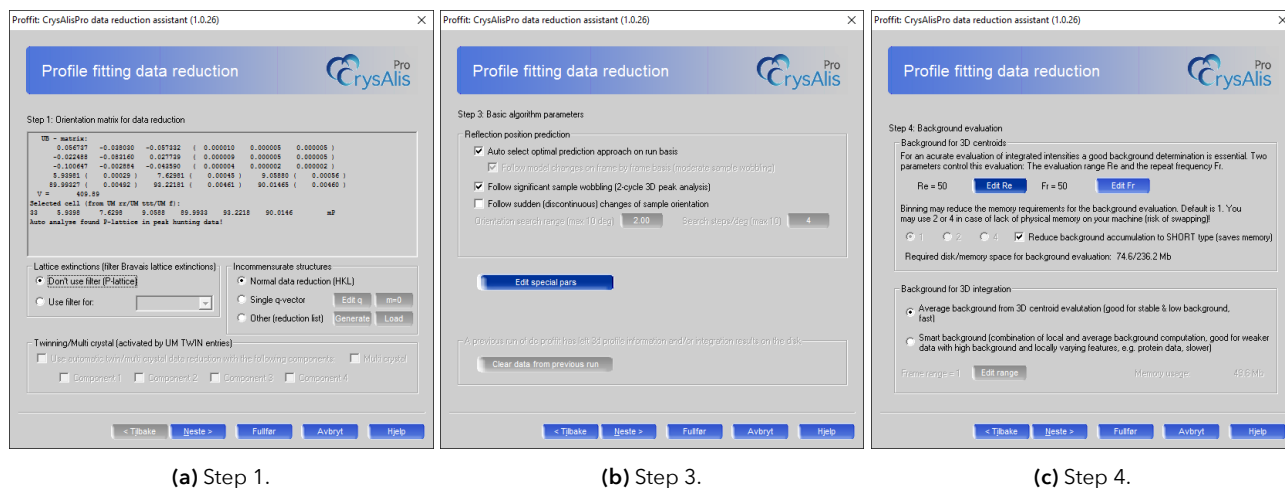


Figure 2.17: CrysAlis' `Unwarp` feature.

Data reduction

When we come to the «end» in the flowchart in Figure 2.11 with satisfactory peak table and model refinements, we may initiate the “data reduction”, i.e. the process of reconstructing the peak profiles (as mentioned briefly on page 19).



(a) Step 1.

(b) Step 3.

(c) Step 4.

Figure 2.18: Screenshots of the data reduction steps in *CrysAlis* – continued in Figure 2.20.

The data reduction procedure in *CrysAlis* is broken into six main steps. In the first step we have the option to ignore reflections that should be absent for a given lattice centring. Analysis of incommensurate and twinned crystals is also enabled at this stage.

In step 2 (omitted in Figure 2.18) the user can choose to only evaluate a partial set of the whole experiment, but this is not of interest of us as we only have one run per data subset.

Step 3 lets us adjust parameters of the algorithms for determining the peak profiles. The “special parameters” are shown in Figure 2.19. Note that the option «HKL check in 3D peak analysis» has been checked manually.

In step 4 we normally choose the «smart background» integration method and uncheck «Reduce background accumulation».

We can choose to reject outliers in step 5. Symmetry equivalent reflections are compared using a selected Laue class.

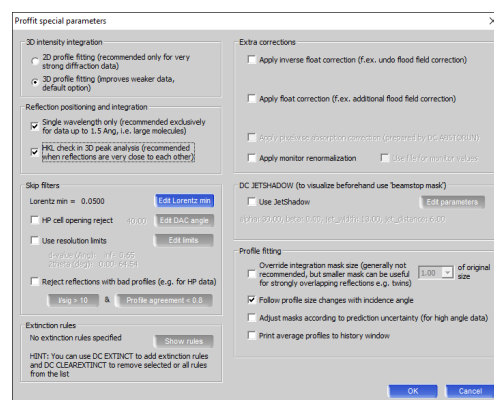
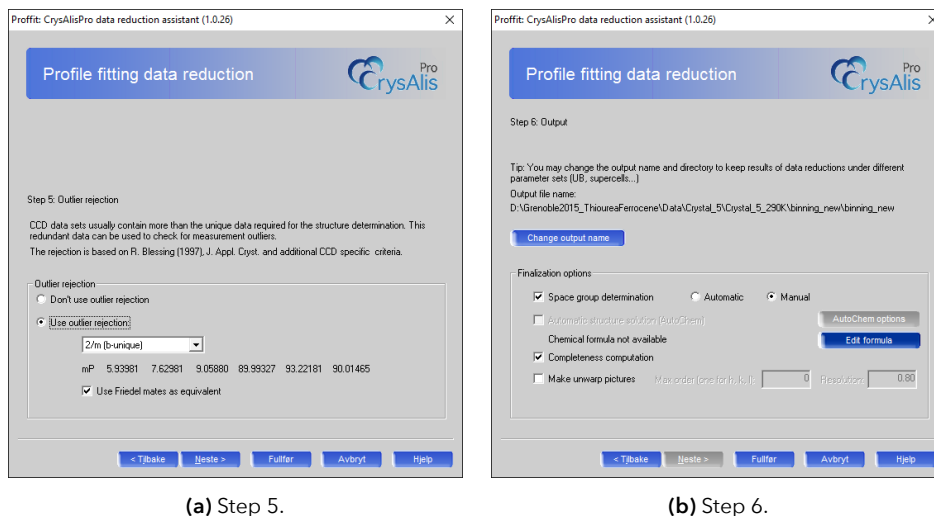


Figure 2.19: Extra profile fitting options.

In the final step we choose whether to take part in the space group determination or not. The chemical composition may be provided here as well.



(a) Step 5.

(b) Step 6.

Figure 2.20: The final steps in the data reduction.

The SNBL Toolbox

Shown in Figure 2.21 are screenshots from the *SNBL Toolbox*^[63] mentioned in subsection 2.3.2.

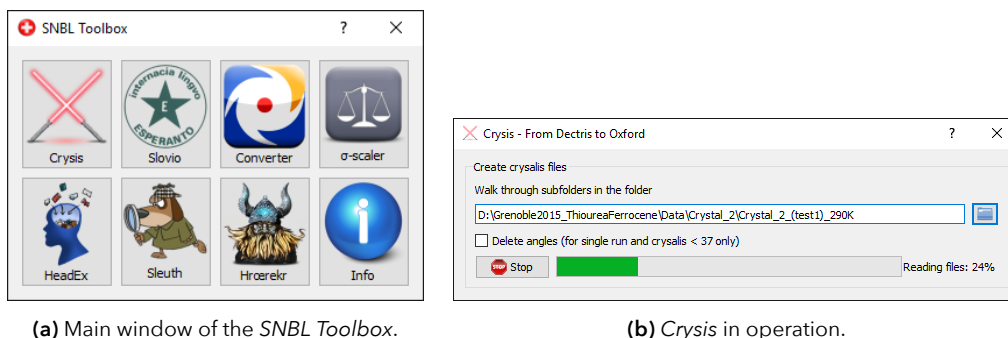
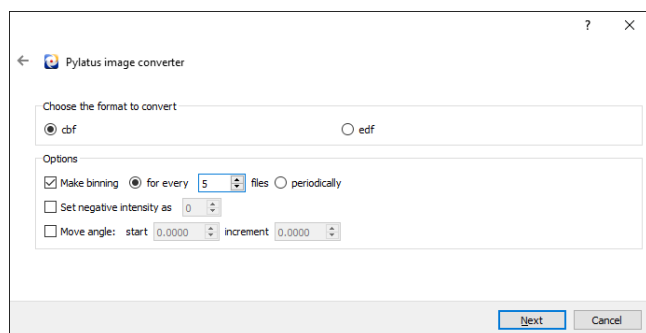
(a) Main window of the *SNBL Toolbox*.(b) *CrysAlis* in operation.Figure 2.21: The *SNBL Toolbox* version 0.5 and the *CrysAlis* component

Figure 2.22: The program used to bin the images.

Figure 2.21b shows the *CrysAlis* program, which prepares the initial parameter file for *CrysAlis*. The «Delete angles» option in should not be checked, and has in some cases removed angular metadata from the headers of *.cbf* files. It is likely a compatibility issue between the toolbox and newer versions of *CrysAlis*.

2.4 Ferrocene and thiourea-ferrocene

2.4.1 Ferrocene

Ferrocene ($C_{10}H_{10}Fe$ or $Fe(C_5H_5)_2$) was discovered in 1951 by the chemist Peter Ludwig Pauson and his student Tom Joseph Kealy[†]. They were supposed to make pentafulvalene, which has a similar but linear structure without iron^[66]. The “sandwich”-like structure, where an iron atom is positioned between two cyclopentadienyl rings (Cp), was first suggested by Robert Burns Woodward and Sir Geoffrey Wilkinson, and independently by Ernst Otto Fischer, and was later confirmed by X-ray studies.^{[64] [67]} If one replaces the iron with any metal cation, the general structure is referred to as a *metallocene*, which in turn is a subset of the broader class of so-called *sandwich compounds*.^[68] Fischer and Wilkinson were awarded the Nobel Prize in Chemistry in 1973 for the structure determination of ferrocene and their research on other sandwich compounds.^[67]

We distinguish between three possible ways the two carbon rings can be rotated in relation to each other: If they are oriented exactly the same they are in an *eclipsed* conformation; If one of the rings is rotated 36° from the other they are said to be in *staggered* conformation. Rotation by any other amount is referred to as *twisted*.

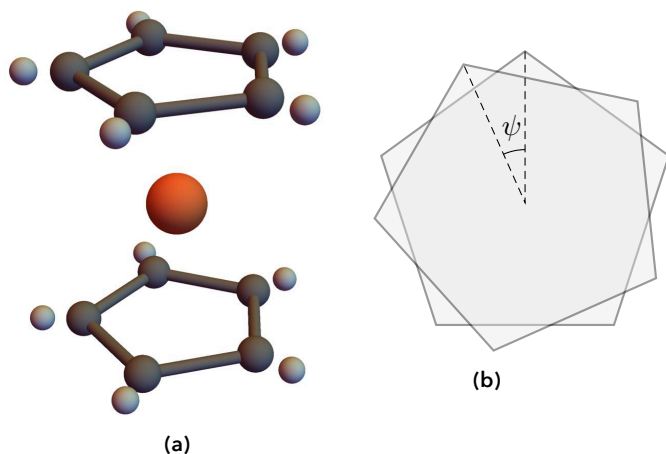


Figure 2.23: (a) The atomic structure of ferrocene. ●: Iron, ●: Carbon, ●: Hydrogen. The two parallel pentagons are the cyclopentadienyl anion rings. The “edges” of the rings (carbon-carbon bond distances) are $(1.403 \pm 0.020) \text{ \AA}$ and the distance from iron to the nearest carbon $(2.045 \pm 0.010) \text{ \AA}$.^[69] (b) Top view of the rings. $\psi = 0^\circ$ and $\psi = 36^\circ$ correspond to eclipsed and staggered conformations, respectively.

monoclinic with space group $P2_1/a$ at room temperature with lattice parameters:^{[69] [77]}

$$a = 10.561(11) \text{ \AA}, \quad b = 7.597(8) \text{ \AA}, \quad c = 5.952(6) \text{ \AA}, \quad \beta = 121.02(12)^\circ; \quad (2.42)$$

Ferrocene is very non-rigid and said to possess conformational freedom. Structural flexibility is a characteristic trait of organometallic molecules.^[78, p. 466] Above 190 K, the cyclopentadienyl rings are rotating, being staggered on average^[74], but freeze into nearly eclipsed conformation at 164 K^[79]. At this point, ferrocene transitions to a triclinic structure with the rings twisted 9° and the colour changes from orange to yellow^{[76] [75] [2]}.

Bermúdez-García et al.^[79] have also studied the electrical dipole moment of ferrocene and concluded that in this low-temperature phase, the molecules will either have a dipole moment pointing parallel to the plane of the cyclopentadienyl rings (type I) or normal to them (type II). Moreover, Type I has a dipole magnitude that is about twice that of type II. In the transition process the iron cation is shifted off centre, removing the inversion symmetry of ferrocene. Seiler and Dunitz state that crystals cooled from room temperature to the triclinic phase will always be twinned.^[76]

An orthorhombic phase of ferrocene has also been attained in the temperature range 78 K to 250 K, but crys-

[†] Ferrocene was made earlier by Samuel A. Miller, John A. Tebbboth and John F. Tremaine, but they published later.^{[64] [65]}

tallisation occurs at 110 K or less.^[77] Ferrocene is then eclipsed^[74] and the space group is found to be $Pnma$ and lattice parameters (at 98 K):^[76]

$$a = (6.987 \pm 0.006) \text{ \AA}, \quad b = (8.995 \pm 0.007) \text{ \AA}, \quad c = (12.196 \pm 0.005) \text{ \AA}. \quad (2.43)$$

A crystal size roughly between 40 μm to 300 μm is necessary for obtaining the orthorhombic structure.^[77]

2.4.2 Thiourea-ferrocene

Thiourea ($\text{SC}(\text{NH}_2)_2$) is a ferroelectric which crystallises in an orthorhombic cell at room temperature with parameters:^[80]

$$a = (7.5429 \pm 0.0008) \text{ \AA}, \quad b = (8.5422 \pm 0.0007) \text{ \AA}, \quad c = (5.4647 \pm 0.0004) \text{ \AA}, \quad (2.44)$$

in the space group $Pnma$ with $Z = 4$. Cooling it below $T_1 = 202 \text{ K}$ changes the crystal from a paraelectric to a ferroelectric phase. Going below the critical temperature $T_2 = 169 \text{ K}$, a transition to the space group $Pmc2_1$ occurs.^[81]

It is of interest to us because mixing it with ferrocene results in an *inclusion compound*.

This is a system in which one of the components, called the *guest*, is confined within the structure of the *host*.^[82] The host-to-host interactions dominate the crystal structure, and the two components can be distinguished individually.^[2]

Thiourea is categorised as a *soft host*, meaning its structure changes substantially in the presence of guest components – we also say that its framework is *interrupted* by the guest introduction. The term *clathrate compound* is further used to emphasise the guest molecules being caged by arrays of the host molecules. If the guest molecules align linearly in the clathrate we may describe it as a *tunnel inclusion complex*[†].

Urea ($\text{CO}(\text{NH}_2)_2$), a compound very similar to thiourea, is referred to as a *versatile host* since it may form hexagonal, orthorhombic or rhombohedral tunnel inclusion compounds.^[2] On the contrary, thiourea is regarded as *non-versatile* in the sense that when structural changes occur, it will only form rhombohedral tunnel inclusion complexes.^[2] Nevertheless, thiourea is able to form inclusion complexes with a greater variety of guests than urea, and has a larger tunnel diameter of about 6.1 \AA compared to urea (5.25 \AA).^[3] In hexagonal inclusions, the host molecules have a helical and chiral arrangement, contrary to the layered and non-chiral arrangements found in the rhombohedral complexes. This comes from the fact that the tunnels of the hexagonal type have a uniform force field both along the tunnel direction and normal to it, giving the guest molecules of cylindrical shapes no preferred location in it. On the other hand, the force field along the tunnel axis of rhombohedral complexes have a period of about 5.5 \AA . If guest molecules have similar periodicity, rhombohedral formation is favoured over hexagonal formation.^[2]

The cell dimensions of thiourea complexes, in hexagonal setting, are generally about $a \approx 15.8 \text{ \AA}$ and $c \approx 12.5 \text{ \AA}$ with $Z = 6$ formula units per unit cell, space group $R\bar{3}c$ and the edge of the hexagonal tunnel approximately 5.37 \AA .^[2, p. 231]

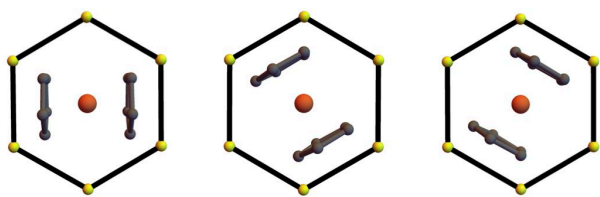


Figure 2.25: The three possible subconfigurations of the perpendicular orientation as given by Sorai et al.^[3] The hexagons are crude representations of thiourea.

[†] The word *channel* is sometimes used instead of «tunnel».

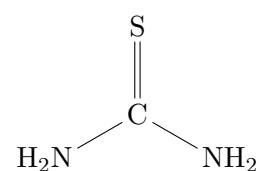


Figure 2.24: The structural formula of thiourea. Urea would have oxygen in place of the sulphur atom.

The tunnels of the urea and thiourea inclusion complexes all have hexagonal cross sections, and the host molecules form spirals whose axes are centred between three adjacent tunnels.

In the *thiourea-ferrocene* clathrate ($\text{C}_{13} \text{H}_{22} \text{Fe} \text{N}_6 \text{S}_3$), thiourea acts as the host and form a honeycomb of tunnels with trigonal symmetry. Within these tunnels, the ferro-

cene may be aligned either parallel to the host lattice, i.e. its fivefold molecular axis coincide with that of the tunnel, or perpendicular, meaning the molecular axis lies in the plane of the host lattice. The three possible subconfigurations of the perpendicular orientation are shown in Figure 2.25. Nuclear magnetic resonance studies by Lowery et al.^[83] indicate, however, that the parallel orientation is an approximation, and that there are three subconfigurations also here, tilted about 17° from the tunnel axis and related by a threefold axis.

The cyclopentadienyl rings of neighbouring ferrocene molecules repel each other, which leads to tilting and rotation of the ferrocenes. The rings are also reported to be three-dimensionally disordered at room temperature, and that finding two neighbouring ferrocenes in the parallel orientation was unlikely due to the cyclopentadienyl rings being very close.^[84] Monte Carlo simulations by Drew et al.^[85] show that the parallel orientation is preferred over the perpendicular by a ratio of 3 : 2, while Gibb claims the exact opposite.^[86] At 140 K, Lowery et al.^[83] state that about 55 % of the ferrocenes are in the perpendicular orientation.

Nicholson and Hough^[84] have determined the crystal structure of 3 : 1 thiourea-ferrocene to be rhombohedral with space group $R\bar{3}c$ and cell parameters:

$$a = (16.360 \pm 0.003) \text{ \AA}, \quad c = (12.395 \pm 0.002) \text{ \AA}, \quad (2.45)$$

with $Z = 6$ in a unit cell based on the hexagonal setting. Sorai et al.^[3] measured slightly larger parameters;

$$a = 16.40 \text{ \AA}, \quad c = 12.50 \text{ \AA}. \quad (2.46)$$

Phase transitions

In 1981 Sorai et al.^[3] used an adiabatic-type calorimeter to measure excess heat capacities in the range 13 K to 280 K and found five phase transitions occurring at the critical temperatures:

$$T_1 = 147.2 \text{ K}, \quad T_2 = 159.79 \text{ K}, \quad T_3 = 171.4 \text{ K}, \quad T_4 = 185.5 \text{ K}, \quad T_5 = 220 \text{ K}, \quad (2.47)$$

where T_2 is associated with first-order transition, the higher temperatures with second-order, and T_1 is ambiguous. The different phases are labelled with Roman letters I–VI, with the first phase I being above T_5 , phase II between T_4 and T_5 , and so on – see Figure 2.26. Results from this study and Clement et al.^[87] indicate that the transition at T_2 is the strongest and involves a volume change.

The two lowest temperature transitions are linked with reorientation of the ferrocenes. Below 141 K the ferrocenes are static and effectively frozen-in, with an equal probability of finding the ferrocene in the parallel and perpendicular orientations.^{[86][83]} Going from phase VI to V, multiple ferrocene molecules will collectively form a spiral pattern along the tunnel axis with specific phase relations. This restriction is then lifted in the V to IV-transition, which is associated with the ferrocene flipping up to the parallel orientation, as well as a rapid reorientation of these molecules about the channel axis.^{[86][3]} Hough and Nicholson^[84] also found that the crystal twins reversibly below T_2 . Above 300 K, the ferrocenes are believed to tumble rapidly between all positions.^[83]

Very little is known about changes in the thiourea matrix,^[2] but the host lattice forming the hexagonal tunnels are stationary from 140 K to 298 K.^[83]

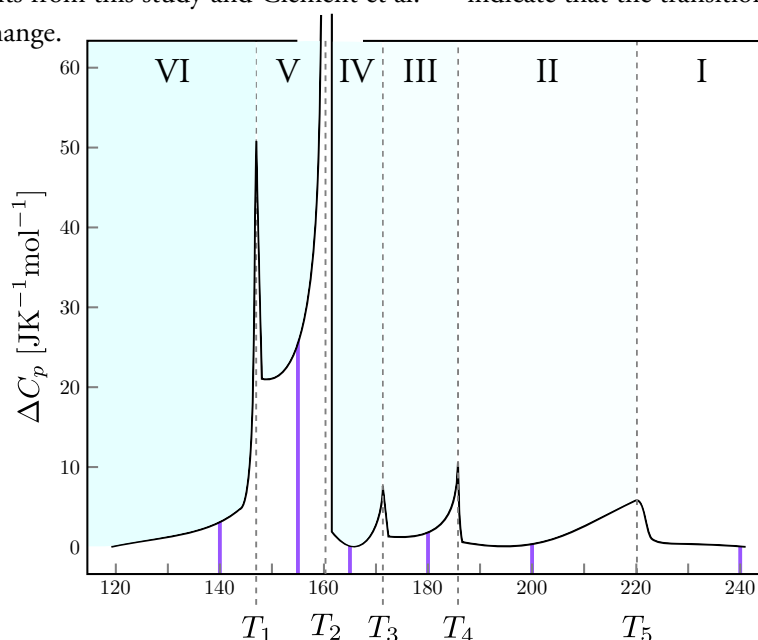


Figure 2.26: The excess heat capacities arising from the phase transitions. Dashed grey lines indicate where transitions occur, and the purple lines at what temperature our crystallographic studies have taken place (some are out of range). The plot is reproduced from Sorai et al.^[3] Temperatures on the horizontal axis are in kelvins.

Chapter 3

Analysis

3.1 Silicon data

Data has been collected on six different silicon crystals at the ESRF in the autumn of 2014. First, the *Mathematica* function calculating and presenting the related quantities will be introduced and validated in subsection 3.1.1. Thereafter, intensities obtained from data reduction of the silicon data will be compared to theoretical values in subsection 3.1.2.

3.1.1 Comparing calculations with literature

Structure factors and checking of absent reflections are calculated by *Mathematica* functions developed earlier by Thorkildsen and Larsen. These have been integrated in the `StructureFactorTable` function in a way that allows for a relatively quick and easy way of obtaining the most significant structure factors, along with the quantities relevant to the study of dynamical effects in silicon. An example is given in Figure 3.1.

```
StructureFactorTable[
  0.70913713, "silicon", "m3m",
  {h_, k_, l_} /; OddQ[h] || Divisible[h + k + l, 4],
  "Sort" -> 4, "Keep" -> 9
]
```

(a) Input example in *Mathematica*.

(hkl)	Structure factor $ F_{hkl} $	Phase ϕ_{hkl} [°]	Bragg angle θ_B [°]	Pendellösung distance Λ_0 [μm]	Darwin width $2\delta_{os}$ [μrad]
(111)	59.374	-179.620	6.493	42.140	14.881
(220)	68.225	-179.540	10.641	36.275	10.586
(311)	44.716	-179.510	12.506	54.979	5.957
(400)	57.093	-179.470	15.138	42.576	6.378
(331)	38.199	0.554	16.534	63.198	3.943
(422)	49.472	0.593	18.653	48.227	4.597
(333)	33.235	0.617	19.831	71.276	2.933
(511)	33.235	0.617	19.831	71.276	2.933
(440)	43.239	0.658	21.674	54.122	3.548

(b) The corresponding output.

Figure 3.1: Example of input and output of the `StructureFactorTable` function. The first input argument is the wavelength (here: $\lambda = 0.70931713 \text{ \AA}$ for $\text{MoK}\alpha_1$ from Authier^[1, p. 438]). The next two arguments request data for the actual compound and Laue class, respectively (here: silicon and $m\bar{3}m$). The remaining arguments are optional; The first of them takes extra reflection conditions into consideration (here: Miller index h needs to be odd or the digit sum $h+k+l$ must be divisible by four), while the last two are concerned with the table formatting; The table is sorted by increasing values in the fourth column (Bragg angles) and only the first nine entries are presented.

The user needs to at least input the radiation wavelength, the name of the crystal[†] and the Laue class. The procedure starts by reading in the compound data. Scattering factors are computed using a function that is a linear combination

[†] Information on the unit cell, asymmetric unit and scattering coefficients is contained in a `.dat` file of the same name as the compound or crystal. The `Xray` package currently contains 29 such data files.

of five Gaussians:

$$f(s) = \sum_{i=1}^5 a_i \exp(-b_i s^2) + c, \quad s \equiv \frac{\sin(\theta)}{\lambda}. \quad (3.1)$$

The function is an analytical approximation and is based on tabulated values from volume C of the *International Tables for Crystallography*.^[89] Our values for the eleven parameters (scattering coefficients), $a_1, a_2, \dots, b_1, \dots, b_5, c$, are gathered from Waasmaier and Kirfel, who claim $f(s)$ is valid for values of $\sin(\theta)/\lambda$ up to 6.0 \AA^{-1} .^[90] Corrections of the atomic scattering factor due to anomalous scattering, f' and f'' , is computed by interpolating in tabulated values for the appropriate wavelength. The calculations are based on work by Cromer and Liberman.^[91]

A list of reflections is generated with the function `ReflectionList`, which filters away systematic absent reflections. From Bragg's (2.7) we have (for the first-order reflection):

$$\sin \theta = \frac{\lambda}{2d_{hkl}} = \frac{\lambda}{2} \sqrt{\mathbf{h}^T \mathbf{G}^{-1} \mathbf{h}}, \quad (3.2)$$

where \mathbf{h} is a reciprocal lattice vector and \mathbf{G}^{-1} is the metric tensor of the reciprocal space. From (3.2) we see that certain \mathbf{h} may correspond to a complex angle for a given wavelength. The function also removes these reflections before merging by symmetry equivalence. Next the quantities we see in the table of Figure 3.1 are computed.

Comparing structure factors

Theoretical values from the `StructureFactorTable` function have been compared to three other sources, as shown in Table 3.1 to the right. Comparisons have been made for the three compounds silicon (Si), germanium (Ge) and gallium arsenide (GaAs) at the two characteristic wavelengths of Mo K_{α_1} and Cu K_{α_1} .

We see that silicon values are in good agreement with Authier^[1] with our values being just 0.74% less than his on average. Given that the energy corresponding to the wavelength of Mo K_{α_1} is 17.479 keV^[1, p. 438], we can compare with matching data from Cornell University's CHESSE database.^[88] This time our values are 13.1% less than those found in the database

	<i>hkl</i>	structureFactorTable	Authier ^[1, p. 315]	CHESSE database ^[88]	structureFactorTable	Chang ^[11, p. 183,191]
Silicon	111	59.374	60.55	58.728		
	220	68.226	67.84	69.329		
	311	44.717	44.0	46.147		
	400	57.093	56.6	60.212		
	331	38.199	38.5	40.754		
	422	49.473	49.7	53.755		
	511	33.235	33.2	36.502		
	440	43.239	43.3	48.341		
	444	33.582	33.61	39.755		
	642	29.830	29.86	0		
	660	23.904	23.9	30.883		
555	16.251	16.20	21.230			
844	17.786	17.68	25.114			
880	12.730	14.3	20.255			
Germanium	111	154.03		154.81		145.71
	220	185.69		190.37		173.923
	311	121.92		126.58		113.646
	400	154.4		163.68		143.089
	331	102.72		110.22		94.846
	422	132.05		144.55		122.610
	511	88.449		97.986		
	440	114.78		129.71		105.620
	444	89.613		108.03		
	642	80.194		0		
	660	65.594		87.245		
555	44.794		60.316			
844	54.981		74.447			
880	47.039		64.138			
Gallium arsenide	111				146.220	147.971
	200				6.754	15.809
	220				174.310	174.219
	311				114.130	114.179
	222				5.760	
	400				142.360	142.769
	331				93.860	95.032
	420				6.052	6.538
	422				119.830	
	333				80.228	80.251
	440				102.590	103.526
442				5.832	6.538	

Table 3.1: Comparison of the structure factors generated from `StructureFactorTable` and other sources. The wavelengths used were $\lambda_{\text{Mo}} = 0.709317 \text{ \AA}$ and $\lambda_{\text{Cu}} = 1.540593 \text{ \AA}$ from Authier^[1, p. 438].

on average. We also see a clear tendency of the discrepancy increasing for each reflection having a greater Bragg angle (as the hkl list here is sorted by), which is likely due to different displacement parameters being used.

The discrepancies we see are likely to emerge from using different sources for scattering factors.

Comparing the Darwin width with literature

A table analogous to Table 3.1 can be made for Darwin widths. Again, Cornell University's database has been used to provide values, now also for Cu K_{α_1} at 8.048 keV. ^[1, p. 438] A table with ten Darwin widths was found in a book by Pike and Sabatier ^[20, p. 1121], but these corresponded to a wavelength of one ångström. For the CHESSE database, a wavelength of 1.0 Å was obtained for 12.398 keV.

	hkl	structureFactorTable	Authier ^[1, p. 447]	CHESSE database ^[88]		structureFactorTable	Authier ^[1, p. 447]	CHESSE database ^[88]		structureFactorTable	Pike and Sabatier ^[20, p. 1121]	CHESSE database ^[88]
Si $M_{\alpha} K_{\alpha_1}$	111	14.885	15.2	14.719	Si $Cu K_{\alpha_1}$	33.691	33.8	32.767	Si 1.0 \AA	21.245	20.847	20.885
	220	10.589	10.6	10.757		25.176	24.6	25.067		13.304	7.272	15.438
	311	5.958		6.147		14.627		14.770		8.677	8.727	8.885
	422	4.599		4.995		13.507		14.293		6.946	3.103	7.476
	333	2.934		3.221		9.112		9.736		4.473	1.309	4.865
440	3.549	3.6	3.966	12.354	12.0	13.413	5.502				6.087	
Ge $M_{\alpha} K_{\alpha_1}$	111	35.561	35.6	35.741	Ge $Cu K_{\alpha_1}$	75.323	75.4	79.404	Ge 1.0 \AA	48.154	49.936	50.688
	220	26.518	26.6	27.187		58.115	58.0	62.976		36.063	18.423	39.358
	311	14.939		15.511		33.531		36.931		20.390	21.332	22.372
	422	11.259		12.325		29.003		34.194		15.686	7.757	18.345
	333	7.157		7.929		19.243		23.039		10.029	3.151	11.898
	400	8.627	8.6	9.749		25.274	25.2	31.045		12.217		

Table 3.2: Comparison of the Darwin widths from StructureFactorTable and other sources. The same values for the characteristic wavelengths as in Table 3.1 were used.

Most likely, the values in Authier's table 15.2 ^[1, p. 447] denote δ_{os} . These were therefore doubled in Table 3.2 in order to make comparisons. We see that the computed values are in general agreement with the other sources, except for some of Darwin widths provided by Pike and Sabatier ^[20, p. 1121], which are close to exactly half of our values. Discrepancies are addressed to different sources for input data.

3.1.2 Intensity comparison

Each sample consists of six data subsets with name format x_y_z . The three parameters denote by which amount of millimetres the detector was shifted in the corresponding direction. Values used in this project are listed in Table 3.3 along with the number of reflections found with each setting.

Setting	Sample A	Sample B	Sample C	Sample D	Sample E
0_0_0	287	303	300	312	311
0_0_90	270	275	274	278	276
0_100_0	102	118	118	113	125
0_100_90	137	141	130	135	147
0_200_0	50	46	51	52	46
0_200_90	61	64	75	79	67
<i>Total</i>	907	947	948	969	972

Table 3.3: The amount of reflections after data reduction in *CrysAlis* for a given sample and setting.

Details on the *CrysAlis* procedure may be read in subsection 6.2.1 of appendix B. We will be using output generated from `StructureFactorTable` as reference values. These are presented in Figure 3.2.

(hkl)	Structure factor $ F_{hkl} $	Phase ϕ_{hkl} [°]	Bragg angle θ_B [°]	Pendellösung distance Λ_0 [μm]	Darwin width $2\delta_{os}$ [μrad]
(220)	68.193	-179.570	10.335	37.393	10.270
(111)	59.351	-179.640	6.307	43.408	14.447
(400)	57.062	-179.500	14.697	43.938	6.180
(422)	49.442	0.560	18.103	49.830	4.449
(311)	44.694	-179.540	12.144	56.697	5.776
(440)	43.209	0.621	21.027	55.993	3.429
(331)	38.177	0.523	16.050	65.248	3.819
(620)	37.976	0.685	23.650	62.522	2.747
(444)	33.554	-179.250	26.068	69.391	2.259
(511)	33.214	0.582	19.243	73.679	2.837
(333)	33.214	0.582	19.243	73.679	2.837
(642)	29.803	-179.180	28.337	76.551	1.896
(531)	29.091	0.644	22.039	82.589	2.223
(800)	26.609	0.890	30.492	83.939	1.618
(533)	25.619	-179.290	24.578	92.010	1.800
(822)	23.878	-179.040	32.562	91.488	1.399
(660)	23.878	-179.040	32.562	91.488	1.399

Figure 3.2: Output from the mentioned *Mathematica* function serving as reference for the subsequent analysis.

The wavelength applied to the function, $\lambda = 0.68894 \text{ \AA}$, was extracted from the header information of the first `.cbf` file in each data directory belonging to the this project.

When comparing the six different detector orientations in Table 3.3 we see that the most amount of reflections were obtained with the 0_0_0 setting; we will therefore be using this setting exclusively in the following analysis. The *Mathematica* function `IntensityTable` has been written for the task of extracting desired information from the reflection files (`.hkl`). The function gathers symmetry equivalent reflections at a single row in a table along with some statistics. Input example:

```
IntensityTable[{"silicon", "m3m", {h_, k_, l_} /; OddQ[h] || Divisible[h + k + l, 4]}, file]
```

Figure 3.3: Input example for the `IntensityTable` function. The first three arguments (in the curly bracket) have the same function as in `StructureFactorTable`. The next argument, `file`, represents the path to an `.hkl` file. The condition on the Miller indices are used to remove reflections that should be systematically absent.

(hkl)	Intensity [counts]	Uncertainty [counts]	Tally	Range (min; max)	Relative span from middle
(400)	302,105	9,213	10	(263,369; 359,524)	16%
(422)	290,509	7,093	29	(234,183; 355,750)	21%
(440)	288,375	9,692	8	(245,688; 320,673)	13%
(220)	259,799	14,452	10	(212,089; 336,725)	24%
(620)	255,654	8,935	16	(207,929; 346,015)	27%
(444)	225,244	4,469	6	(210,815; 238,629)	6%
(331)	214,718	4,243	30	(168,749; 251,939)	19%
(311)	212,078	2,877	42	(178,398; 263,524)	20%
(333)	199,318	5,577	6	(174,890; 210,979)	9%
(511)	199,021	4,655	33	(151,641; 263,242)	28%
(111)	198,894	4,515	12	(174,190; 224,184)	13%
(642)	188,820	5,489	8	(166,000; 213,356)	13%
(531)	175,507	2,651	44	(147,942; 218,718)	20%
(533)	154,454	3,654	12	(132,497; 178,059)	15%
(711)	144,927	6,132	8	(121,304; 167,211)	16%
(551)	130,708	2,203	13	(120,556; 149,297)	11%

(a) Si_A(0_0_0).

(hkl)	Intensity [counts]	Uncertainty [counts]	Tally	Range (min; max)	Relative span from middle
(220)	222,807	5,786	16	(181,201; 264,868)	19%
(400)	213,571	10,211	11	(157,574; 254,739)	23%
(422)	199,955	5,448	32	(129,283; 260,631)	30%
(440)	181,192	3,973	8	(167,151; 204,462)	10%
(620)	142,295	4,422	17	(121,396; 177,051)	20%
(111)	140,880	9,650	16	(67,650; 192,591)	44%
(331)	121,323	3,637	36	(44,562; 160,482)	48%
(444)	119,077	8,427	5	(93,844; 139,717)	19%
(311)	114,014	5,733	38	(31,526; 171,739)	61%
(333)	106,266	3,361	12	(88,291; 121,073)	15%
(642)	102,616	4,654	5	(95,036; 119,544)	12%
(511)	99,940	3,544	30	(54,606; 123,738)	35%
(531)	85,656	1,589	44	(54,009; 110,484)	33%
(533)	71,091	1,382	14	(65,973; 86,875)	15%
(711)	63,214	2,090	12	(52,012; 70,332)	14%
(551)	62,042	1,690	14	(53,246; 70,931)	14%
(731)	58,925	559	1	(58,925; 58,925)	0%
(553)	46,594	567	1	(46,594; 46,594)	0%

(b) Si_B(0_0_0).

(hkl)	Intensity [counts]	Uncertainty [counts]	Tally	Range (min; max)	Relative span from middle
(400)	258,704	9,121	12	(215,109; 317,193)	20%
(422)	250,687	5,654	31	(209,264; 323,202)	23%
(220)	246,201	6,453	16	(207,404; 307,981)	20%
(440)	233,294	7,163	10	(213,318; 297,072)	18%
(620)	195,678	4,274	18	(169,061; 227,685)	15%
(311)	180,074	4,045	40	(143,539; 238,198)	26%
(444)	179,132	9,778	4	(159,413; 206,410)	13%
(331)	169,414	3,893	30	(135,505; 223,353)	26%
(511)	161,820	2,787	35	(135,046; 193,173)	18%
(111)	159,127	6,988	12	(129,985; 218,639)	28%
(333)	158,878	4,041	12	(144,557; 186,123)	13%
(642)	141,999	3,584	5	(133,599; 153,972)	7%
(531)	135,788	2,125	40	(117,571; 172,886)	20%
(533)	116,826	3,446	10	(101,465; 138,141)	16%
(551)	95,894	2,315	14	(81,552; 110,893)	15%
(711)	94,387	2,736	10	(82,025; 104,639)	12%
(731)	78,147	1,690	1	(78,147; 78,147)	0%

(c) Si_C(0_0_0).

(hkl)	Intensity [counts]	Uncertainty [counts]	Tally	Range (min; max)	Relative span from middle
(220)	358,444	24,531	14	(210,211; 542,258)	46%
(422)	347,456	12,053	27	(215,973; 453,606)	34%
(440)	290,903	15,770	16	(178,865; 368,165)	33%
(620)	247,137	8,286	15	(183,806; 310,318)	26%
(400)	239,077	37,579	8	(112,751; 378,785)	56%
(111)	233,713	15,880	16	(162,820; 381,803)	47%
(444)	211,417	11,331	6	(167,676; 245,089)	18%
(311)	211,347	11,055	47	(82,774; 353,284)	64%
(511)	202,272	7,390	20	(130,918; 253,109)	30%
(331)	198,119	11,164	36	(79,745; 317,080)	60%
(333)	187,903	11,070	8	(151,479; 238,309)	23%
(642)	165,683	5,842	12	(129,936; 197,875)	21%
(531)	161,882	3,246	43	(102,078; 217,798)	36%
(533)	132,094	3,215	18	(98,637; 151,789)	20%
(711)	105,292	2,616	15	(87,008; 121,973)	17%
(551)	101,279	5,097	8	(80,461; 121,397)	20%
(731)	80,323	5,839	2	(74,722; 86,411)	7%

(d) Si_D(0_0_0).

(hkl)	Intensity [counts]	Uncertainty [counts]	Tally	Range (min; max)	Relative span from middle
(220)	258,704	9,121	12	(215,109; 317,193)	20%
(422)	250,687	5,654	31	(209,264; 323,202)	23%
(220)	246,201	6,453	16	(207,404; 307,981)	20%
(440)	233,294	7,163	10	(213,318; 297,072)	18%
(620)	195,678	4,274	18	(169,061; 227,685)	15%
(311)	180,074	4,045	40	(143,539; 238,198)	26%
(444)	179,132	9,778	4	(159,413; 206,410)	13%
(331)	169,414	3,893	30	(135,505; 223,353)	26%
(511)	161,820	2,787	35	(135,046; 193,173)	18%
(111)	159,127	6,988	12	(129,985; 218,639)	28%
(333)	158,878	4,041	12	(144,557; 186,123)	13%
(642)	141,999	3,584	5	(133,599; 153,972)	7%
(531)	135,788	2,125	40	(117,571; 172,886)	20%
(533)	116,826	3,446	10	(101,465; 138,141)	16%
(551)	95,894	2,315	14	(81,552; 110,893)	15%
(711)	94,387	2,736	10	(82,025; 104,639)	12%
(731)	78,147	1,690	1	(78,147; 78,147)	0%

(e) Si_E(0_0_0).

Figure 3.4: Tables over the intensities for all the 0_0_0 detector settings, sorted by decreasing value of intensity. The «Intensity» column is the weighted mean of the equivalents. The fourth «Tally» column denotes the number of symmetry equivalent reflections in the specific row. «Range» gives the smallest and largest intensities within the set, and the final column gives the middle value in a set of equivalent reflections divided by the weighted mean.

Although modulus of the structure factor has been used in Figure 3.2 and photon counts in Figure 3.4, the relative intensities of the various reflections should still be the same. For these silicon crystals we were unable to acquire details on the absorption frame scaling by *CrysAlis* and do not have any detailed assessment of the crystal shapes. This limits our ability to come with decisive conclusions. Some macroscopic details on the six silicon samples are listed in Table 3.4.

We note, however, that order of the strongest reflections are shuffled both among the samples and in comparison to the reference values. For instance, observe that in sample A and C the 220 reflection ranks fourth and third, respectively, despite being strongest in Figure 3.2. We also see that 111 appear to be relatively weak in all samples. If we compare sample A with sample D and take their sizes into account, we see that two mentioned reflections advance in the strength order with decreasing crystal size. These are typical signs of dynamical effects.

A *Mathematica* procedure has been written by Thorkildsen that performs a data reduction independent of *CrysAlis*. Tables corresponding to Figure 3.4 can be found in Figure 6.1 in appendix C. A comparison between the two sets of tables show that more reflections are found by Thorkildsen's method and that the relative spans from

Sample	Description	Dimensions
Si_A	Big sphere/ellipsoid	0.5 mm
Si_B	Pronounced axis	≤ 0.3 mm
Si_C	Arrowhead	≤ 0.3 mm
Si_D	Thin sheet	≈ 50 by 80 μm
Si_E	Wedge shaped	≤ 50 μm

Table 3.4: Shape descriptions of silicon crystals and approximate dimensions.

middle» are smaller. The order of most intense reflections in Figure 6.1 do not match the reference order nor the corresponding orders in Figure 3.4. Decline of strong reflections is still visible.

Inconsistency within same data sets

It was discovered that reprocessing the same data sets would produce different reflection files every time. Also performing the data reduction again on the same *CrysAlis* project would give different results. A case with `Si_E_0_0_0` is presented in Figure 3.5.

(hkl)	Intensity [counts]	Uncertainty [counts]	Tally	Range (min; max)	Relative span from middle
(220)	372,564	22,838	14	(226,229; 522,440)	40%
(422)	353,822	13,067	27	(232,338; 483,552)	36%
(440)	318,943	12,076	16	(201,610; 382,387)	28%
(400)	254,202	40,146	8	(118,162; 399,349)	55%
(620)	251,171	8,176	15	(188,772; 301,814)	23%
(111)	234,337	12,259	16	(169,924; 324,339)	33%
(311)	213,477	11,772	47	(89,179; 391,777)	71%
(511)	212,221	7,378	20	(122,286; 259,918)	32%
(444)	211,032	8,365	6	(177,406; 234,177)	13%
(333)	202,543	11,890	8	(157,822; 254,728)	24%
(331)	182,826	13,461	36	(34,771; 324,544)	79%
(642)	161,631	4,926	12	(134,891; 191,043)	17%
(531)	159,809	3,047	43	(91,836; 210,233)	37%
(533)	130,526	3,047	18	(98,550; 148,517)	19%
(711)	105,599	2,655	15	(89,733; 122,784)	16%
(551)	101,770	4,593	8	(80,337; 116,398)	18%
(731)	80,400	2,605	2	(77,903; 83,118)	3%

(a) Third run.

(hkl)	Intensity [counts]	Uncertainty [counts]	Tally	Range (min; max)	Relative span from middle
(422)	378,538	13,513	27	(256,172; 499,099)	32%
(440)	374,626	16,204	16	(267,988; 479,259)	28%
(220)	353,777	19,802	14	(252,854; 496,112)	34%
(620)	275,012	9,116	15	(228,671; 345,382)	21%
(444)	271,981	12,037	6	(237,337; 323,851)	16%
(400)	245,735	38,327	8	(115,354; 384,922)	55%
(511)	238,924	7,174	20	(191,010; 287,902)	20%
(331)	225,694	9,006	36	(119,063; 320,373)	45%
(642)	222,096	10,879	12	(161,232; 270,576)	25%
(333)	220,824	17,010	8	(154,279; 288,663)	30%
(311)	220,634	9,705	47	(99,503; 337,271)	54%
(111)	199,319	11,276	16	(131,059; 272,346)	35%
(531)	192,747	4,149	43	(137,711; 257,049)	31%
(533)	166,802	7,139	18	(112,416; 221,046)	33%
(711)	137,485	4,166	15	(108,686; 168,342)	22%
(551)	135,190	5,387	8	(113,859; 150,547)	14%
(731)	107,170	18,303	2	(89,583; 126,218)	17%

(b) Fourth run.

(hkl)	Intensity [counts]	Uncertainty [counts]	Tally	Range (min; max)	Relative span from middle
(422)	375,558	13,099	27	(249,847; 520,978)	36%
(440)	351,405	16,748	16	(189,473; 416,217)	32%
(220)	314,622	25,901	14	(151,523; 503,279)	56%
(444)	274,076	18,247	6	(218,003; 329,158)	20%
(620)	270,512	8,334	15	(241,075; 352,925)	21%
(400)	255,527	37,221	8	(114,424; 386,270)	53%
(333)	220,652	15,168	8	(153,245; 281,894)	29%
(511)	219,988	8,215	20	(179,533; 283,672)	24%
(311)	211,038	10,515	47	(84,355; 363,221)	66%
(642)	206,311	8,263	12	(163,851; 256,027)	22%
(111)	197,276	10,256	16	(150,790; 270,692)	30%
(331)	188,305	14,366	36	(36,067; 310,017)	73%
(531)	185,514	3,499	43	(131,684; 226,408)	26%
(533)	160,213	4,854	18	(124,412; 205,520)	25%
(551)	131,141	6,049	8	(109,560; 154,386)	17%
(711)	129,438	4,199	15	(99,577; 153,063)	21%
(731)	93,049	3,911	2	(89,289; 97,117)	4%

(c) Sixth run.

(hkl)	Intensity [counts]	Uncertainty [counts]	Tally	Range (min; max)	Relative span from middle
(220)	400,768	18,062	14	(325,107; 545,922)	28%
(422)	326,268	20,353	27	(123,557; 475,620)	54%
(440)	296,607	16,080	16	(191,702; 386,308)	33%
(620)	252,205	8,706	15	(189,452; 325,109)	27%
(400)	251,622	38,497	8	(119,012; 411,110)	58%
(111)	248,828	16,005	16	(170,813; 426,174)	51%
(311)	235,962	10,863	47	(125,846; 405,553)	59%
(511)	213,697	6,316	20	(139,981; 256,428)	27%
(331)	212,325	9,737	36	(110,513; 334,516)	53%
(444)	211,072	9,013	6	(175,792; 235,075)	14%
(333)	196,804	11,767	8	(149,913; 235,053)	22%
(642)	163,529	5,310	12	(129,623; 191,725)	19%
(531)	163,489	2,966	43	(120,937; 212,033)	28%
(533)	132,485	3,056	18	(95,147; 148,066)	20%
(711)	105,565	2,578	15	(86,808; 126,369)	19%
(551)	102,113	3,793	8	(87,300; 114,710)	13%
(731)	79,932	2,311	2	(77,717; 82,342)	3%

(d) Seventh run.

(hkl)	Intensity [counts]	Uncertainty [counts]	Tally	Range (min; max)	Relative span from middle
(422)	395,375	15,126	27	(261,237; 550,753)	37%
(440)	378,345	18,164	16	(201,435; 494,536)	39%
(220)	346,920	19,553	14	(257,022; 514,176)	37%
(620)	278,772	8,538	15	(245,249; 365,988)	22%
(444)	276,172	15,045	6	(231,010; 337,577)	19%
(400)	265,419	37,730	8	(116,707; 401,741)	54%
(511)	236,746	8,763	20	(188,964; 308,591)	25%
(331)	227,699	9,462	36	(116,220; 329,781)	47%
(333)	227,063	19,825	8	(150,675; 296,933)	32%
(311)	223,728	9,298	47	(121,115; 345,713)	50%
(642)	220,158	10,287	12	(169,717; 273,071)	23%
(111)	207,011	10,831	16	(145,899; 276,701)	32%
(531)	194,365	3,800	43	(136,131; 240,470)	27%
(533)	173,730	6,392	18	(130,862; 232,959)	29%
(551)	142,341	5,407	8	(119,882; 163,513)	15%
(711)	135,159	4,915	15	(103,768; 162,507)	22%
(731)	96,726	3,698	2	(93,168; 100,569)	4%

(e) Eight run.

(hkl)	Intensity [counts]	Uncertainty [counts]	Tally	Range (min; max)	Relative span from middle
(422)	368,259	14,902	27	(216,182; 516,207)	41%
(440)	341,295	18,748	16	(187,211; 446,722)	38%
(220)	320,635	26,252	14	(150,384; 490,762)	53%
(620)	269,591	8,150	15	(240,378; 348,847)	20%
(444)	258,564	14,484	6	(214,134; 316,486)	20%
(400)	249,856	40,854	8	(110,391; 417,225)	61%
(511)	231,023	9,342	20	(179,559; 295,103)	25%
(331)	226,680	8,258	36	(118,886; 307,028)	41%
(311)	217,742	9,472	47	(123,070; 363,759)	55%
(642)	207,166	9,426	12	(159,726; 256,645)	23%
(111)	199,315	10,084	16	(149,115; 266,985)	30%
(333)	194,052	24,975	8	(91,222; 280,277)	49%
(531)	193,209	4,583	43	(128,292; 267,185)	36%
(533)	164,204	5,667	18	(122,297; 214,709)	28%
(711)	131,768	3,775	15	(99,465; 150,677)	19%
(551)	126,619	7,687	8	(93,412; 155,292)	24%
(731)	105,195	8,729	2	(96,032; 113,511)	8%

(f) Ninth run.

Figure 3.5: Tables over the intensities for the `Si_E_0_0_0` detector setting, reprocessed more than nine times. The ninth run is the result of another data reduction of run number eight. The tables do not follow a natural sequence as some were test runs.

The peak tables of all the separate iterations have been verified to be identical. The observations raises concern with the credibility of the output data from *CrysAlis*. More on this topic will be discussed in section 4.1.

3.2 Thiourea-ferrocene room temperature analysis

A total of ten X-ray data sets were acquired in the thiourea-ferrocene project at the ESRF in November 2015. Each data set represents a different sample[†] and has been labelled with a prefix «Crystal» in the analysis. All samples were recorded using 0.1° increments in ϕ . The wavelength was 0.698 04 Å for all recordings. Table 3.5 below gives an overview of the data sets and the temperatures at which measurements have taken place.

Data subset	Crystal/sample ID									
	0	1	2	3	4	5	6	7	8	9
01	290	290	290	290	290	290	290	290	290	290
02	290	240	290		240			320		240
03		200			200			350		200
04		180			180			380		180
05		165			165			410		165
06		155			155					155
07		140			140					140
08		100			100					100
09		90			100					140
10		100			140					155
11		140			155					165
12		155			165					290
13		165			180					
14		180			200					
15		200			240					
16		240			290					
17		290			290					

Table 3.5: Thiourea-ferrocene data overview. The table shows data subset number (01-17) and the corresponding temperature, measured in kelvins, for a given data set. Data sets 2, 3, 5 and 6 (in grey frames) are pure ferrocene; the rest are thiourea-ferrocene. The complete data collection comprises 59 data subsets, each containing 3600 crystallographic images, amounting to a total of 527 GB of raw data.

The particular temperatures have been chosen relative to the calorimetry measurements done by Sorai et al.^[3], who observed five temperature-induced phase transitions at temperatures given in (2.47) (included here for convenience):

$$T_1 = 147.2 \text{ K}, \quad T_2 = 159.79 \text{ K}, \quad T_3 = 171.4 \text{ K}, \quad T_4 = 185.5 \text{ K}, \quad T_5 = 220 \text{ K}.$$

The purpose of the three temperature data series (data sets 1, 4 and 9) was to re-examine the reported phases from a crystallographic point of view. Also notice in Table 3.5 that measurements are taken symmetrically about the coldest point. This has been done to check whether the transitions are reversible. The crystal associated with data set 1 was also subjected to temperatures above 290 K, which constitutes data set 7.

The first step in the analysis is to establish an orientation matrix as accurate as possible for the data sets. Sources contributing to uncertainty in the measurements come from both the beamline instruments and the sample. The samples are inspected both visually and by test runs before doing any large scale data collections. If any twinning or particular flaw is uncovered, the sample may be useless for the specific project.

To arrange for the best starting point possible, the instrument parameters of the diffractometer have been refined at room temperature. The results from these 16 data subsets have been weighted according to their residual factors, and these final parameters are implemented on the initial setup for all data subsets of the temperature series.

Correcting the peak table

In order to obtain accurate values for the parameters of the diffractometer's instrument model, a correct peak table is needed. The task following the peak hunt is to remove incorrect reflections.

Unlike the silicon data, *CrysAlis* tends to split some of the reflections into multiple registrations. For instance, the peak table extract of `Crystal_2_(test1)_290K` in Table 3.6 shows that reflection $\bar{1}25$ has been registered

[†] The data sets labelled `Crystal_1` and `Crystal_7` are recorded from the same sample.

33 times. The corresponding plot in Figure 3.6 clearly shows two peaks. It appears that *CrysAlis* misinterpret the partial reflections, which have likely been moving slowly through the Ewald sphere. We would expect to measure a single reflection up to two times, depending on whether the scattered beams strike the detector. In this example only the two registrations labelled 1242 and 1332 ought to be kept.

All reflections in the peak table have to be processed in a systematic and in a semi-automatic manner due to the large number of peaks and data sets. The following rules are suggested for the general case:

1. Taking standpoint of the largest intensity value in the set of conflicting registrations (such as Table 3.6), entries with an intensity reading less than 85 % of this local maximum value will be deleted.
2. In this result, we take the maximum and all other registrations that are within 5° in ϕ to be a single *group*. The process is repeated until all registrations have been grouped.
3. For each group, all but the strongest registrations are deleted.

This procedure constitutes the algorithm behind `PeakTableHelper`.

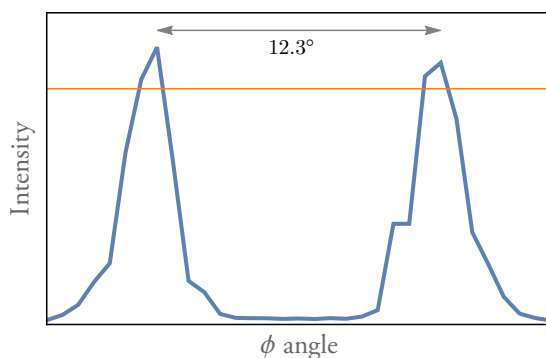


Figure 3.6: Plot of the intensity data from Table 3.6. The two peaks are 12.3° apart in ϕ . The orange line is placed at 0.85 times the maximum intensity of the set.

Obtaining refined instrument parameters

The handling of the peak table was the most time-consuming step in the data process, mainly due to *CrysAlis* lacking an effective method for removing bulks of reflections[†]. For other details concerning the procedure, please see subsection 6.2.2 of appendix B.

An overview of the refined instrument parameters for the individual room temperature sets may be found in Table 3.8 in appendix B. Some data sets were processed up to three times due to “unsatisfactory” results. For example, crystal 8 was processed a second time with the only difference being that the setting `pt num` (peak table entry number) in `CrysAlis` Command shell Options RED Peak table was changed from 20 000 to 200 000. This was done because a relatively large residual factor of 3.37 % was observed the first time, and it was suspected that too few peaks were found. As repeated reflections were not thoroughly removed the second time, a third analysis was needed. The vast amount of reflections found in this particular sample might indicate a flawed crystal (the crystal is analysed further in section 3.6). If we look at the initial amount of reflections in accordance with the orientation matrix, however, 9570 fit the third time compared to 6550 the second time. About 3000 reflections were kept in the end in both cases.

[†] A possible workaround seems to be possible with use of the *CrysAlis* command `wd t oldascii`, but this will have to be added to the *Xray* package at a later time.

1211	-1	-2	5	233.45	65
1214	-1	-2	5	233.85	145
1225	-1	-2	5	234.35	302
1230	-1	-2	5	235.25	652
1232	-1	-2	5	235.85	941
1236	-1	-2	5	236.45	2648
1241	-1	-2	5	236.95	3772
1242	-1	-2	5	237.25	4269
1249	-1	-2	5	237.75	2525
1256	-1	-2	5	238.45	669
1259	-1	-2	5	238.95	495
1266	-1	-2	5	240.45	161
1270	-1	-2	5	241.45	99
1275	-1	-2	5	242.25	95
1279	-1	-2	5	242.95	93
1281	-1	-2	5	243.25	84
1285	-1	-2	5	243.55	90
1288	-1	-2	5	243.85	82
1291	-1	-2	5	244.25	95
1295	-1	-2	5	244.65	86
1302	-1	-2	5	245.45	120
1304	-1	-2	5	247.25	219
1316	-1	-2	5	248.75	1549
1326	-1	-2	5	248.75	1549
1329	-1	-2	5	249.25	3822
1332	-1	-2	5	249.55	4029
1337	-1	-2	5	250.15	3162
1341	-1	-2	5	250.95	1420
1344	-1	-2	5	251.45	935
1349	-1	-2	5	252.15	424
1352	-1	-2	5	252.85	166
1356	-1	-2	5	253.55	97
1357	-1	-2	5	253.75	59

Table 3.6: Extract from an unbalanced peak table showing all registrations of $\bar{1}\bar{2}5$. Left-most column contains registration numbers set by *CrysAlis*. Fourth column contains ϕ values and last column intensity values. The rows with green background correspond to the two local peaks.

A second proceeding with crystals 3 and 4 was also needed, as neither of these were cleared of multiple-registered reflections the first time. In all cases, we observe in Table 3.8 that an improvement in the `res` factor results from this peak table trimming.

Afterwards, the instrument parameters were weighted using the residuals as uncertainties. In cases where data has been analysed multiple times, only the latest proceeding was used to represent the data subset in the weighting. The refined instrument parameters are presented in Table 3.7. The uncertainties in the weighted means are standard deviations $\tilde{\sigma}_{\bar{x}}$ calculated according to

$$\tilde{\sigma}_{\bar{x}} = \sqrt{\frac{1}{\sum_{i=1}^n \sigma_i^{-2}} \cdot \frac{1}{n-1} \sum_{i=1}^n \frac{(x_i - \bar{x})^2}{\sigma_i^2}}, \quad (3.3)$$

where x_i denotes the i 'th refinement of instrument parameter x and residual factors have been used in place of σ_i . \bar{x} represents the weighted mean of the relevant parameter;

$$\bar{x} = \frac{\sum_{i=1}^n w_i x_i}{\sum_{i=1}^n w_i}, \quad w_i = \frac{1}{\sigma_i^2}. \quad (3.4)$$

		Weighted values	
Parameters		Best estimate	With uncertainty
b2	[10 ⁻³ °]	-2.189	-2 ± 4
d1	[10 ⁻³ °]	56.858	57 ± 6
d2	[10 ⁻³ °]	-3.627	-4 ± 4
d3	[°]	-0.138 926	-0.139 ± 0.014
x0	[px]	26.9703	27.0 ± 0.2
y0	[px]	741.182	741.18 ± 0.07
dd	[mm]	146.391	146.39 ± 0.04

Table 3.7: Refined instrument parameters. The best estimates will be used when setting the instrument model in advance.

Table 3.8 below gives an overview of all refinements. We see that the residual factors are less than one percent, giving us confidence in the refined parameters of the diffractometer given in Table 3.7.

	n0	n	res [%]	b2 [°]	d1 [°]	d2 [°]	d3 [°]	x0 [px]	y0 [px]	dd [mm]
[2nd]Crystal_3_290K	4762	1768	0.2985	-0.024 523	0.085 068	-0.022 558	-0.054 378	28.134	741.022	146.232
[2nd]Crystal_4_(01)_290K	3689	1607	0.6486	-0.025 714	0.110 336	-0.088 672	0.127 106	30.844	742.212	145.544
[2nd]Crystal_8_290K	44 640	3064	1.5041	-0.016 241	0.017 191	-0.034 943	0.004 532	28.708	741.893	145.405
[3rd]Crystal_8_290K	44 640	3019	0.4845	-0.031 541	0.024 471	-0.044 801	-0.188 891	26.014	741.914	146.891
Crystal_0_(test1)_290K	10 248	9719	0.2038	0.007 022	0.048 421	0.006 481	-0.160 705	26.624	741.336	146.454
Crystal_0_(test2)_290K	8569	5957	0.3155	0.008 930	0.047 939	0.000 074	-0.161 940	26.647	741.454	146.434
Crystal_1_(01)_290K	7701	7207	0.1946	-0.000 513	0.048 481	-0.002 517	-0.163 955	26.535	741.323	146.408
Crystal_1_(17)_290K	4570	4333	0.2525	-0.006 725	0.046 776	-0.009 169	-0.147 439	26.918	741.150	146.401
Crystal_2_(test1)_290K	1954	1732	0.2405	0.003 949	0.052 202	0.004 213	-0.111 014	27.396	740.954	146.350
Crystal_2_(test2)_290K	2807	2375	0.1796	0.004 432	0.052 698	0.004 705	-0.120 834	27.280	740.942	146.368
Crystal_3_290K	4762	2465	1.0638	-0.022 279	0.088 543	-0.021 666	0.037 892	29.619	740.965	146.038
Crystal_4_(01)_290K	3689	2287	0.8131	-0.017 721	0.100 468	-0.075 604	0.096 920	30.363	742.073	145.507
Crystal_4_(16)_290K	3645	2602	0.9111	-0.024 057	0.182 666	-0.019 387	-0.149 067	26.889	740.960	146.337
Crystal_4_(test)_290K	3821	2754	0.9013	-0.053 303	0.153 978	-0.012 153	-0.259 439	25.521	740.431	146.418
Crystal_5_290K	4411	3904	0.6286	0.012 640	0.056 828	0.019 653	-0.114 202	27.539	740.765	146.310
Crystal_6_290K	3012	2868	0.4537	-0.014 718	0.043 892	-0.008 874	-0.127 558	27.157	741.565	146.415
Crystal_7_(01)_290K	7628	5264	0.4466	0.003 844	0.053 132	0.006 262	-0.133 507	27.028	741.139	146.391
Crystal_9_(01)_290K	7099	3732	0.5498	0.021 999	0.104 597	0.010 141	-0.345 906	24.279	741.115	146.458
Crystal_9_(test)_290K	6893	3621	0.4709	-0.043 008	0.107 532	-0.031 533	-0.174 748	26.278	740.906	146.497

Table 3.8: Parameters acquired from careful inspection of the room temperature data. The `n0` column shows the number of reflections in the peak table that match the initial lattice (after peak hunt and automatic lattice determination). `n` shows the corresponding final number of reflections (after refinements). Residual factors are listed in the `res` column. The remaining columns display the instrument parameters in *CrysAlis*. The shorthand labels in the title row, descriptions may be found in Table 2.2.

Observe that there is a correlation between parameters of the instrument model, especially `d3` and `dd`.

3.3 Ferrocene

Recall that out of the ten crystals studied at the ESRF four of them were found to be pure ferrocene (crystals 2, 3, 5 and 6). The samples were recognised to be ferrocene by their lattice parameters from preliminary analyses.

Absorption correction

We may check if the absorption correction seems to be in order. This was also an opportunity to get acquainted with the available options regarding absorption in *CrysAlis*.

The project files of the mentioned data sets[†] were kept aside, then the data sets were reprocessed using the refined values from Table 3.7. In the case of crystal 2, two data sets were collected at room temperature; the others contained only one data set each (see Table 3.5). At this point, *binned* versions of the four data sets in question were made with the *Pylatus image converter* application in the *SNBL ToolBox*^[63] (see Figure 2.22). The crystallographic image files are compressed in the sense that every five images are merged into one, cutting the number of *.cbf* files from 3600 to 720. The binning reduces the processing time at the cost of a little information loss.

The results from automatic absorption processing by *CrysAlis* is shown in Figure 3.7 on the right. We see that for the most part absorption correction is handled smoothly. The profiles of the curves correlate to variations in path length due to crystal rotation. The plot associated with crystal 3 stands out as incorrectly processes, as several frame scaling factors closed to a pronounced peak have been set to zero. The reason for this absorption curve being different from the other three variants is probably due to this crystal's particular shape or misaligned mounting on the goniometer, but the errors with the scaling factors are probably linked to an issue with the scaling algorithm and this particular sample.^[51, p. 70]

It is possible to choose some manual settings for the absorption correction procedure. After data reduction has been completed, one may go to *CrysAlis* » *Inspect data reduction results* » *Refinalize* and tweak various parameters. In the case of crystal 3 the best results were accomplished when setting **Frame scaling** to either 5 or 8 frames per scale and refining the (Debye–Waller) *B*-factors with either 10 or 15 frames per factor. In Figure 3.8 we see the binned version of crystal 3 was successfully cleared of the zero scalings; the non-binned version was not. Increasing or decreasing the **Restraint (ESD)**, which «represents expected standard deviation of differences between adjacent scales»^[47], did not yield any improvement either.

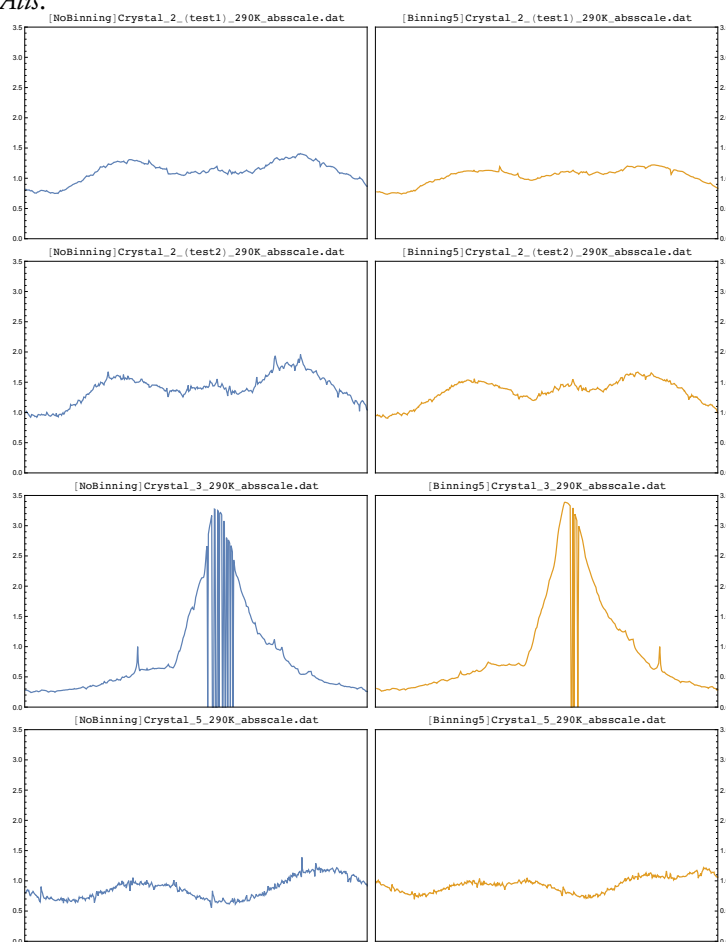


Figure 3.7: Results of scaling corrections done by *CrysAlis*' so-called *scale3 abspack*, with a scaling factor plotted against frame number. Results for unbinned data are shown on the left; binned on the right. The module scales the *.hkl* file in order to compensate for effects like detector variations, crystal decay and absorption.^[47] Scalings seem to be in order for every crystal except number 3.

[†] Crystal 6 is not included, as it was discovered to be ferrocene after this absorption analysis.

A final attempt was made with a manual flux correction. First a monitor `.ini` file is generated with the *CrysAlis* command `xx monitorini fromrunlist` (monitor-ini-form-run-list). Next the values of that file, which are all initially set to 1.0000, need to be edited, and the *Mathematica* function `MonitorIni` was written for this purpose. Decreasing the frame values linearly from 1 to 0.75 was first tried, but a more purposeful approach would be to extract the registered flux values from the headers of `.cbf` files. This was done with the *Head Extractor* application in *SNBL Toolbox* and the content has been plotted in Figure 3.9. In order to load the altered monitor file, one has to select `Use file monitor values` after checking `Apply monitor renormalization` in *CrysAlis* `>Data reduction with options>>Step 3: Edit special parameters` (see Figure 2.19). Sadly, neither outcomes of these methods surpassed the manual corrections.

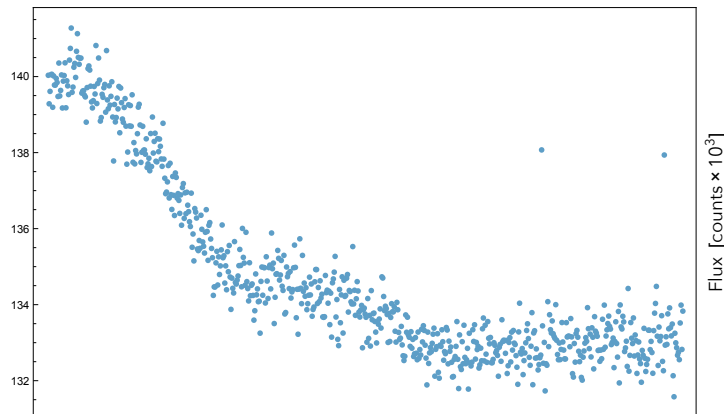


Figure 3.9: Plot over the incoming radiation flux on crystal 3. The flux is monitored by counting photons scattered vertically from a Kapton foil.

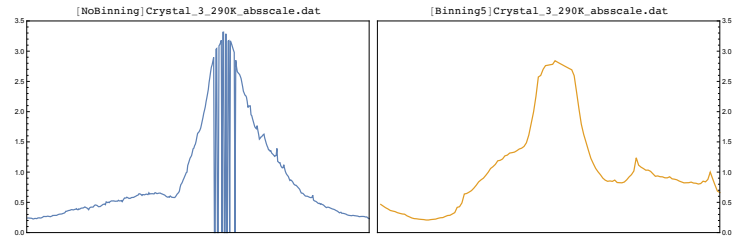


Figure 3.8: Best results obtained from scaling corrections with manual settings. Only the binned version was noticeably improved.

3.3.1 Further inspection of crystal 3

As refinement with different parameters of the absorption correction did not yield satisfactory results, the data was reprocessed in order to check the peaks more carefully. Results from the peak hunt are presented in Figure 3.10.

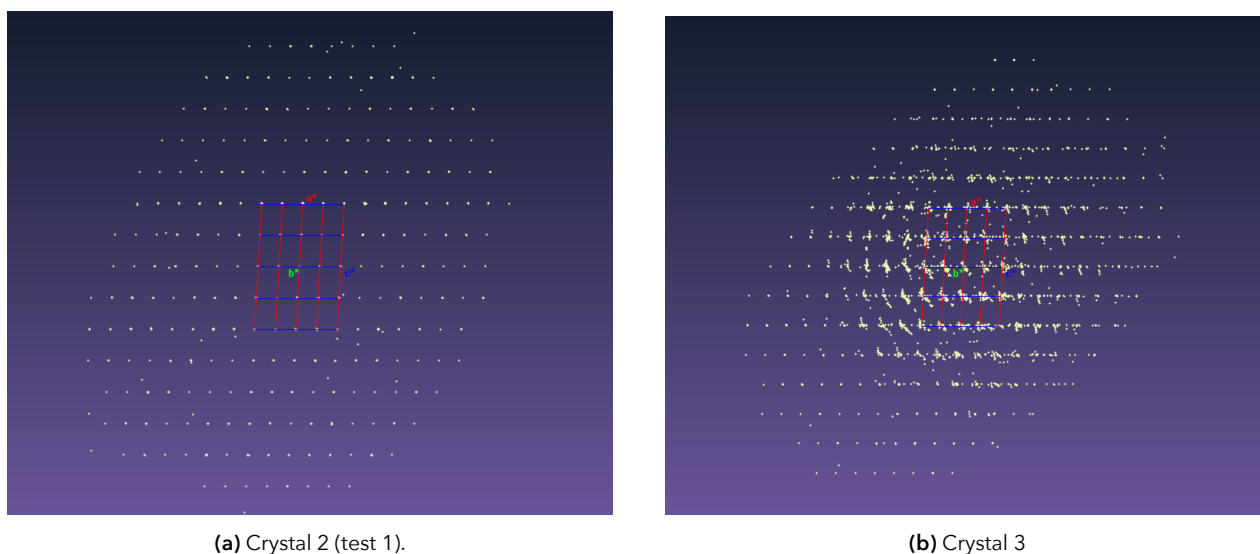


Figure 3.10: Screenshots from `Ewald explorer` immediately after peak hunt, showing reciprocal space in the \mathbf{b}^* direction. We see that crystal 3 has an additional streak pattern. Notice also that this pattern is asymmetric. The other two data subsets were similar to (a).

This time it was recognised that, when using the «auto analyse unit cell» method, the unit cell of crystal 3 matched only 62 % of the initially found peaks. The other four ferrocene crystals matched at least 95 %. Crystal 5 also showed a slight tendency of streaks, but the peak table was not much affected by the reindexation to 0.05 (reduced from 97 % to 88 %). `Ewald explorer` was unable to determine any meaningful twin component to the wrong peaks.

Apart from the streaks in crystal 3, the reflections fit the lattice quite well, and has about the same amount of peaks matching the orientation matrix as the others after refinements. It appears that the scaling module (`Scale3 abspack`, version 1.0.7) or the profile fitting module is unable to process this ferrocene sample correctly.

Using the `Unwarp` feature, reconstructions of reciprocal space were made. It was revealed that the mentioned streaks were unique to crystal 3, and could be seen in all of the crystallographic directions.

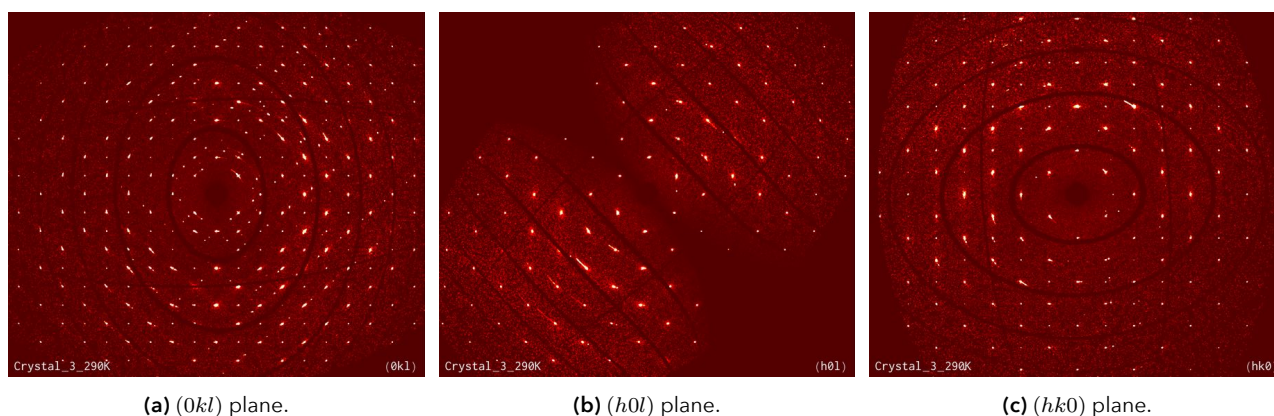


Figure 3.11: Reciprocal space reconstructions of crystal 3 at 0.8 Å resolution.

In addition to the streaks, notice also in Figure 3.11 that many of the peaks in the (0kl) and (hk0)-planes are “accompanied” by a very close reflections. This becomes even more apparent in Figure 3.12.

We observe that the reflections on the lattice can have up to three accompanying reflections, or satellites. Moreover, the specific orientation of the satellites tend to remain the same along a particular direction in reciprocal space. If

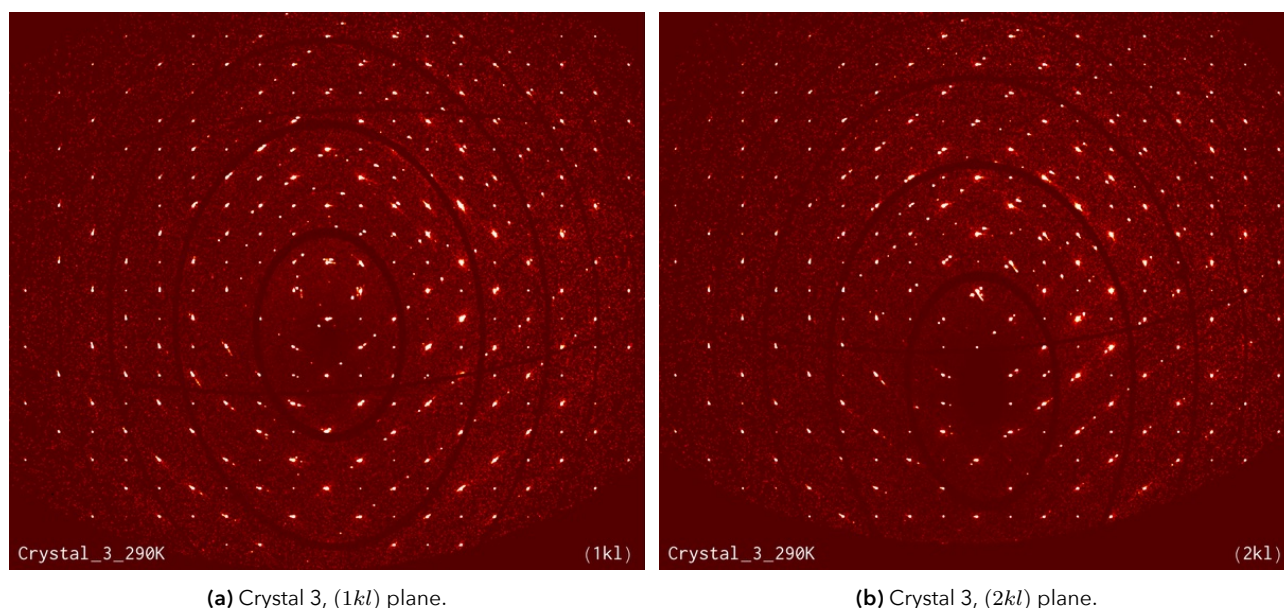


Figure 3.12: Reconstructions of reciprocal space for crystal 3. Note the local clustering of peaks around the lattice points.

we examine the images carefully, it seems like the reflections further out also have this property.

Intermediate reflections

Another feature of crystal 3 is that the streaks tend to be present also between integer Miller indices, especially in the \mathbf{a}^* and \mathbf{b}^* directions, where there are always some peaks in reflection condition (at least in steps of ± 0.1 units).

If we start in the $(0hk)$ plane and consider consecutive planes in the \mathbf{a}^* direction in steps of 0.05 units of that lattice parameter, a “line” of reflections being in reflection condition seems to be propagating in the plane, completing a full cycle in one unit of \mathbf{a}^* .

The streaks appear to have “tails” attached to the reflections. These tails will always be oriented the same way as a given reflection leaves and re-enters reflection condition. As we enter a reflection condition, some streaks will merge to a single reflection, while others will split into a reflection with two or three satellites.

The structure of crystal 3 appears to be modulated and incommensurate with the main structure. The [Ewald explorer](#) has an option for setting a so-called q -vector to describe the modulation, but experimentation with this was unsuccessful.

Of course, the reflections not belonging to the main lattice could simply be due to poor crystal quality.

A final remark on the ferrocene crystals is that the most intense and diffuse reflections linger out to about $h \pm 0.15$ and $k \pm 0.20$ and $l \pm 0.20$ for integer h, k, l . Also, crystal 5 had a significantly higher background in the reciprocal space reconstructions.

3.3.2 Structure solution

The structure of ferrocene has been solved, and the effect of binning has been checked as well. Structure solution and refinement was carried out in *Olex2*^[46]; a screenshot is shown in Figure 3.13. We see that *SHELXS* could only determine the iron atom in the asymmetric unit. After identifying parts of the cyclopentadienyl ring, the structure could be completely solved.

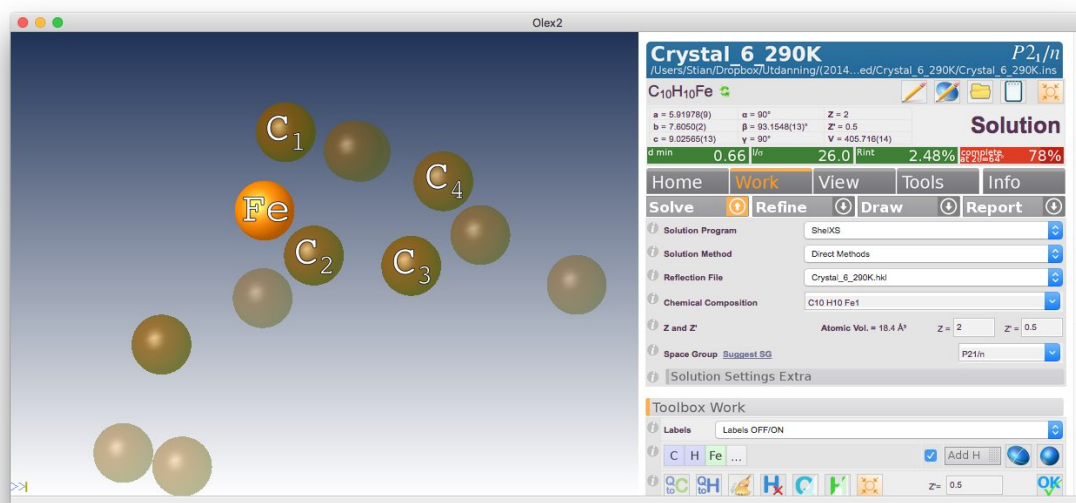


Figure 3.13: Main window of *Olex2*, showing the structure after solution by the *SHELXS* program. The bronze coloured spheres represent peaks of the electron density and serve as suggested atoms, and are labelled *Q* as the element type is unknown. Here four of them are recognised to be carbon atoms. The last one is found after subsequent refinement.

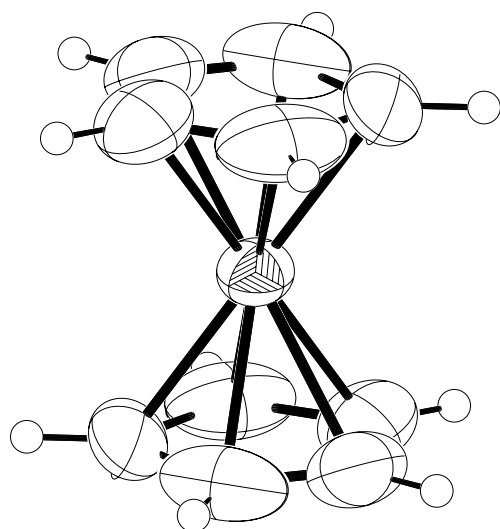
Employing *SHELXT*, however, succeed in finding the correct structure in all of the ten cases (the five data sets, with and without binning) immediately. In the final iterations of refinement, a weighting scheme with two parameters (suggested by the program) was engaged. Goodness parameters from the solution and refinements are presented in Table 3.9.

Sample	Crystal_2_test(1)				Crystal_2_test(2)			
Completeness	75 %				75 %			
Binned?	X		✓		X		✓	
R_{int} [%]	1.55		1.36		1.25		0.89	
I/σ	21.9		32.2		41.5		51.0	
Hydrogen?	X	✓	X	✓	X	✓	X	✓
GooF	1.138	1.128	1.162	1.125	1.140	1.140	1.149	1.137
R_w [%]	20.34	16.07	19.43	14.64	19.87	16.35	19.03	15.12
R [%]	5.84	5.15	5.54	4.80	5.87	5.24	5.54	4.88

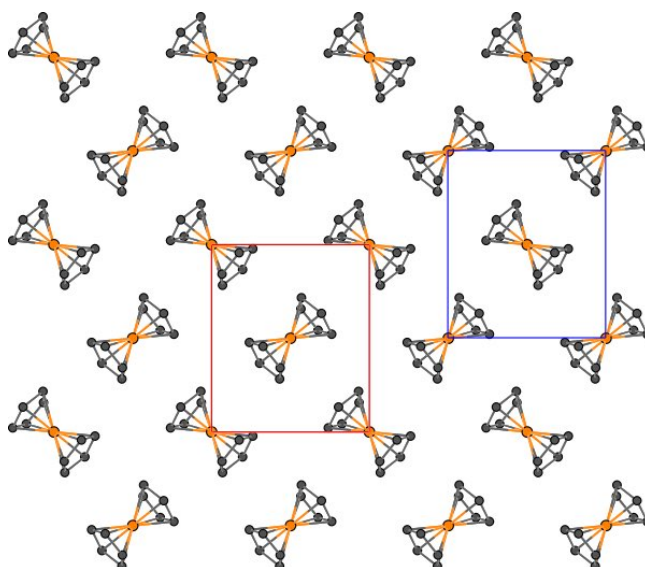
Sample	Crystal_3				Crystal_5				Crystal_6			
Completeness	66 %				64 %				78 %			
Binned?	X		✓		X		✓		X		✓	
R_{int} [%]	3.01		2.48		0.90		0.80		2.48		1.77	
I/σ	22.6		23.7		79.4		87.5		26.0		27.1	
Hydrogen?	X	✓	X	✓	X	✓	X	✓	X	✓	X	✓
GooF	1.157	1.157	1.015	1.029	1.224	1.211	1.217	1.213	1.176	1.185	1.152	1.128
R_w [%]	23.17	19.92	19.24	14.96	24.38	20.76	22.07	18.52	23.02	18.46	24.41	20.22
R [%]	6.78	6.25	5.73	4.97	8.54	7.99	7.32	6.76	7.49	6.70	7.61	6.87

Table 3.9: Parameters from the ferrocene refinement. Each block is for a particular data subset, which are divided into two halves for comparison between binned and unbinned versions. The GooF and R -factor (including only data with $I \geq 2\sigma(I)$) before and after adding hydrogen is also provided.

In addition to testing the effect of binning, when each structure had converged to a solution, hydrogen atoms were added using an automatic feature. We see that adding them decreased the R -factor by around 0.5 percentage points, while R_w dropped with about 4.



(a) Ferrocene molecule with anisotropic displacement parameters (except hydrogen).



(b) Ferrocene crystal structure along a^* . Red unit cell is used by crystals 2 and 3; blue cell by crystals 5 and 6.

Figure 3.14: Images of crystal 3 rendered by *Olex2*.

Weighted mean of the ferrocene lattice parameters are calculated to be:

$$a = 5.926(2) \text{ \AA}, \quad b = 7.611(3) \text{ \AA}, \quad c = 9.033(4) \text{ \AA}, \quad \beta = 93.160(7)^\circ \quad (3.5)$$

in the monoclinic space group $P2_1/n$ (# 14). This is the second cell choice according to the *International Tables, volume A*^[92, p. 187], whereas the values by Seiler and Dunitz^[69] in (2.42) are given in the third cell choice, $P2_1/a$ (with \mathbf{b} being the unique axis). Transformation of our values in (3.5) are given below, along with Seiler and Dunitz' values for convenience:

$$a' = 10.523(8) \text{ \AA}, \quad b' = 7.611(4) \text{ \AA}, \quad c' = 5.926(2) \text{ \AA}, \quad \beta' = 121.041^\circ. \quad (3.6)$$

$$a = 10.561(11) \text{ \AA}, \quad b = 7.597(8) \text{ \AA}, \quad c = 5.952(6) \text{ \AA}, \quad \beta = 121.02(12)^\circ. \quad (\text{S \& D})$$

The numbers are in reasonable agreement with Seiler and Dunitz'.

It was also seen that crystals 2 and 3 have been determined with the ferrocene in centre of the unit cell having its molecular axis coinciding (almost) with the space diagonal through the origin, while crystals 5 and 6 have axes almost coinciding with the $[\bar{1}\bar{1}1]$ direction. In the reciprocal space reconstructions of the two cases it is clear that the \mathbf{c}^* direction in crystals 5 and 6 is the \mathbf{b}^* direction in 5 and 6. When solving the structure we find the individual ferrocene molecules to be in the staggered conformation in all four crystals. This gives us, however, only a picture of the molecule on average. The relative large anisotropic displacement parameters of the carbon atoms also give an indication of a disordered state, in accordance with the literature.^[74]

Despite having the peculiar streaks, crystal 3 did not stand out in the structure solution.

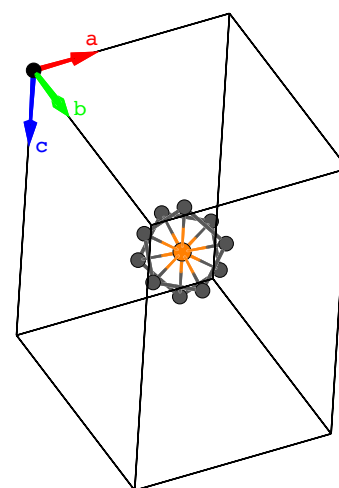


Figure 3.15: Viewing down the molecular axes of ferrocene (here: crystal 5), which is close to $[\bar{1}\bar{1}1]$.

3.4 Thiourea-ferrocene – crystal 1

17 data sets were recorded with this crystal while it was configured with a liquid nitrogen cryostat. The specific measurement points are listed in Table 3.5.

The initial procedure is the same for all data sets and may be reviewed in subsection 6.2.3. There are two main differences with this procedure compared to that for room temperature; the refined values for the instrument model are set immediately at startup, which leaves only the lattice parameters, a and c , and the rotation angles available for refinement. The second change is that *Ewald explorer* has been used to check for twinning. A graphic overview of the procedure for each data subset is given in Figure 2.11.

The automatic peak hunt usually found sufficient peaks, but at the colder temperatures unexpected cell identifications occurred. Whenever this particular issue arose, inspection with *Ewald explorer* often showed a sizeable void of reflections, or quite simply too few reflections. If unable to transform to the desired unit cell in *CrysAlis*, the peak hunt was redone using another method or specifying other threshold values.[†] As a “last resort”, it is possible to force the unit cell parameters or orientation matrix on the data (not used in this thesis).

Luckily, for this particular crystal it was possible to transform all data sets to the same configuration – which was hexagonal $6/m$ lattice, primitive centring – with the feature `[Lattice Wizard] >> [Lattice reduction]`. Even so, some special observations were made: The lattice parameter c was initially set to about 61.7 \AA for data subsets 03, 04 and 14 (temperatures 200 K, 180 K and 180 K). This value is more or less exactly five times larger than observed in the other data sets. This integer multiple of the cell length could be an indication of a commensurate structure. In this particular analysis, however, we strive for consistency among the data subsets. The “problem” was simply circumvented with the command:

```
um c 1 0 0 0 1 0 0 0 0.2,
```

which performs a user-specified transformation of the orientation matrix (in direct space).

Refining the instrument model (rotation angles and lattice parameters), reindexation, clearing the peak table of wrongly indexed reflections is straightforward.

From the two 290 K data subsets of crystal 1, we find our best estimates for the lattice parameters to be

$$a = (16.3691 \pm 0.0003) \text{ \AA}, \quad c = (12.4036 \pm 0.0004) \text{ \AA}. \quad (3.7)$$

These values are in accordance with those of Hough and Nicholson^[84] in (2.45). Uncertainties are taken from *CrysAlis*, then weighted means are calculated to get the result above.

Imposing a “common orientation”

After all 17 data subsets of `Crystal_1` have been processed using this procedure, the next step is to make sure they are all oriented the same way, so that comparisons will be more meaningful. Although they have the same unit cell, they may be rotated and/or mirrored compared to each other. The way to ascertain similar orientations is to compare the **UB** orientation matrices. If they are different, the three crystal rotation angles (`r1`, `r2` and `r3`) will also differ.

Two *Mathematica* functions now come into play: First, `RefinedValues` is needed to extract the matrices from the log files of *CrysAlis*. The first data set is (arbitrarily) chosen to provide the reference orientation, the orientation matrices of the others will have to be transformed to match the reference. This is done by `UBtransformation`, and the whole operation consists of four steps:

1. All Laue equivalent bases are calculated.
2. Every equivalent matrix is subtracted from the reference matrix.

[†] It was later found out that certain transformations between an orthorhombic and hexagonal cell could have given the desired results. The required transformation matrix is readily found in *The International Tables for Crystallography, volume A*^[92, p. 81].

3. The resulting matrices are squared element-wise, and the *largest* element of the matrix with the *smallest* total squared deviation is chosen as the correct matrix.
4. The corresponding Laue equivalent matrix is found. The transformation code for *CrysAlis* is printed.

A final note on the orientation process of crystal 1: In some cases, it was not possible to find any matching transformations. This was resolved by assuming a higher Laue symmetry. It appears that *CrysAlis* uses the symmetry of the lattice, $6/mmm$, rather than that of the crystal, which is $\bar{3}m$. This observation is attributed to an obverse–reverse twinning of the crystal (continued discussion in subsection 3.4.2).

3.4.1 Preliminary room temperature reconstructions of reciprocal space

At first, planes in reciprocal space of the kind

$$(hkl) : l \in \{-6, -5, -4, -3, -2, -1, 0, 1, 2, 3, 4, 5, 6\}. \quad (3.8)$$

were created. The diffraction pattern for a given l is identical to that of $-l$, so only non-negative l 's will be considered. The first six reconstructions are shown in Figure 3.16.

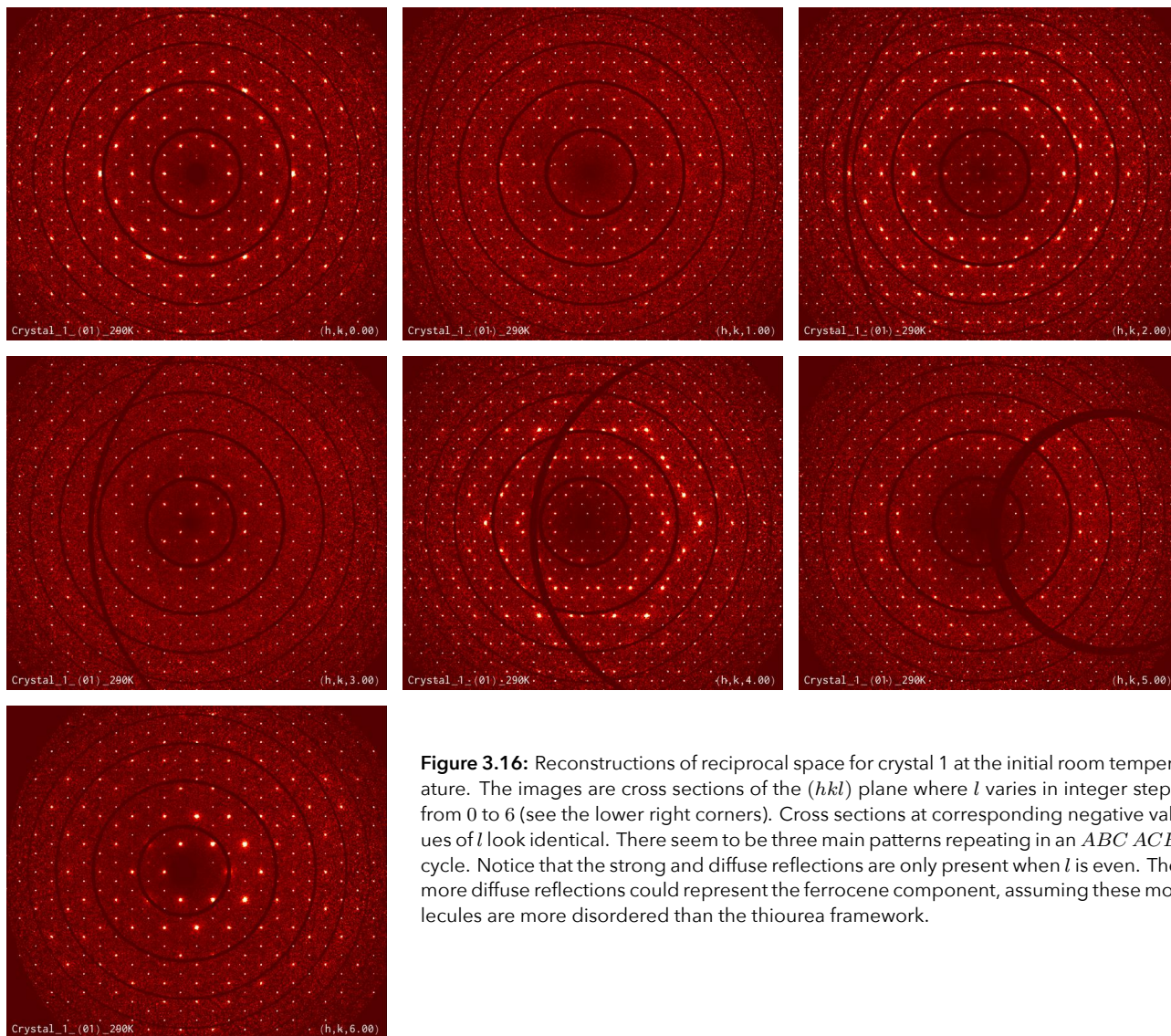


Figure 3.16: Reconstructions of reciprocal space for crystal 1 at the initial room temperature. The images are cross sections of the (hkl) plane where l varies in integer steps from 0 to 6 (see the lower right corners). Cross sections at corresponding negative values of l look identical. There seem to be three main patterns repeating in an $ABC\ ACB$ cycle. Notice that the strong and diffuse reflections are only present when l is even. The more diffuse reflections could represent the ferrocene component, assuming these molecules are more disordered than the thiourea framework.

It may not be obvious from Figure 3.16, but there are three distinct patterns repeating along l with a period of six units. If we call these patterns A , B and C , we have that

$$A : l \equiv 0 \pmod{3} \iff l \in \{\dots, 0, 3, 6, 9, 12, \dots\} \quad (3.9a)$$

$$B : l \equiv 1 \text{ or } 5 \pmod{6} \iff l \in \{\dots, 1, 5, 7, 11, 13, \dots\} \quad (3.9b)$$

$$C : l \equiv 2 \text{ or } 4 \pmod{6} \iff l \in \{\dots, 2, 4, 8, 10, 14, \dots\} \quad (3.9c)$$

Equivalently, the pattern is $ABC\ ACB$. Within one of these types, the main lattice remains the same. Patterns of type B and type C look almost the same, but more reflections are seen in type C and they are more intense.

3.4.2 Twinning of crystal 1

There are several observations that point to crystal 1 being twinned:

1. It does not have the space group $R\bar{3}c$ (#167) as indicated by the literature^[84].
2. The metric symmetry ($6/mmm$) is higher than the Laue symmetry ($6/m$).^[44, p. 121]
3. According to Herstein^[2, p. 200], thiourea will only form rhombohedral tunnel inclusion compounds, but this is not reflected in the space group, which was found to be $P6_3/mcm$ (#193) in an initial data reduction.
4. Comparison with crystals 4 and 9 (see ref)

Signs of reticular merohedry

It was discovered that all reflections would fit combinations of the conditions:

$$hkl : -h + k + l = 3n, \quad (\text{obverse}) \quad (3.10a)$$

$$hkl : h - k + l = 3n \quad (\text{reverse}) \quad (3.10b)$$

for various choices of l . These are the reflection conditions for a rhombohedrally centred cell in the obverse and reverse setting, respectively.^[92, p. 29] The function `ReflectionConditionCheck` was written in order to easily extract reflections from raster graphics, i.e. the reconstruction images, and show which adhered to a specific reflection condition. More details of this function will be given in subsection 6.3.2.

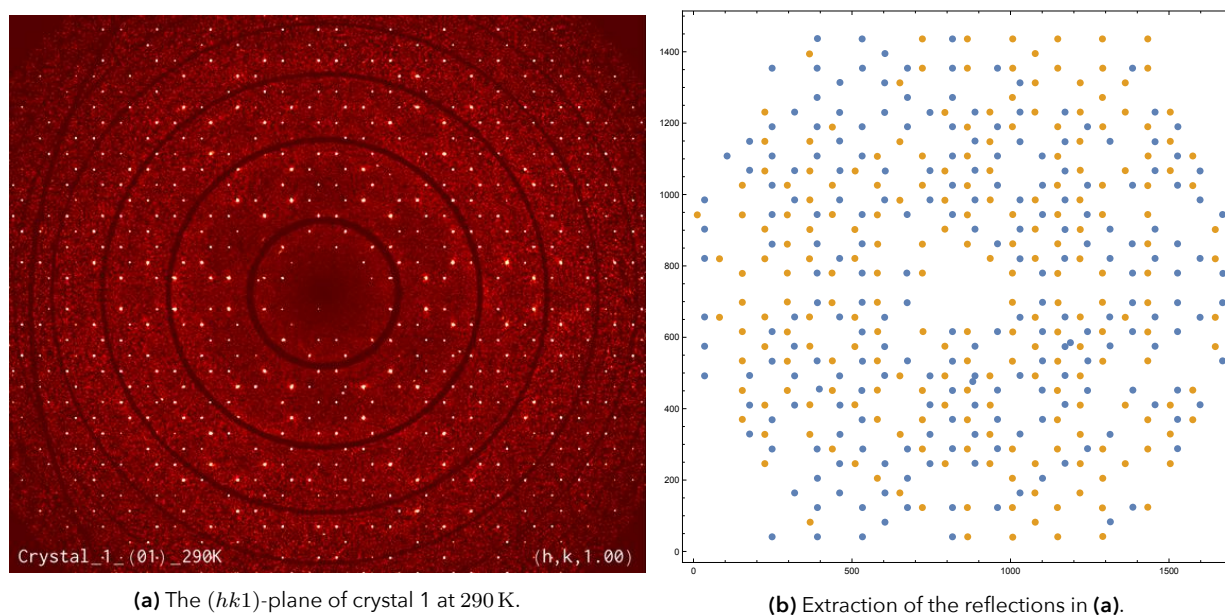


Figure 3.17: (a) Reconstruction of the $(hk1)$ plane in reciprocal space of crystal 1. (b) `ReflectionConditionCheck` applied at the same image. Yellow dots represent reflections fulfilling the condition in (3.10a), and the blue dots the rest of the lattice.

Figure 3.17b shows that only half of the reflections in the $(hk1)$ plane of data subset `Crystal_1_(01)_290K` fulfil the reflection condition of (3.10a); the other half adhere to (3.10b). Further inspection revealed that when $l \in \{0, 3, 6, \dots\}$, i.e. the pattern type *A* of (3.9a), both reflection conditions of (3.10) were fulfilled, and the reflections overlap. For pattern types *B* and *C* we get two domains of reflections as seen in Figure 3.17b.

This pattern we see where reflections alternate between overlapping and not, is called *reticular merohedry*, and is typical for rhombohedral crystals.^[93] The point group of the twin lattice is $6/mmm$, while $\bar{3}m1$ is the Laue group associated with the structure. By performing a coset decomposition we find that the two-fold rotation axis $2_{[001]}$ is

a suitable twin operator, giving to the twin law:

$$T = \begin{bmatrix} -1 & 0 & 0 \\ 0 & -1 & 0 \\ 0 & 0 & 1 \end{bmatrix} \quad (3.11)$$

According to Herbst-Irmer and Sheldrick^[94], there reflections from an obverse–reverse twin adhere to one of four types, as stated in Table 3.10.

Type	Condition	Observed in
I	$-h + k + l = 3n$ $h - k + l \neq 3n$	main domain
II	$-h + k + l \neq 3n$ $h - k + l = 3n$	second domain
III	$-h + k + l \neq 3n$ and $h - k + l \neq 3n$	none domain
IV	$-h + k + l = 3n$ and $h - k + l = 3n$	both domains

Table 3.10: The four obverse–reverse twin reflection types according to Herbst-Irmer and Sheldrick^[94].

These descriptions are in accordance with our findings with the `ReflectionConditionCheck` function.

Solving the structure

Although *CrysAlis* has the ability to operate with multiple lattices for twins, we were unable to assign distinct lattices for the obverse and reverse settings. Instead, the peaks that should be systematic absent in the reverse setting were hid in `Ewald explorer` so that the program would select a rhombohedral lattice instead of hexagonal. After data reduction the structure was solved correctly, but with refinement parameters converging to poor values such as $R = 15.76\%$ and $\text{Goof} = 2.341$. Since the structure solutions and refinements gave much better results for the other thiourea-ferrocene crystals (4 and 9), this topic was not pursued further for crystal 1.

3.4.3 Low temperature inspection

As temperature decreases from room temperature, the most evident changes occur at the transition from 155 K to 140 K. We observe a splitting of the nodes, which persists at least down to 90 K.

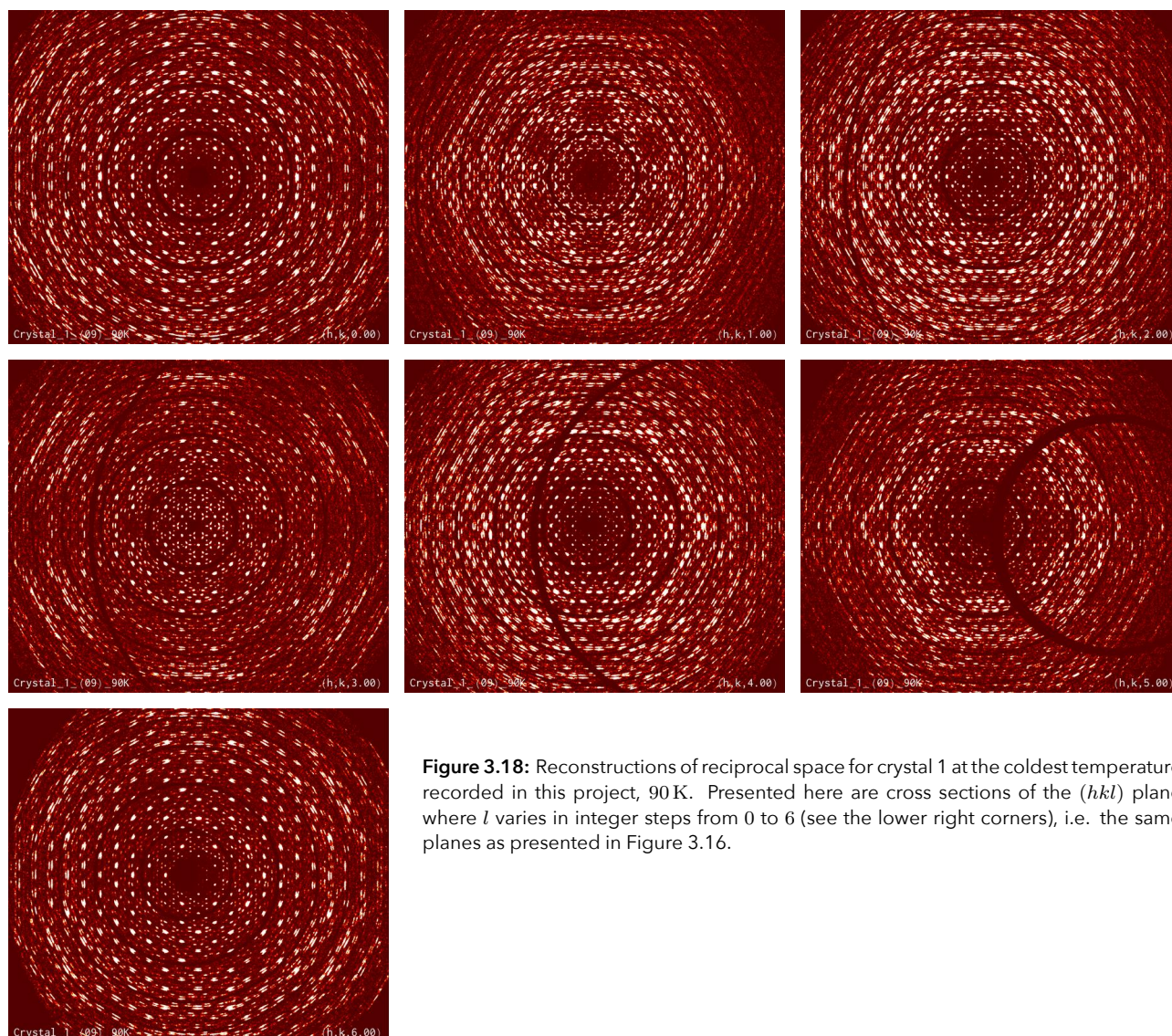


Figure 3.18: Reconstructions of reciprocal space for crystal 1 at the coldest temperature recorded in this project, 90 K. Presented here are cross sections of the (hkl) plane where l varies in integer steps from 0 to 6 (see the lower right corners), i.e. the same planes as presented in Figure 3.16.

For data subsets in this temperature region, the percentage of peaks matching the lattice fell from about 90 % to 65 % after reindexation with tolerance set to 0.05 with `Lattice wizard` \gg `Reindexation with current cell`. This is probably linked to the splitting of nodes, rendering a single lattice determination difficult.

The bright and split patterns we see in Figure 3.18 do not change significantly in size nor position in the range from 140 K to 90 K. The reflections seem to split into two or three streaks with the streaks being perpendicular to a line towards the origin, and growing in length further out in reciprocal space; see Figure 3.19. The rotational broadening is likely due to thiourea being a «soft host».

If we consider the transition from 200 K to 180 K carefully, we notice an emergence of weak satellites near the origin. Proceeding to 165 K shows an increase in both the number of satellites and the intensity of the existing ones.

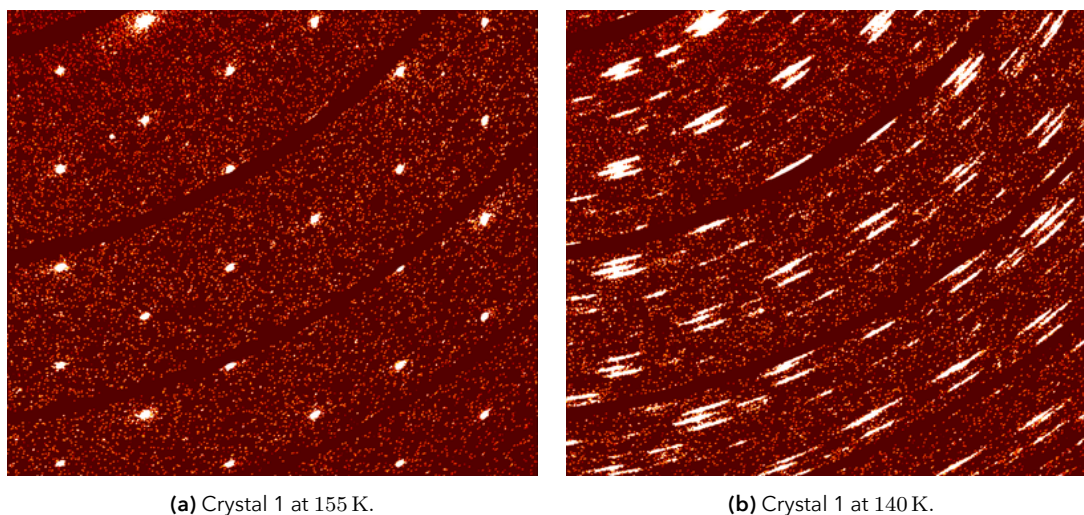


Figure 3.19: Reflections splitting somewhere in the temperature range 155 K to 140 K. Both images are centred at $(hkl) = (13.5, \overline{13.5}, 0)$ with resolution 3.0 Å. When reflections split, they tend to become the streak closest to the origin, or the middle one when splitting in three.

Distinction between 140 K and 100 K

Although the appearance of the diffraction patterns look overall the same in the temperature range 90 K to 140 K, a minor detail distinguishes the 140 K patterns from those at 100 K.

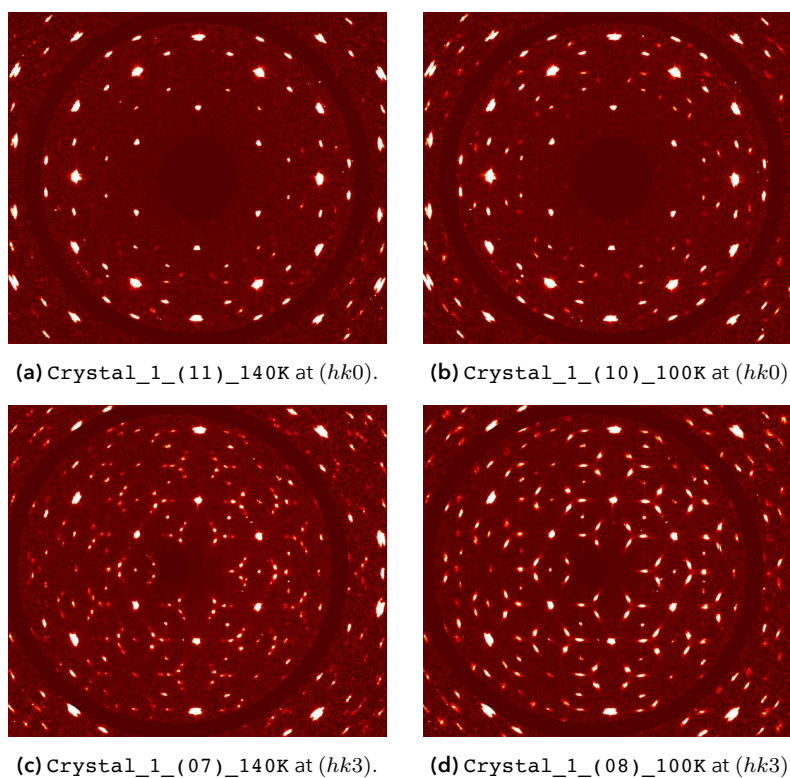


Figure 3.20: Two examples of transition from 140 K to 100 K, showing appearance of new satellites or intensifying of the intermediate structure. All images are reconstructed sections in reciprocal space at 3.0 Å.

If we look closely at the top images in Figure 3.20, we see that a secondary set of reflections appear at 100 K that either were not there at 140 K or were very weak. This is true for the whole diffraction pattern, also at other integer l 's, but most prominent near the origin. The bottom row of the same figure shows another example. The main feature we see at these transitions is an intensifying of intermediate reflections.

3.4.4 Finer sampling of reciprocal space

A new series of reconstructions were produced with a smaller step size in the l direction. Images were still in the (hk) -plane and with l going from 0 to 6 but now in increments of 0.05 units of c^* . The process is time-consuming as a single image takes about seven minutes to create, and the same procedure was done on all 17 data subsets. At this stage *CrysAlis* was installed on computers at the University's physics laboratory so that the reconstructions could be made in parallel[†].

Intermediate reflections at $l \pm 0.2$

After completion, we were able to see some interesting new features in the reciprocal space. Most notably were the intermediate peaks at ± 0.2 units away from integer l for about half of the data subsets. From a temperature developing point of view, we see an outline of ordering starting at 200 K, reaching maximum peaks at 165 K and remaining the same at 155 K, but vanish sometime before reaching 140 K. Figure 3.21 shows a cross section at 165 K. Accordingly, these intermediate peaks are present in 8 of the 17 data subsets. The process also seems to be fully reversible as identical patterns appear at the same temperatures when returning to room temperature.

The five-doubling of lattice parameters observed for some of the crystal 1 data (page 47) were in this temperature range, signalling a connected between these reflections and a modulation or increase of the unit cell.

Intermediate reflections at $l \pm 0.4$

A secondary type of intermediate peaks were observed at ± 0.4 units away from integer l at temperatures 180 K, 165 K and 155 K. Whereas the primary type of intermediate peaks at $l \pm 0.2$ were existent in the whole range $l \in \{0.2, 0.8, 1.2, \dots, 5.8\}$, these only appear at some values and vary with temperature. An overview is given in Table 3.11 below.

From the striking symmetry of Table 3.11 it is evident that the transitions of the crystal are reversible. The discrepancy between some of the same temperatures are likely due to difference in the exposure of the images, making the patterns more obscure in the darker variants (which here correspond to the second half of the data subsets). The most prominent reconstructions from the secondary type of intermediate reflections are shown in Figure 3.23.

Even finer sampling

Another series of reconstructions with the same parameters except for increments lowered to 0.01 units of c^* was also made. These images did not reveal any new features. They did, however, make it more apparent that random but sharp reflections always are present between the planes of integer indices.

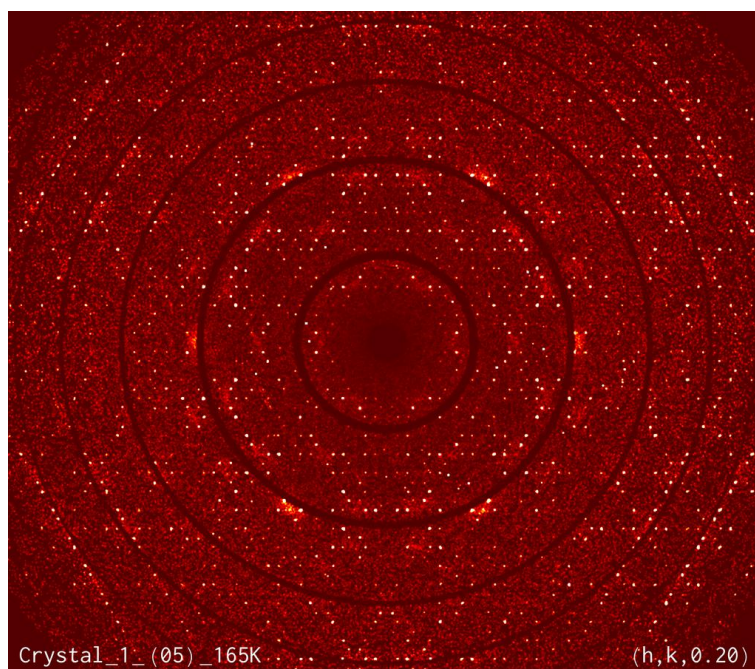


Figure 3.21: Intermediate reflections in the $(h, k, 0.20)$ -plane. The clear diffuse spots are the same as mentioned in Figure 3.16. The overall pattern of this cross section shows some resemblance to the $(hk3)$ -plane in Figure 3.16, while the $(h, k, 0.80)$ -plane (not shown) has a pattern more like the $(hk1)$ -plane in the same figure.

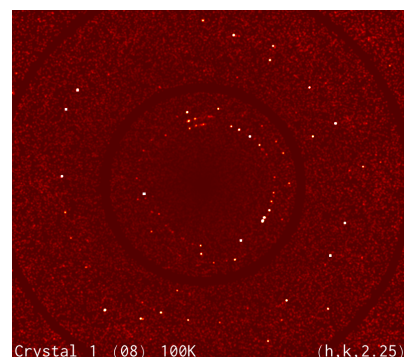


Figure 3.22: Tendency of ring formation.

[†] Constructing these images on a single computer would require at least 10 days for the complete data set of crystal 1.

	0.2	0.4	0.6	0.8	1.2	1.4	1.6	1.8	2.2	2.4	2.6	2.8	3.2	3.4	3.6	3.8	4.2	4.4	4.6	4.8	5.2	5.4	5.6	5.8	
290 K																									
240 K																									
200 K	◆			◆	◆			◆	◆			◆	◆			◆	◆			◆	◆			◆	◆
180 K	◆			◆	◆		◆◆	◆	◆			◆	◆		◆	◆			◆	◆			◆	◆	
165 K	◆	◆*	◆**	◆	◆		◆◆	◆	◆	◆		◆	◆		◆	◆	◆	◆	◆*		◆	◆		◆	◆
155 K	◆	◆*	◆**	◆	◆		◆◆	◆	◆	◆		◆	◆		◆	◆	◆	◆	◆*		◆	◆		◆	◆
140 K																									
100 K																									
90 K																									
100 K																									
140 K																									
155 K	◆	◆**	◆**	◆	◆			◆	◆	◆*		◆	◆		◆	◆	◆	◆	◆**		◆	◆		◆	◆
165 K	◆	◆**	◆**	◆	◆			◆	◆	◆*		◆	◆		◆	◆	◆	◆	◆**		◆	◆		◆	◆
180 K	◆			◆	◆			◆	◆			◆	◆		◆	◆			◆	◆			◆	◆	
200 K	◆			◆	◆			◆	◆			◆	◆		◆	◆			◆	◆			◆	◆	
240 K																									
290 K																									

Table 3.11: Overview of where the intermediate reflections are observed at the various temperatures, with the first temperature being the first data subset and l shown in the top row. Black diamonds designate the primary intermediate reflections, while the secondary are grey for clarity. The asterisks represent observations where the patterns are somewhat (or very) unclear.

Although these sharp reflections seem to emerge randomly around reciprocal space, they still tend to be fairly equidistant from the origin. In the temperature range 165 K to 90 K, starting at $l \approx 2.30$ faint rings start to appear close to the centre. Three concentric rings can be distinguished, gradually shrinking as we move along c^* , before vanishing at about $l \approx 3.60$. The rings do not form fully connected circles and are very weak, but the outline can still be seen. The same phenomenon was seen at $(1.2, k, l)$ for `Crystal_1_(06)_155K`.

3.4.5 The modulation patterns

The patterns we see at integer l repeat themselves every six units of l , as seen at ambient temperatures in Figure 3.16 and even more clearly when the reflections split, as seen in Figure 3.18.

Like the diffraction patterns at integer l , the patterns appearing at $l \pm 0.2$, $l \pm 0.4$, $l \pm 0.6$ and $l \pm 0.8$ have a period of six units of l , but emerge only at the specific temperatures listed in Table 3.11. In all cases, there is no significant change between the temperatures 165 K and 155 K. Since the diffractograms show no asymmetry before and after reaching the minimum temperature of 90 K, there are effectively just three unique images of each of the six patterns. These are shown in Figure 3.24.

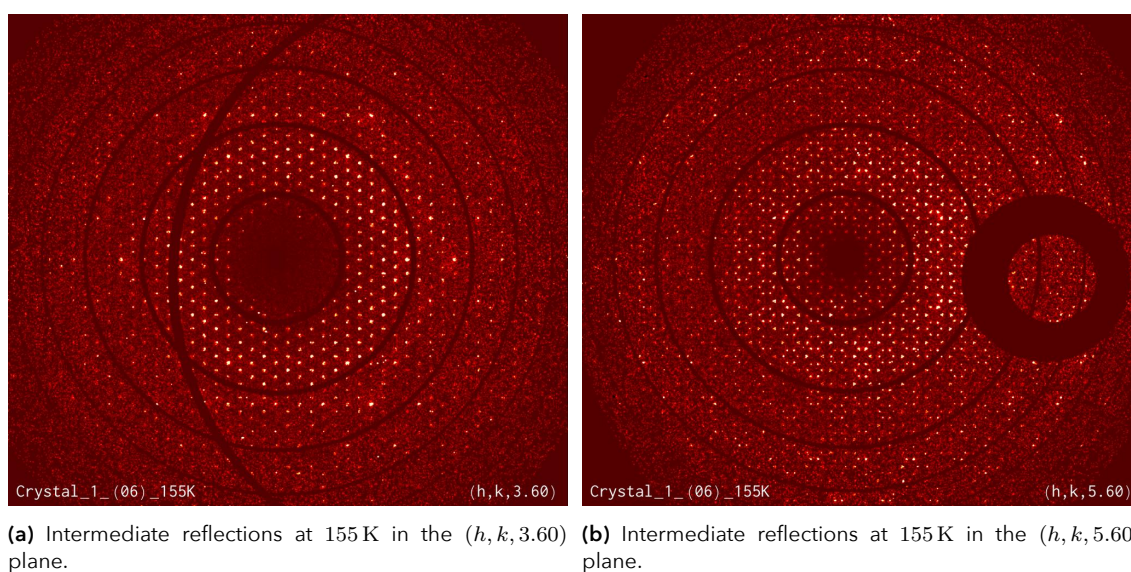
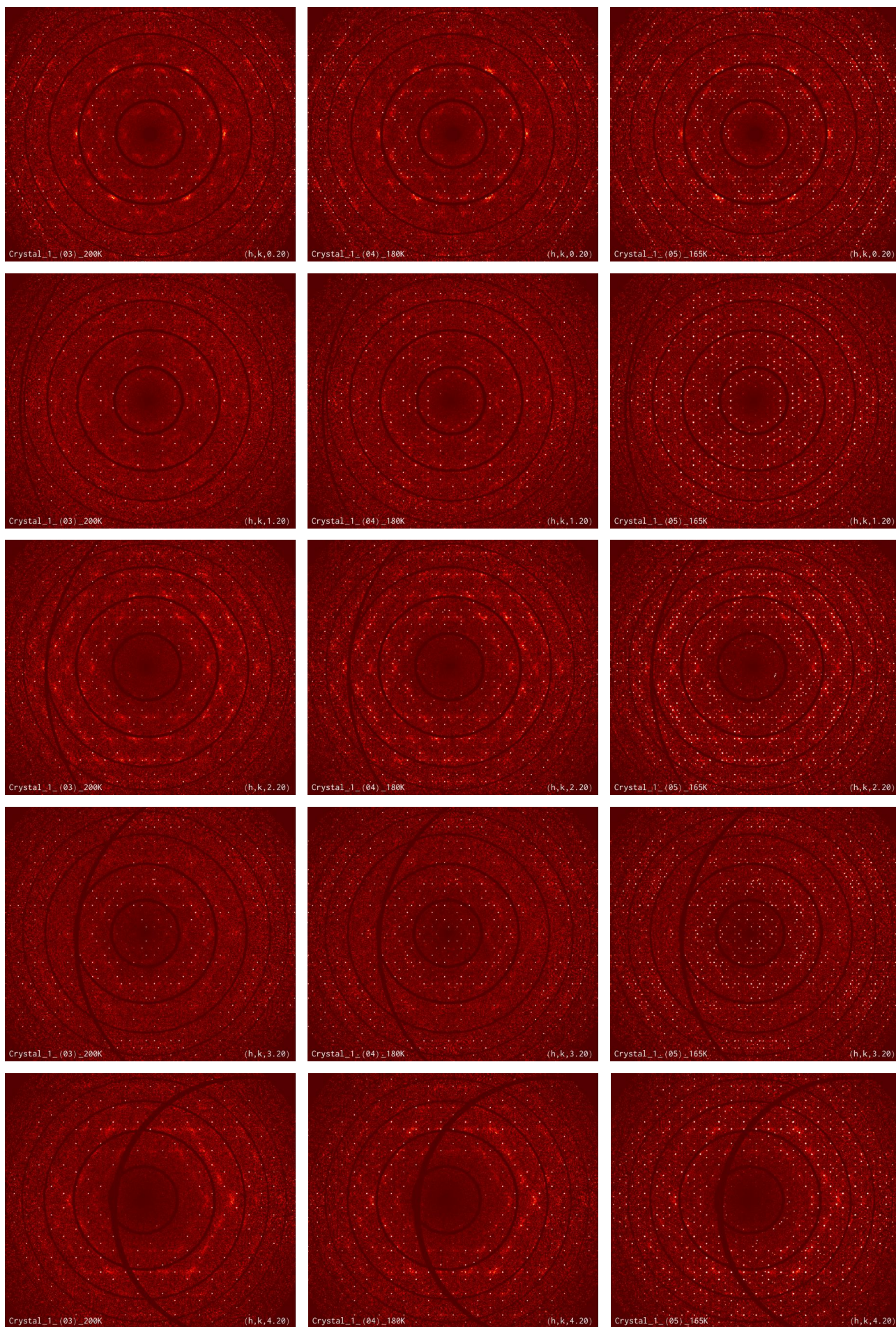


Figure 3.23: Intermediate reflections of the second type at the same temperature, but in two different planes. If we zoom in on the reflections in, we will see that many of them are clusters of two or three spots. In (b) we clearly see that the reflections are arranged in hexagons, and that these follow a hexagonal pattern themselves. The reflections in (a) fit in the middle of the smallest hexagons in (b).



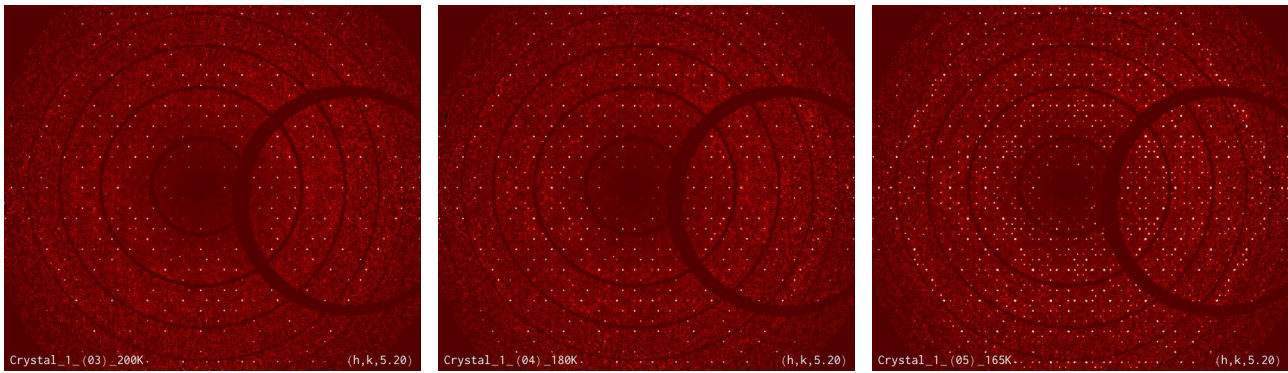


Figure 3.24: Reconstructions of reciprocal space for crystal 1 at the $l + 0.2$ -patterns for the three temperatures where these appear. Each row corresponds to a certain plane in reciprocal space, while each column a fixed temperature (see bottom corners).

We see the same pattern at each $l + 0.2$ -plane: As we decrease the temperature from ambient conditions, the intermediate reflections first appear at 200 K. They grow in numbers until reaching a maximum at around 165 K to 155 K, before abruptly disappearing at or before 140 K.

Complementary modulation patterns

The relation between the modulation patterns seems to be more complex than the $ABC ACB$ pattern for the integer l -planes in ref. Still, the planes come in “pairs” that complement each other in the sense that they do not overlap but belong to the same diffraction pattern. The pair of intermediate patterns at $l \pm 0.2$ are centrosymmetric about that given l . Some pairs have overlap of reflections; a brief overview is given in Table 3.12.

l_1	l_2	Note on overlapping
0.8	1.2	No overlap
1.8	2.2	No overlap
2.8	3.2	Somewhat overlap
3.8	4.2	No overlap
4.8	5.2	No overlap
5.8	0.2	Somewhat overlap

Table 3.12: Overview for the complementary layers (hkl_1) and (hkl_2) .

The six pairs of the mentioned planes have been combined to produce new images, shown in Figure 3.25. These images have some common features in their patterns, but it is difficult to say anything conclusive. They also seem to bear some resemblance to the planes in Figure 3.18 with split reflections.

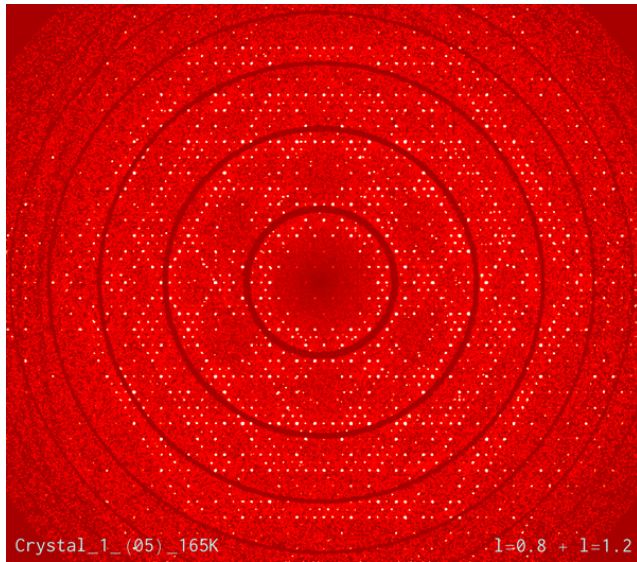
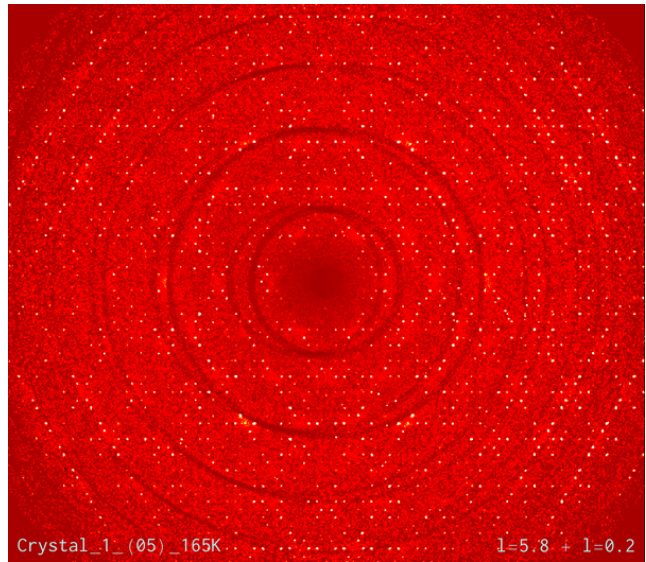
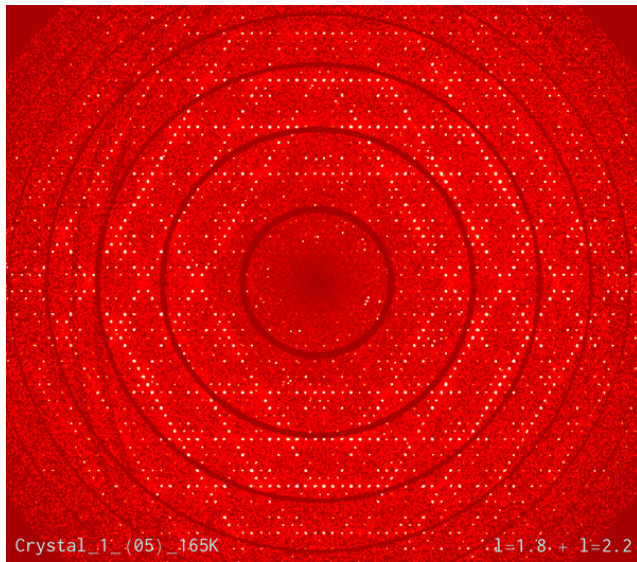
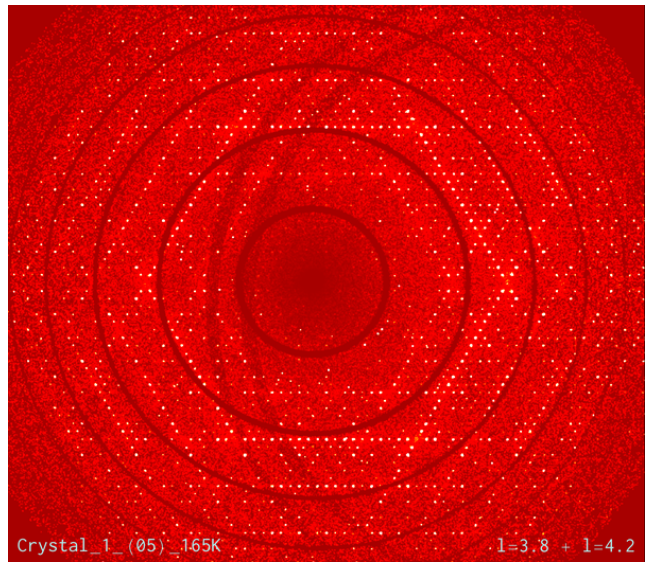
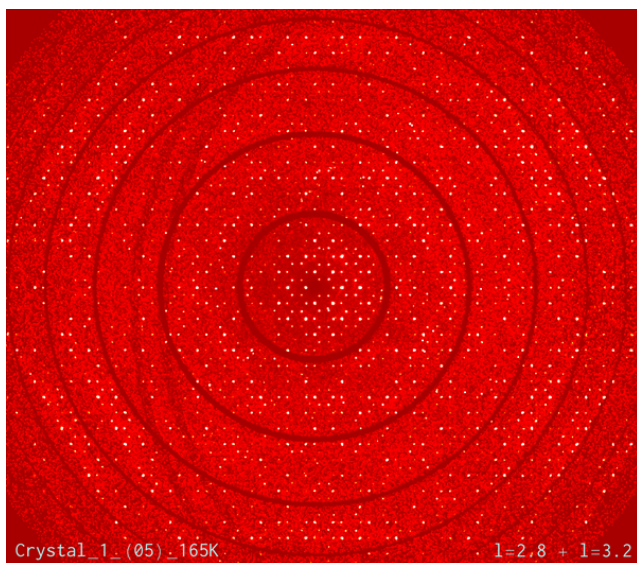
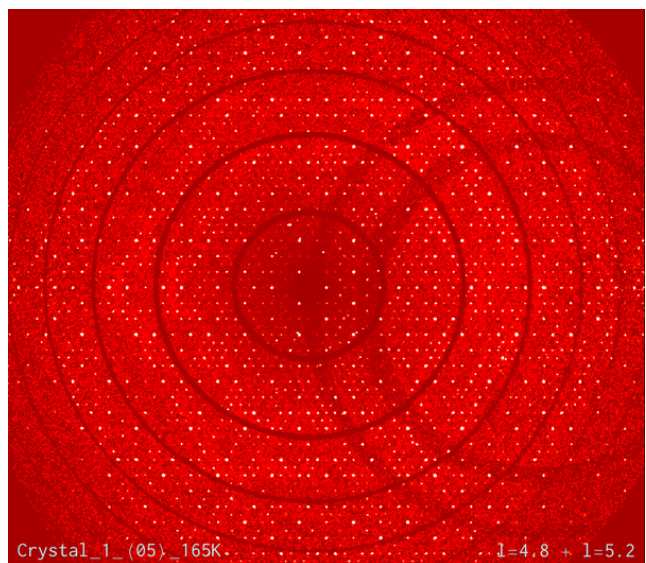
(a) $(h, k, 0.8)$ and $(h, k, 1.2)$.(b) $(h, k, 5.8)$ and $(h, k, 0.2)$.(c) $(h, k, 1.8)$ and $(h, k, 2.2)$.(d) $(h, k, 3.8)$ and $(h, k, 4.2)$.(e) $(h, k, 2.8)$ and $(h, k, 3.2)$.(f) $(h, k, 4.8)$ and $(h, k, 5.2)$.

Figure 3.25: Complementary $l \pm 0.2$ modulations. All reconstructions are from the `Crystal_5_(05)_165K` data subset.

3.5 Crystal 4

17 data subsets have been collected also for crystal 4, but they differ from crystal 1 in that we have two data subsets on 100 K (one replaces 90 K) and one extra «test run» at room temperature. Recall the specific measurement points from Table 3.5. The *CrysAlis* procedure is identical to that of crystal 1. The three main steps are:

1. Setting the diffractometer instrument parameters to values obtained from room temperature data (Table 3.7).
2. Finding peaks, determining the unit cell, reindexing, removing wrongly indexed peaks and refining the instrument model parameters.
3. Extracting refined instrument parameters and orientation matrices from log files.

For this crystal, the data was also processed without presetting the refined instrument parameters in order to check the necessity of the refinement procedure. The whole process from peak hunt to right before data reduction is the same.

Like before, once each data subset has been processed and refined they need to be “aligned” by transformation of the orientation matrix, as it affects the orientation of the reconstructions of reciprocal space. We did not experience the same trouble with transformations of the orientation matrix as with crystal 1; the required transformation matrices were obtained using the `UBtransformation` function (as explained on page 47) with Laue class $\bar{3}m$ (orientation $\bar{3}m1$).

Comments on the analysis without preset instrument parameters

It was discovered at this point that performing the peak hunt using the option «auto analyse unit cell» yielded much better results. Using the «automatic threshold and background detection» method found in `Lattice wizard` `Peak hunting wizard` (see Figure 2.13), *CrysAlis* tends to find a rhombohedral lattice that accounts for about 35 % of the found peaks, for the seven first data subsets. When going into the `Ewald explorer` and checking for twins, the program finds a twin, rotate 120° about the original lattice, that indexes about the same amount of peaks. After using the «auto analyse unit cell», however, the amount of matching peaks had risen to about 90 %. This method has since been used on all data sets.

The two methods – with and without preset instrument parameters – both had one instance each where *CrysAlis* did not succeed in setting a rhombohedral lattice automatically. With preset parameters the case was data subset 09 at 100 K, in which the lattice was initially suggested to be $2/m$, C -centred. The lattice was, rather surprisingly, set correctly after performing the «auto analyse unit cell» a second time. With no initial instrument settings, we had the same problem with data subset 10 at 140 K. In this case the refined parameters were used, giving the rhombohedral lattice after a second peak hunt.

In retrospect, the desired unit cells could most probably have been obtained with transformation matrices found in chapter 5.1 of the *International Tables for Crystallography, volume A*^[92]†.

† This was accomplished when the same problem arose during a reprocessing of data.

3.5.1 Investigation of the reciprocal space

We see right away that the reciprocal space of crystal 4 is quite different from that of crystal 1.

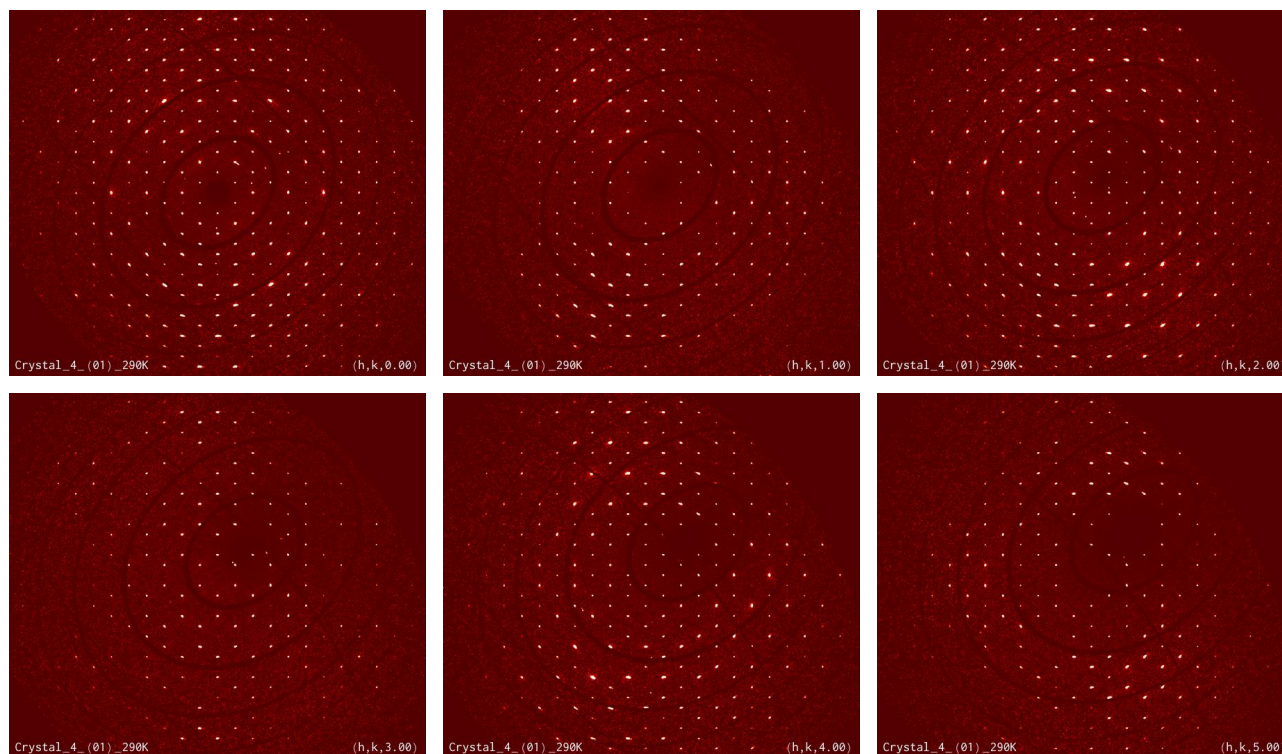


Figure 3.26: Reconstructions of the reciprocal space of crystal 4, using data subset `Crystal_4_(01)_290K`. The (hkl) planes with $l \in \{0, 1, 2, 3, 4, 5\}$ are shown here.

`ReflectionConditionCheck` was used to confirm that all reflections adhere to (3.10a), i.e. the obverse setting of the rhombohedral cell. The space group was for all data subsets determined to be $R\bar{3}c$ (#167), which is the same found by Hough and Nicholson^[84].

When we go through the reciprocal planes in steps of 0.05 units along c^* we notice that the nodes are not in reflection condition simultaneously. Reflections with maximum intensity rather seem to propagate along “lines” in the plane perpendicular to the c^* axis, very much like the lines seen in crystal 3 (see page 44). In this crystal, we notice two nearly parallel lines that propagate symmetrically towards the origin. We have the most amount of nodes in reflection condition when the lines meet, which can take place up to 0.05 units away from integer l . This may be due to an inaccurate orientation matrix.

Intermediate reflections

The only noticeable signs of modulation are observed in the $(h, k, 2.8)$ planes and c . When we check the $(h, k, 3.2)$ planes we may notice a very faint pattern similar to ref, but it is in more or less indistinguishable from the background. Similarly to crystal 1, this modulation is only visible in the temperature range from 200 K to 155 K.

Lower temperatures

The first significant changes to the diffraction pattern is observed in the transition from 155 K to 140 K. We see the same two traits as we did for crystal 1: nodes of the reciprocal lattice are split in two or three and satellite reflections appear.

For crystal 1 we perceived a faint build-up of satellite reflections in the temperature shifts between 200 K to 165 K, but the same cannot be said for crystal 4.

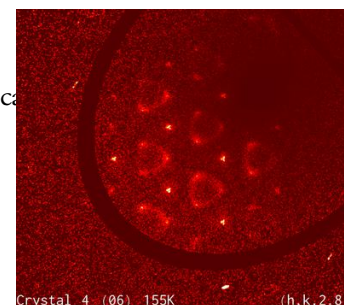


Figure 3.27: Diffuse pattern at 3.0 Å resolution in the $(h, k, 2.8)$ plane in crystal 4.

3.5.2 Solving the thiourea-ferrocene structure

In regards to the structure solution, only the data subsets processed with refined instrument parameters were used.

Thiourea structure only (at room temperature)

According to Hough and Nicholson^[84], the iron atoms have site symmetry 32, making them systematically absent for odd l . A reflection file (`.hkl`) generated for thiourea-ferrocene at room temperature has been truncated so that only entries with odd values of the Miller index l are present. This leaves us with the structure of thiourea only, as seen in Figure 3.28.

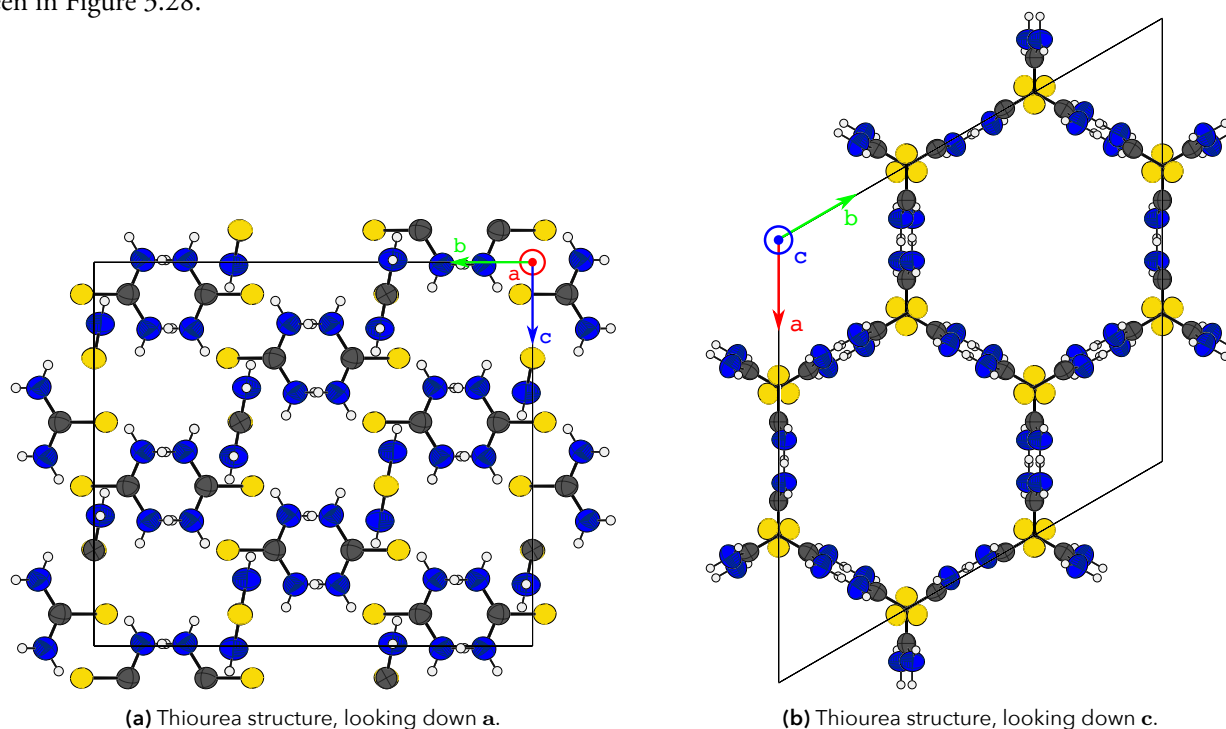


Figure 3.28: The thiourea-ferrocene structure with ferrocene suppressed.

Thiourea-ferrocene solution

All 17 data subsets were solved and refined to values presented in Table 3.13 below.

Data subset		01	02	03	04	05	06	07	08
Temperature		290 K	240 K	200 K	180 K	165 K	155 K	140 K	100 K
Completeness	[%]	92	94	93	94	93	93	94	94
R_{int}	[%]	6.07	6.00	6.25	6.25	7.75	6.43	8.67	13.03
I/σ		14.9	16.3	17.1	17.4	13.8	16.9	9.0	6.6
R	[%]	8.49	8.14	7.95	8.03	8.72	8.27	18.13	21.81
GooF		1.189	1.134	1.112	1.071	1.093	1.062	1.978	1.961
Data subset		16	15	14	13	12	11	10	09
Temperature		290 K	240 K	200 K	180 K	165 K	155 K	140 K	100 K
Completeness	[%]	93	93	93	94	93	92	93	93
R_{int}	[%]	7.56	6.80	7.38	6.78	9.09	11.45	17.97	10.63
I/σ		12.6	14.8	14.9	15.6	11.5	11.3	4.7	2.5
R	[%]	8.59	8.20	8.23	8.38	7.86	10.71	15.66	—
GooF		1.116	1.096	1.075	1.053	1.086	1.123	1.550	—

Table 3.13: Goodness parameters from the solving the structure of crystal 4 at all temperatures except the second data subset at 100 K.

The structure was in all cases solved with *SHELXT* and refined by least square methods by the same program.

Olex2 has trouble ascertaining the cyclopentadienyl rings of the ferrocene molecule when the temperature has decreased to 140 K. Firstly, the rings are not found to be five-fold, but six-fold, which must due to the non-crystallographic point group of the molecule. Secondly, the Q-peaks surrounding the iron atom almost form a spherical shell, as seen in Figure 3.29.

A selection of these Q-peaks must be carbon atoms of the cyclopentadienyl rings, but if care is not taken the carbon atoms will attain unreasonably large anisotropic displacement parameters. Both the *R*-factor and Goof would slightly increase as well.

When comparing the solved structures at the various temperatures we find that not much changes for temperatures above 140 K. Going below the temperature of $T_1 = 147.2$ K should transition the structure into the final phase VI according to Sorai et al.^[3]

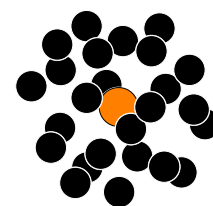


Figure 3.29: Q-peaks surrounding iron atom.

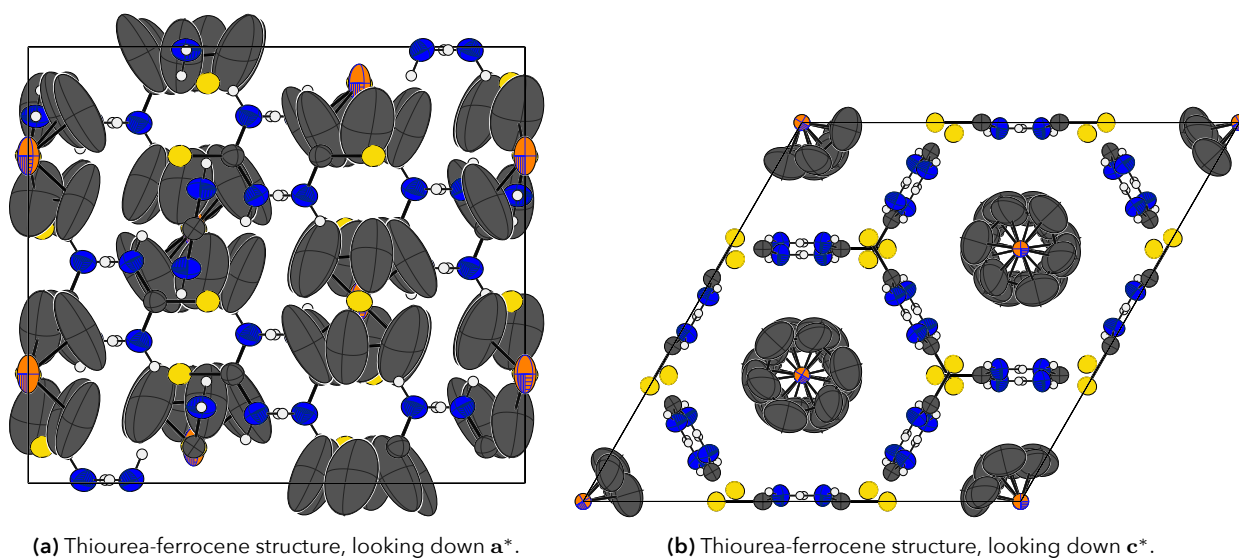


Figure 3.30: Thiourea-ferrocene (crystal 4) at 200 K.

When we reach 140 K we notice an important difference in the structure:

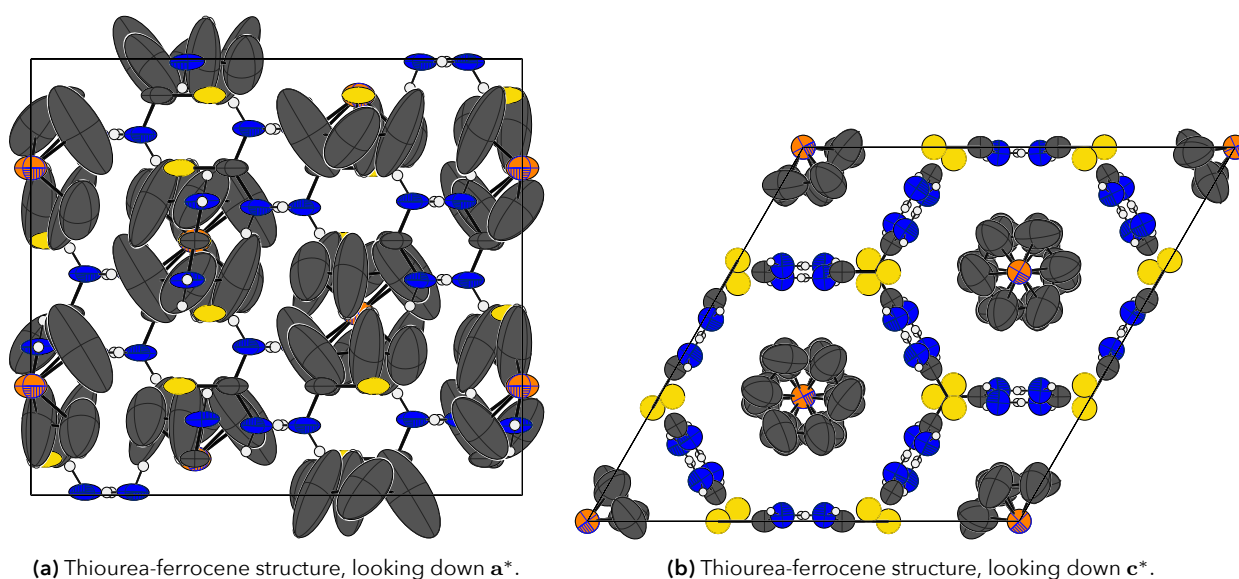


Figure 3.31: Thiourea-ferrocene; data subset `Crysta1_4_(07)_140K`.

The most noticeable change is in the anisotropic displacement parameters of the thiourea structure and iron atoms,

which appear to have been “squeezed” in the hexagonal base plane. The change we see could indicate that the ferrocene molecules have gone from what we (in subsection 2.4.2) called a «parallel orientation» to a «perpendicular orientation». Furthermore, this new alignment could alter the thiourea framework and thus be responsible for the split reflections we see at this temperature.

We note, however, that the structure of data subset `Crystal_(10)_140K` did not show a distinct elongation of the iron atom in the plane; its displacement parameters were rather isotropic. The thiourea framework still had the same appearance in both cases.

When it comes to the lowest temperature in our data set, 100 K, we succeeded in obtaining the familiar thiourea-ferrocene structure for one of the data subsets only, and with substandard refinement. Visually, the structure appeared similar to Figure 3.31a at 140 K, but with the anisotropic parameters flattened out even more in the plane.

3.6 Crystals 7 and 8

Crystal 7

Recall that the sample called «crystal 7» was the same thiourea-ferrocene crystal as «crystal 1». It stands out as the only data set going up in temperature. Five data subsets were collected at 290 K, 320 K, 350 K, 380 K and 410 K. The crystal was critically damaged at the highest temperature, as is evident from Figure 3.32.

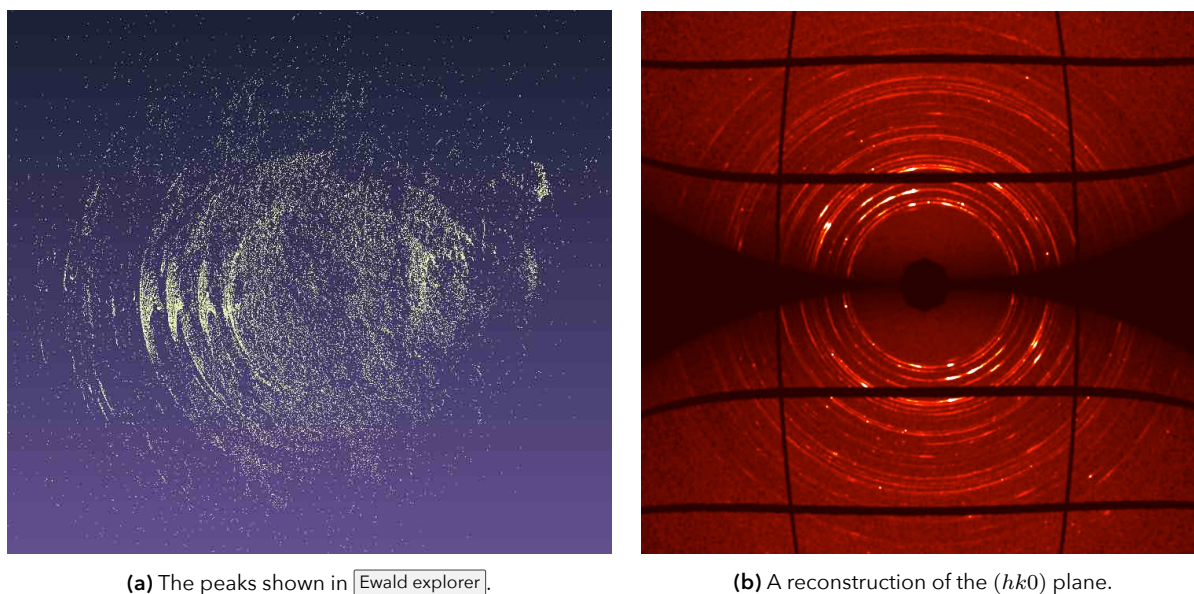


Figure 3.32: The condition of crystal 7 at 410 K.

A short list of the lattice parameters in Table 3.14 shows sign of expansion in the heating process.

Temperature	a	c
290 K	16.3812	12.4114
320 K	16.4086	12.4353
350 K	16.4376	12.4617
380 K	16.4686	12.4900

Table 3.14: The lattice parameters as determined by *CrysAlis*.

Crystal 8

This crystal was flawed and discarded after the test run.

It was still possible to solve the structure correctly and obtain the refinement parameters:

R_{int} :	5.02 %
I/σ :	18.4
R :	7.75 %
R_w :	24.34 %
GooF:	1.068.

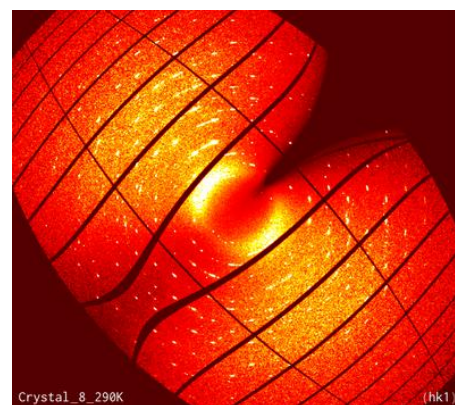


Figure 3.33: Reconstruction of crystal 8 in the $(hk0)$ plane.

3.7 Crystal 9

12 data subsets have been collected for crystal 9 in total, and the specific temperatures are found in Table 3.5. The data was once again processed without presetting the refined instrument parameters.

The two data subsets (07)_140K and (08)_100K were not determined to have rhombohedral lattices initially. Reiterating the peak hunt with refined instrument parameters was successful only for the former data set. A rhombohedral lattice was set for the 100 K data through `Ewald explorer`. By viewing the peaks the $(hk1)$ plane and hiding those systematically absent in the reverse setting, a rhombohedral unit cell was determined from the remaining peaks. This had to be refined in order to include the rest of the peak table.

3.7.1 Investigation of the reciprocal space

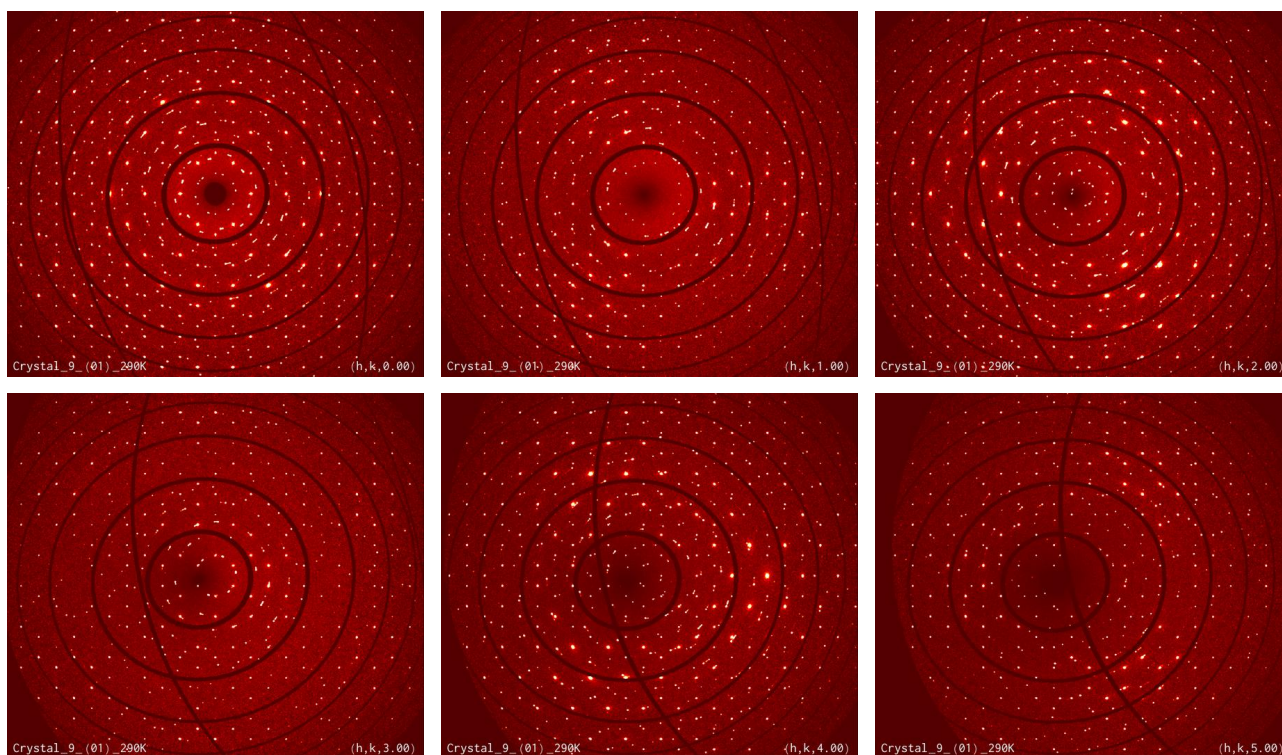


Figure 3.34: Reconstructions of the reciprocal space of crystal 9 at room temperature. Like Figure 3.16 and Figure 3.34, the first six (hkl) planes with integer l are shown.

Although we could not discern any significant difference between crystal 4 and 9 in the structure solution, the images of reciprocal planes are clearly different. Observe in Figure 3.34 the numerous satellite reflections amounting to small circles in the plane.

Another trait we see in this crystal is that it has a smoother background. This is probably related to the higher signal-to-noise ratio, which on average is 53.9 for crystal 9; over four times greater than crystal 4's average of 12.5.

The “lines of propagating reflections” mentioned in connection with crystal 3 and 4 are present also here. Unlike before, all nodes enter reflection condition simultaneously and precisely at integer l .

There is no difference between crystal 4 and 9 with regards to intermediate reflections at specific $l \pm 0.2$ layers.

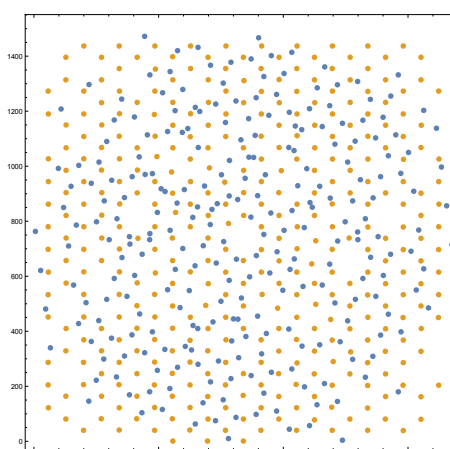


Figure 3.35: ReflectionConditionCheck applied to the $(hk0)$ plane to distinguish the main lattice from the satellites. The yellow dots represent reflections fulfilling (3.10a).

Inspection of lower temperatures

For this crystal we observe that the evident splitting of reciprocal nodes happens at 100 K, contrary to 140 K as seen in crystals 1 and 4. The transition from 155 K to 140 K shows splitting of the lattice to a very small degree, and even less for the satellite reflections; compare Figure 3.36a and Figure 3.36b.

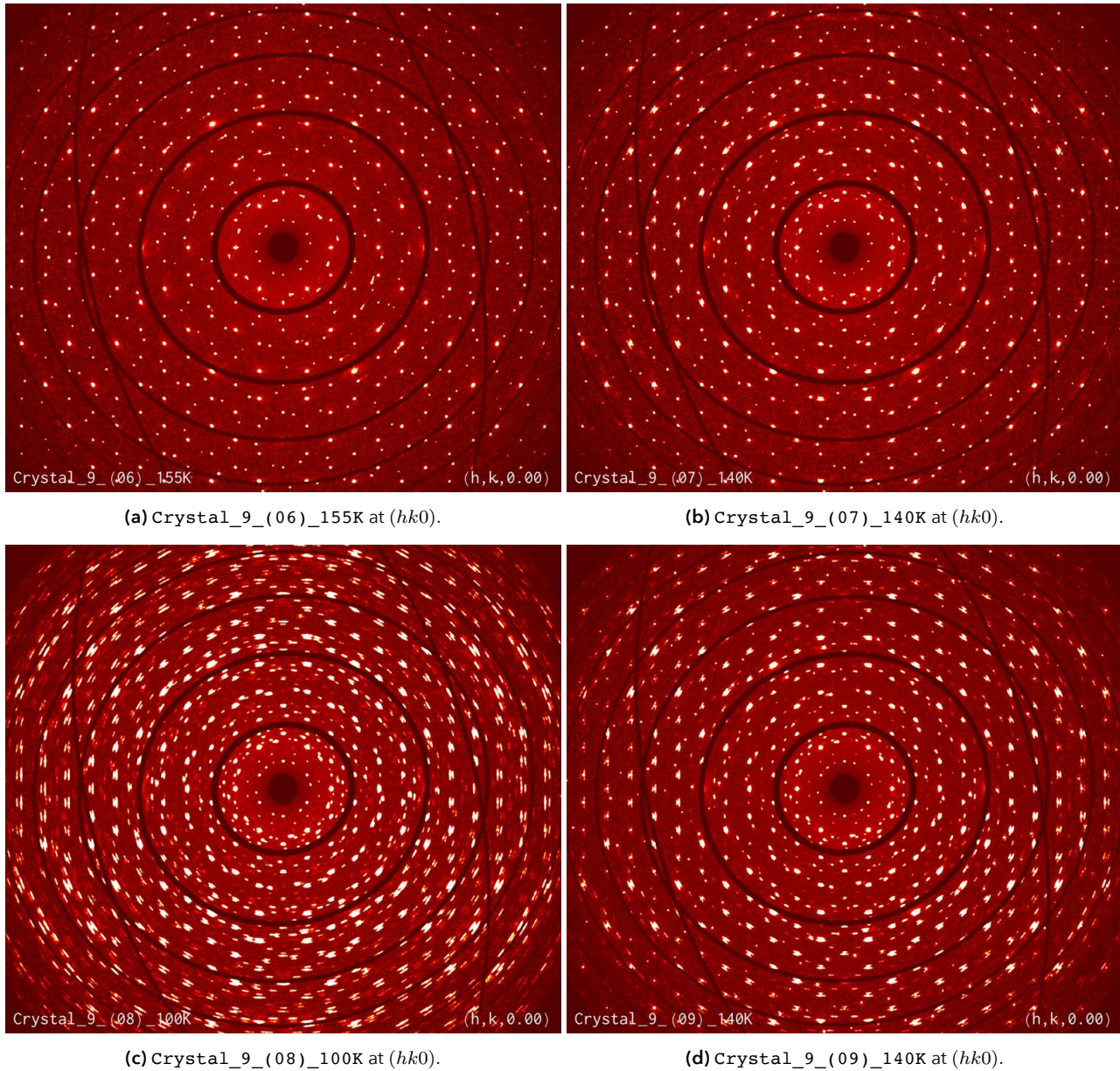


Figure 3.36: Reconstructions of the reciprocal plane $(hk0)$ for crystal 9 at the temperatures 155 K, 140 K and 100 K.

Comparing the first image at 140 K (Figure 3.36b) with the second image at this temperature (Figure 3.36d), we see that it appears to not have “recovered” from splitting of nodes at 100 K. The next data subset in this sequence, (10)_155K (not shown here), is indistinguishable from the corresponding image in Figure 3.36a.

3.7.2 Solving the thiourea-ferrocene structure

The structure has been solved and refined in the same manner as with crystal 4 in Table 3.13.

Data subset		01	02	03	04	05	06
Temperature		290 K	240 K	200 K	180 K	165 K	155 K
Completeness	[%]	85	86	85	85	86	86
R_{int}	[%]	2.85	5.95	2.66	2.15	2.05	2.06
I/σ		43.4	32.9	67.0	69.1	66.4	70.7
R	[%]	7.85	7.45	7.31	7.42	7.68	7.74
GooF		1.130	1.066	1.085	1.083	1.104	1.056
Data subset		07	08	09	10	11	test
Temperature		140 K	100 K	140 K	155 K	165 K	290 K
Completeness	[%]	86	85	87	86	85	85
R_{int}	[%]	2.03	9.60	6.14	2.08	1.91	3.07
I/σ		61.4	14.4	25.6	76.8	77.3	41.9
R	[%]	8.11	20.85	10.49	8.07	7.87	8.24
GooF		1.120	3.482	1.560	1.059	1.075	1.128

Table 3.15: Goodness parameters from the solving the structure of crystal 9.

The structure was solved at 100 K for this crystal, but very poor refinement resulted. We saw the same characteristic flattening of anisotropic parameters in the hexagonal base plane, just as described for crystal 4 (see page 63).

Comparing this with crystal 4, we see that the refinement indicators R and GooF are on the same order of magnitude. Crystal 4 has higher completeness, but crystal 9 excel with great signal-to-noise ratio and better internal consistency among symmetry equivalent reflections.

Chapter 4

Discussion

4.1 Challenges with *CrysAlis*

CrysAlis, like most crystallographic software, can be characterised as a so-called *black box* system, meaning the internal algorithms are hidden to us. Thus, we cannot fully explain the inconsistency among the reprocessed silicon data in subsection 3.1.2 nor the errors with frame scaling of crystal 3 (ferrocene) in Figure 3.8.

Other issues with the silicon data were also present. The newest version of *CrysAlis* at the time silicon data were processed was 171.37.35h, but data reduction on this version would never finish properly. The current version, 171.38.41, would also get stuck in the procedure (see Figure 4.1). When inspecting the data reduction results we found under «error model calculation» that no reflections were located in a certain `.tmp` file. This was checked on the two data subsets `Si_A_0_0_0` and `Si_A_0_0_90`. We had to switch to the older 171.35.21 version to run the data reduction successfully. The program could also fail in this version, in which case it would usually help to uncheck «Reduce background accumulation to SHORT type» in `Data reduction assistant` `> Step 4: Background evaluation`.

Refinalisation on newer versions were investigated. For the particular data set (`Si_D_0_100_90`) data reduction was first executed in 35.21 version. Refinalising within the same version produced the same `.hkl` files. The *CrysAlis* project was then loaded in the two newer versions mentioned above and refinalised once more. All reflections were in the same order, but intensities varied.

Performing the peak hunt in version 38.41 (automatic and traditional methods for `Si_B_0_0_0` and `Si_B_0_0_90`, respectively) led to a «runtime error» when trying to reduce the data in version 35.21 stating an «unsuccessful reading of image header». Initiating data reduction in version 38.41 (or 37.35h) instead did not prompt the error.

A final data process was done where as much variation as possible was eliminated; The data subset `Si_E_0_0_0` was arbitrarily selected for the task. Following the standard procedure (see ref), all the related project files in the data directory were copied to another location once data reduction was complete. The whole process was then redone. All details, including lattice parameters and orientation matrix, are identical up to data reduction. See Figure 4.2. After this step we find that the reflection files differ.

The challenges we have seen with *CrysAlis* thus far in this section seem to be related to specific crystal; silicon. The program is likely

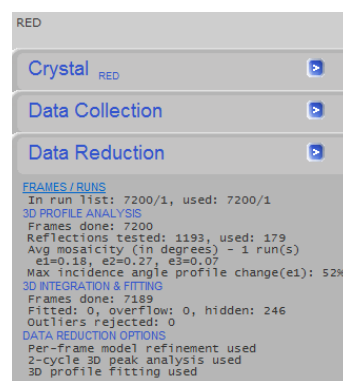
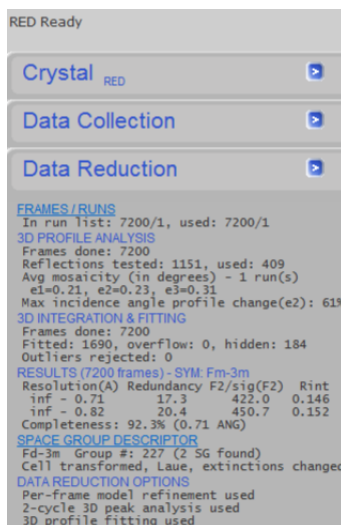
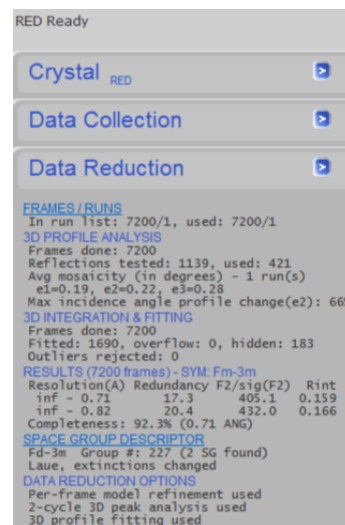


Figure 4.1: Data reduction stuck on frame 7189. Version: 171.38.41



(a) Results from first run.



(b) Results from second run.

Figure 4.2: Screenshots from *CrysAlis* showing differences despite all parameters being identical up to data reduction.

created with the aim of being versatile in order to cover as many fields of applications as possible, and not optimised for highly perfect crystals. For instance, we did not face any problems of this kind with the ferrocene or thiourea-ferrocene crystals (but data reductions on the same projects would still differ slightly). Even if we do not encounter any bugs in the software, finding the best parameters for the specific project can be a challenge in any case. Performing initial testing of different settings as a matter of usual practice is recommended.

A final note to keep in mind: After transforming the UB matrix (using the `um crec` command from the `UBtransformation` function), the instrument model refinement needs to be executed at least *twice* in order for the residue value to return to “normal”. Increasing the number of cycles in a single refinement will not help.

4.2 Thiourea-ferrocene

4.2.1 The temperature’s impact on relevant parameters

In our investigation of the crystal structure – via the images of reciprocal space – we use the hexagonal thiourea-lattice as a reference system or a “background” to contrast any temperature related changes we might observe. An underlying assumption is that the thiourea framework is not altered significantly in the cooling process.

The next four pages contain two sets of three plots each; one for the lattice parameters a , c and γ , and the another of the three rotations angles $r1$, $r2$ and $r3$. Each page is for a particular crystal, with an additional page for the alternative processing of crystal 4.

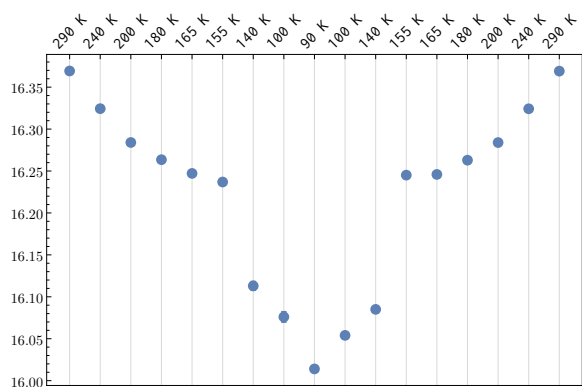
Starting with crystal 1, we first notice an abrupt change in the lattice parameters a , c and γ as the temperature decreases to 140 K or lower; a is lowered while c and γ increase. Another feature in the plots is a clear tendency for the a and c parameters to decline with lower temperature, which is also very symmetric about the turning point at 90 K. The same pattern is evident in the rotation angles, too.

Moving on to the first processing of crystal 4 – which followed the same standard procedure as the previous crystal – the same traits observed for crystal 1 also apply for a , c and γ . The development of the rotation angles as function of temperature follow a less clear pattern here. All plots, except for γ , in the case where no instrument parameters were preset are very chaotic, even though some resemblance with the previous descriptions can be seen. The lattice parameter a does not show the same abruptness as commented for crystal 1.

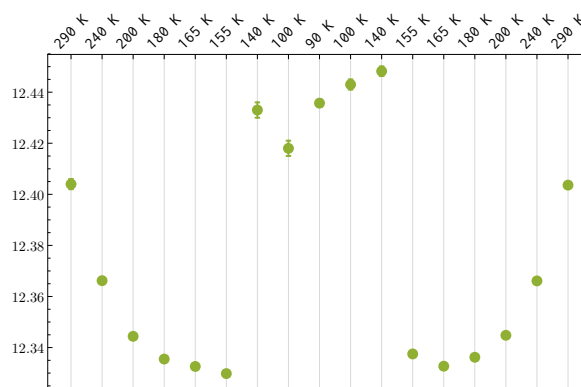
Finally, in crystal 9 we see the same decline of the a and c parameters with colder temperature, but a does not follow an obvious pattern around the coldest temperatures.

The uncertainties provided by *CrysAlis* seem suspiciously small; nonetheless, all data has been subjected to the same calculation procedures by the software.

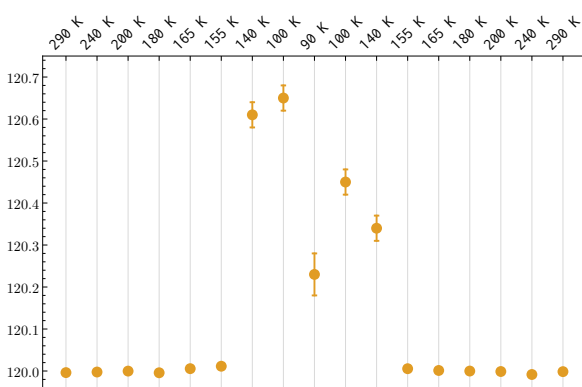
The temperature's impact on crystal 1



(a) Lattice parameter a .

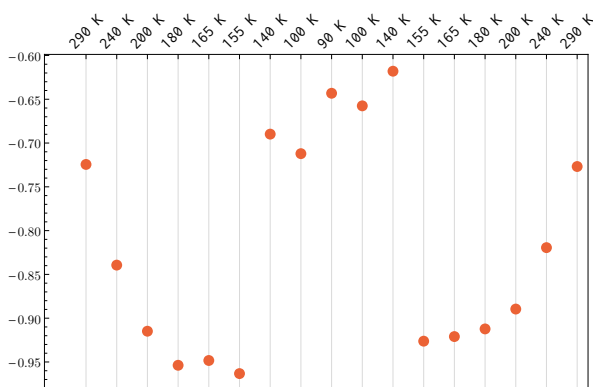


(b) Lattice parameter c .

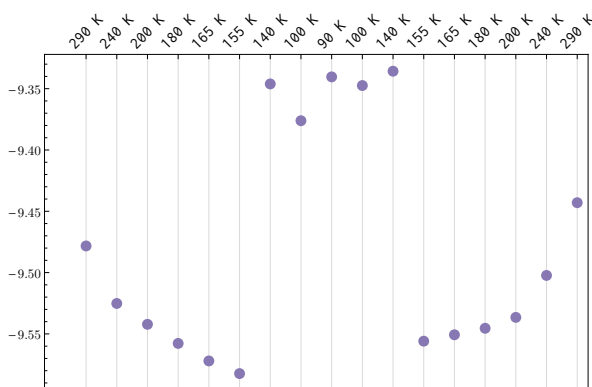


(c) Interaxial angle γ .

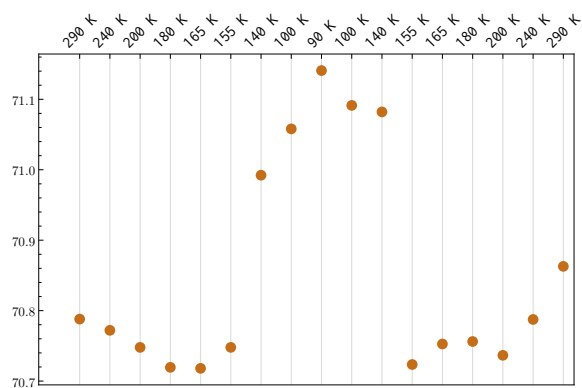
Figure 4.3: (a) and (b): Lattice parameters a and c of crystal 1 at various temperatures with ångströms on the vertical axes. (c): The cell parameter γ as calculated for an unconstrained cell (in degrees).



(a) Rotation angle $r1$.



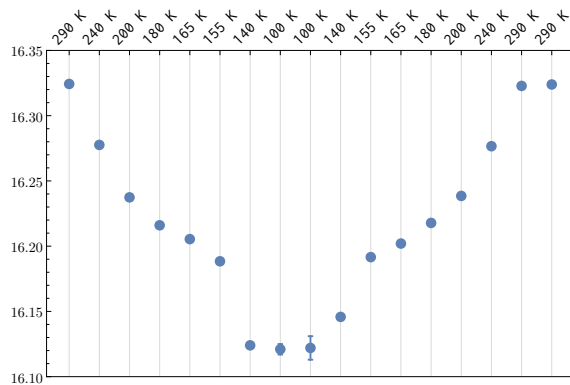
(b) Rotation angle $r2$.



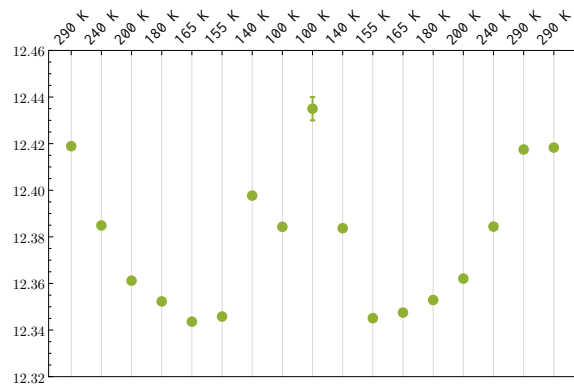
(c) Rotation angle $r3$.

Figure 4.4: Rotation angles $r1$, $r2$ and $r3$ of crystal 1 after transformations. Values on vertical axes are in degrees.

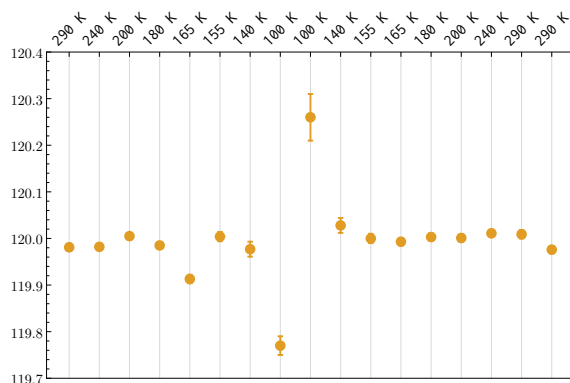
The temperature's impact on crystal 4 (presetting instrument model with refined values)



(a) Lattice parameter a .

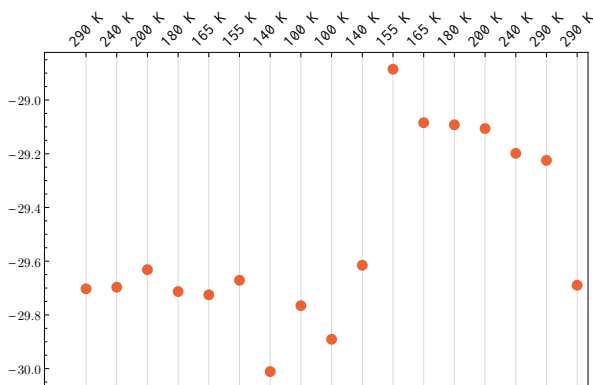


(b) Lattice parameter c .

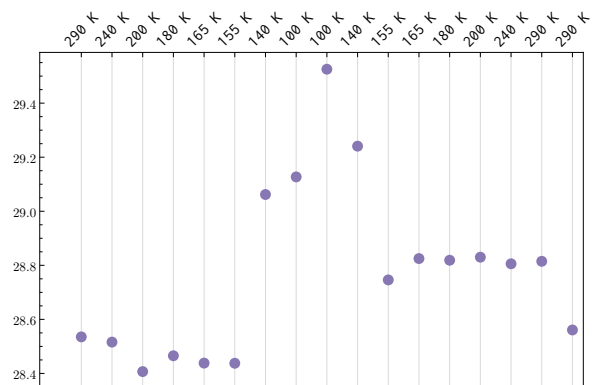


(c) Interaxial angle γ .

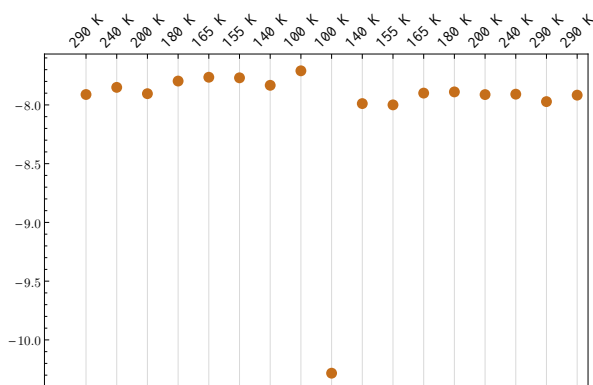
Figure 4.5: (a) and (b): Lattice parameters a and c of crystal 4 at various temperatures with ångströms on the vertical axes. (c): The cell parameter γ as calculated for an unconstrained cell (in degrees).



(a) Rotation angle $r1$.



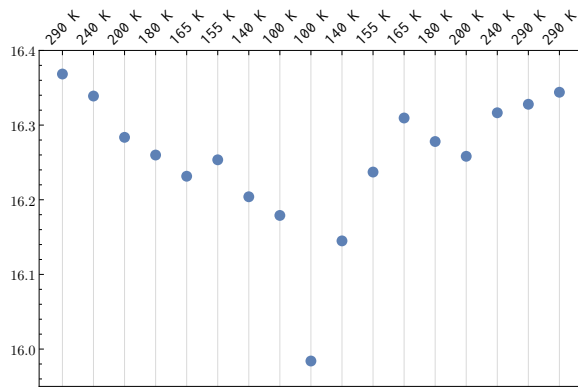
(b) Rotation angle $r2$.



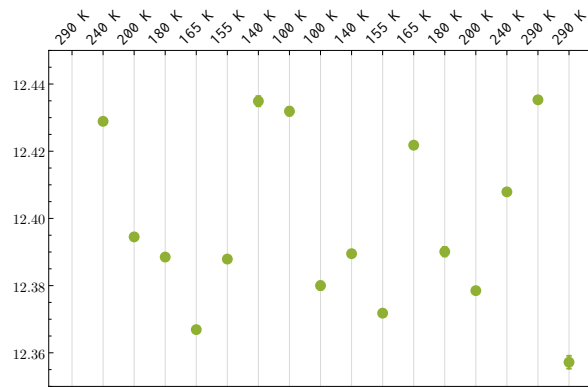
(c) Rotation angle $r3$.

Figure 4.6: Rotation angles $r1$, $r2$ and $r3$ of crystal 4 after transformations. Values on vertical axes are in degrees.

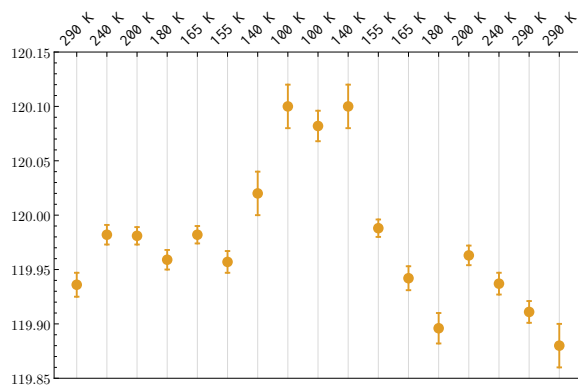
The temperature's impact on crystal 4 (no presetting of the instrument model parameters)



(a) Lattice parameter a .

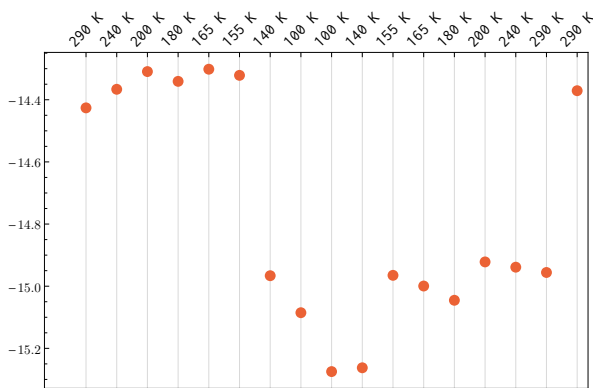


(b) Lattice parameter c .

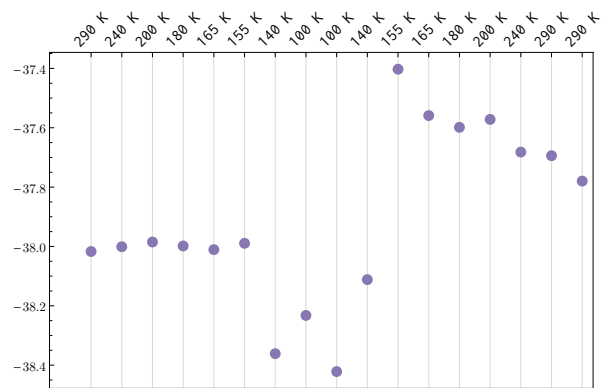


(c) Interaxial angle γ .

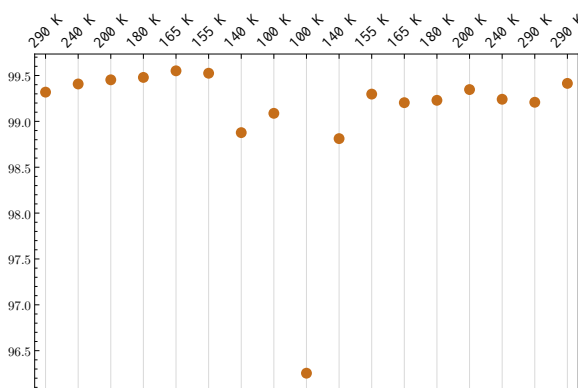
Figure 4.7: (a) and (b): Lattice parameters a and c of crystal 4 at various temperatures with ångströms on the vertical axes. (c): The cell parameter γ as calculated for an unconstrained cell (in degrees).



(a) Rotation angle $r1$.



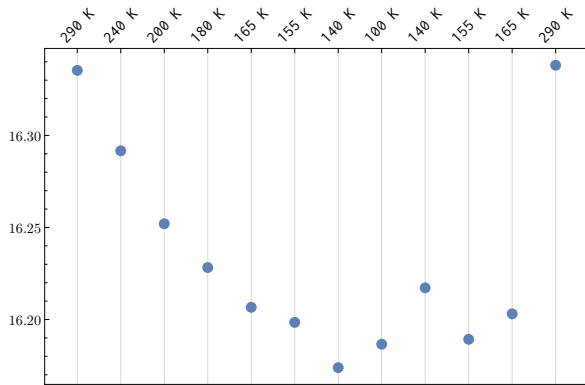
(b) Rotation angle $r2$.



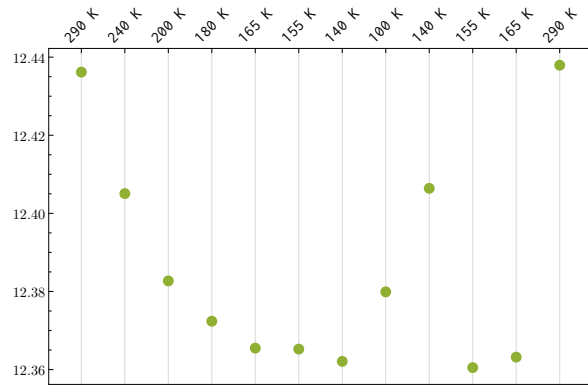
(c) Rotation angle $r3$.

Figure 4.8: Rotation angles $r1$, $r2$ and $r3$ of crystal 4 after transformations. Values on vertical axes are in degrees.

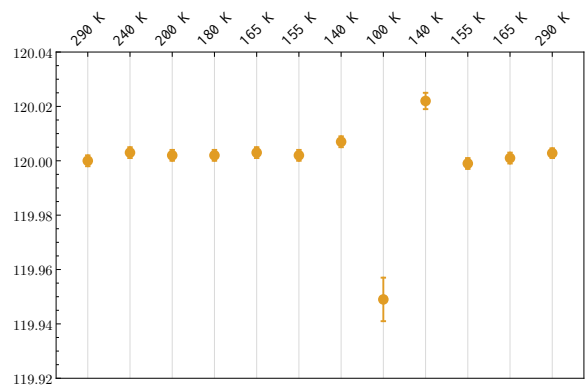
The temperature's impact on crystal 9



(a) Lattice parameter a .

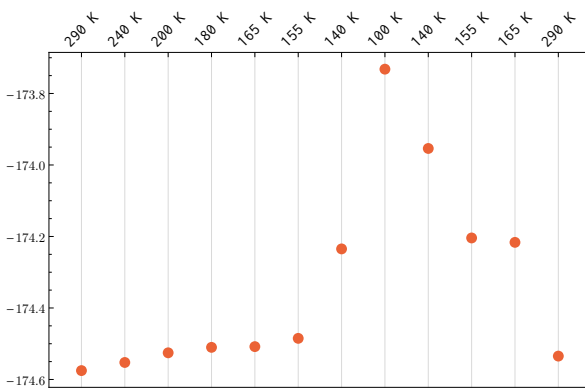


(b) Lattice parameter c .

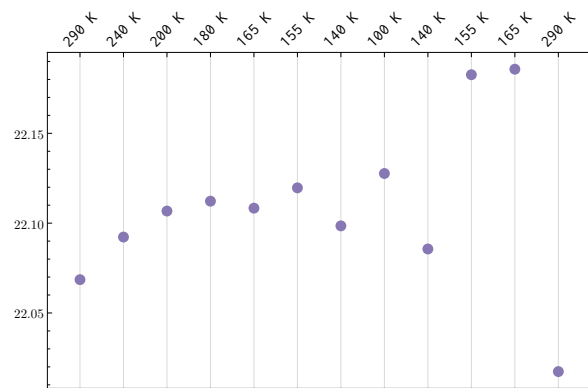


(c) Interaxial angle γ .

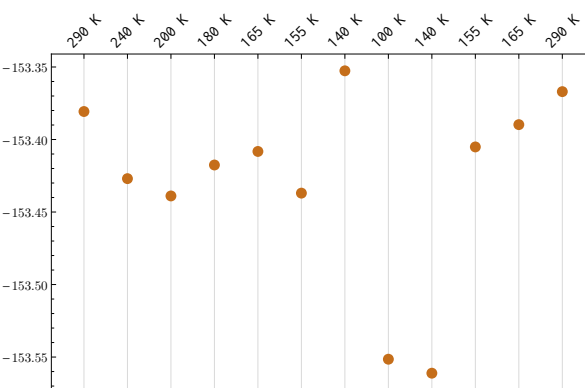
Figure 4.9: (a) and (b): Lattice parameters a and c of crystal 9 at various temperatures with ångströms on the vertical axes. (c): The cell parameter γ as calculated for an unconstrained cell (in degrees).



(a) Rotation angle $r1$.



(b) Rotation angle $r2$.



(c) Rotation angle $r3$.

Figure 4.10: Rotation angles $r1$, $r2$ and $r3$ of crystal 9 after transformations. Values on vertical axes are in degrees.

Mosaicity parameters

The peaks are assumed to follow a Gaussian distribution; the mosaicity is defined as the standard deviation of this curve. Figure 4.11 show plots of mosaicities extracted from data (after data reduction). The degree of mosaicity is given for three different scanning directions.

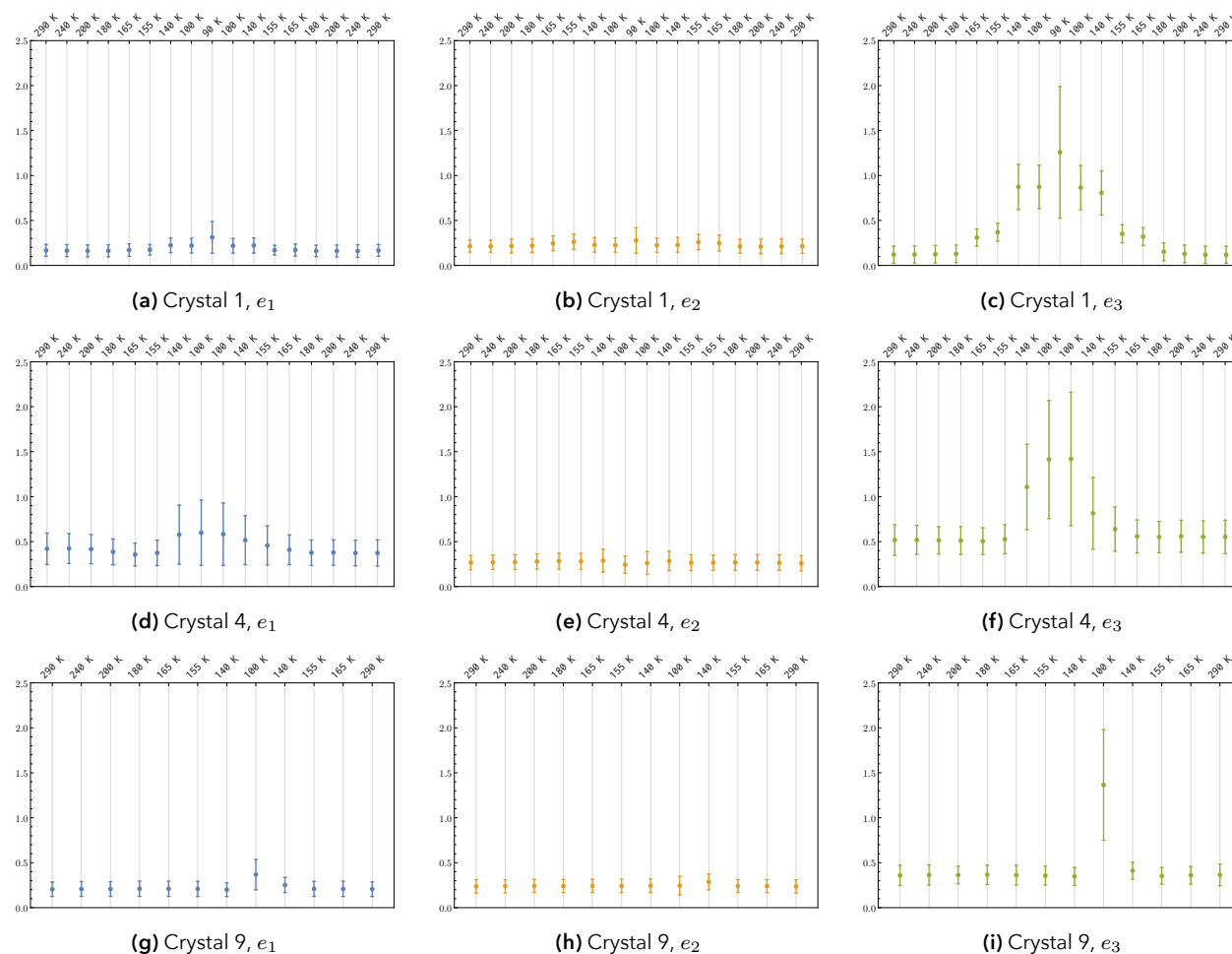


Figure 4.11: Mosaicity parameters of crystals 1, 4 and 9. e_1 and e_2 are directions in the detector plane, while e_3 is in the scanning direction.^[47] Note that all vertical axes show the same range; 0.0° to 2.5° .

It is clear that the colder temperatures affect the mosaicity in the e_3 direction most.

When looking over the structure solved in *Olex2* for the data points in Figure 4.11f and Figure 4.11i with mosaicity over 1.0° , we find that they correspond to the cases where the iron atoms had anisotropic displacement parameters visible flattened in the hexagonal plane (normal to the tunnel axis).

Also note that the 100 K data point with the large mosaicity in Figure 4.11i correspond to when the prominent splitting of reflections occurs, as seen in Figure 3.36d. This provides a link between the three observations: (i) splitting of reflections, (ii) large mosaicity and (iii) the shift of the iron atom's anisotropic displacement parameters.

Chapter 5

Conclusion

Structure factors and silicon data

The `StructureFactorTable`, which is a continuation of *Mathematica* code written by Thorkildsen and Larsen, has shown to produce values in good agreement with the literature. Structure factors generated with the *Mathematica* function were compared with results from experimental silicon data. We saw a decline in the intensity of the normally strong reflections, which we interpreted as a consequence of dynamical effects.

Room temperature analysis and refinement

An improvement of the instrument model residual factor could be traced back to a thorough inspection of the peak table, while its effect on the analysis and refinement of thiourea-ferrocene data remains inconclusive.

The «auto analyse unit cell» peak hunting method seems to find more peaks than the regular automatic method, and has since its discovery, been the preferred choice.

Temperature-induced phase transitions

Descriptions of the development of reciprocal for the thiourea-ferrocene crystals:

Transition	Description
290 K to 240 K	(no special remarks)
240 K to 200 K	(no special remarks)
200 K to 180 K	Emergence of weak satellites and intermediate reflections (crystal 1);
180 K to 165 K	Satellites increase in numbers and intensity (crystal 1)
165 K to 155 K	(no special remarks)
155 K to 140 K	The most significant change – splitting of reflections (crystals 1 and 4); Disappearance of intermediate reflections (crystal 1)
140 K to 100 K	Satellites increase in numbers and intensity (crystal 1); splitting of nodes (crystal 9)
100 K to 90 K	(no special remarks)

Table 5.1: Characteristic observations of the reciprocal space at studied temperature transitions.

The observation of splitting of reflections was linked to both a relatively large mosaicity (over 1.0°) and a shift of the iron atom's anisotropic displacement parameters to be most prominent in the plane perpendicular to the tunnel axis.

Twinning

The thiourea-ferrocene sample referred to as «crystal 1» is concluded to be twinned by so-called «reticular merohedry». Remarkable diffraction patterns emerge in the temperature range from 155 K to 200 K at specific fractions of l

5.1 Future work

Further studies of thiourea-ferrocene

Although the structures of ferrocene and thiourea-ferrocene have been solved with resulting lattice parameters in accordance with the crystallographic literature, a complete understanding of the observations has not been achieved. Further work on this project should be focused on simulating modulations of the structure, followed by comparison with observations, in order to uncover more details of the structure. As a first step, reconstructions of reciprocal space can be simulated; Figure 5.1 shows an example.

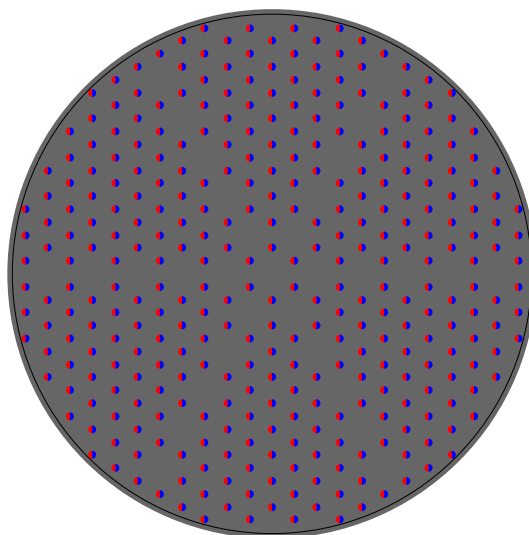


Figure 5.1: A simulation of the $(hk3)$ plane in a thiourea-ferrocene crystal. Developed by Thorkildsen.

Mathematica package

The *Mathematica* package has mainly served as a computational tool, and has the advantage of being independent of «black box» systems such as *CrysAlis*. The package has great expansion potential for our line of work; it has been an indispensable tool for handling the huge amount of data and for solving the specific problems encountered. Although the project has not come to a closure, far less would have been achieved without this package.

Chapter 6

Appendices

6.1 Appendix A – *Mathematica* documentation

Included here is a static version of the *Mathematica* documentation for the **Xray** application. The *Mathematica* package is “installed” by simply placing the package folder **Xray** in \ominus (**\$UserBaseDirectory**) \blacktriangleright **Applications** and is loaded with the command:

```
<< Xray`
```

Alternatively, the user may set the *Mathematica* to load the package automatically on start-up by writing the command above in \ominus (**\$UserBaseDirectory**) \blacktriangleright **Kernel** \blacktriangleright **init.m**.

X-Ray Diffraction Package

Helge Bøvik Larsen · Stian Penev Ramsnes · Gunnar Thorkildsen — University of Stavanger · 2016

▼ CrysAlis

Unwarping

UBtransformation — Derives the *CrysAlis* code needed to transform UB matrices.

UnwarpLayerList — Produces a list of unwarping commands that can be imported into *CrysAlis*.

ImgJpgScript — Generates a script file that converts the `.img` format to `.bmp` or `.jpg` when loaded in *CrysAlis*.

Post-analysis

MergeLogs — Merges multiple log files from the same project.

RefinedValues — Extracts the refined model values from log files.

IntensityTable — Produces a table over intensities and more from `.hkl` files.

ReflectionConditionCheck — Shows which nodes fulfil given reflection conditions in an image of the reciprocal space.

GeneratePixelData · **FindPixelClusters** · **\$PixelData**

Other tools

PeakTableHelper — Given the peak table, this function produces a list of which duplicates to delete.

MonitorIni — Auxiliary tool for the `xxmonitorinifromrunlist` command.

UBfix · **ReflectionSetInspection**

▼ Structure factor calculations

StructureFactorTable — Generates a table of structure factors, phases, Bragg angles and more.

Reflections

ReflectionCheck — Checks if a given reflection is extinct.

SymmetryReduction — Delete duplicates by symmetry equivalence.

FindLaueClassRep — A representative reflection among symmetry equivalent reflections.

ReflectionList — Generates a suitable list of reflections.

ToMiller · **FromMiller** · **\$LaueClasses**

Crystal data

\$Crystals · **ReadCrystalData**

▼ Miscellaneous tools

\$XrayExamples — A special directory containing files for demonstration purposes.

String manipulation

ChangeExtension — Changes the file extension of a given file.

UpdateString — Replaces string expressions inside files with new ones.

ConvertToDat · **UpdateFullForm**

Images

GifGenerator — Produces a `.gif` or `.mp4` animation of the input.

MarkImages — Puts tags in lower left and right corners of images.

Usage messages

ExtractUsage — Extracts usage message from notebooks.

NeatUsage — Tool for writing formatted usage messages.

StructureFactorTable

StructureFactorTable [λ , *crystal*, *class*]

produces a table of structure factors, phases, Bragg angles, Pendellösung distances and Darwin widths for a given wavelength λ , *crystal* and Laue *class*.

StructureFactorTable [λ , *crystal*, *class*, *condition*]

produces the same table, but reflections that do not follow the pattern of *condition* will be disregarded.

Details

- The Pendellösung distance is calculated from equation (4.26) [Authier, 2001]:

$$\Lambda_0 = \frac{\pi V \sqrt{\gamma_o |\gamma_h|}}{C \lambda r_e \sqrt{F_H F_{\bar{H}}}}$$

- The symbols represent the following:

Λ_0	Pendellösung distance (or extinction distance)
V	unit cell volume
γ_o	cosine of the angle between the inward normal to the crystal surface and the incident direction
γ_h	cosine of the angle between the inward normal to the crystal surface and the reflected direction
r_e	classic electron radius. Value used: 2.818×10^{-15} m
λ	wavelength
C	polarisation factor
F_H	structure factor associated with reciprocal lattice node hkl
$F_{\bar{H}}$	structure factor associated with reciprocal lattice node $\bar{h}\bar{k}\bar{l}$

- The Darwin width is also calculated from equation (4.26) [Authier, 2001]:

$$\delta_{os} = \frac{\lambda}{\Lambda_0} \frac{|\gamma_h|}{\sin(2\theta)}$$

- In addition to the options of [ReflectionList](#), the following options can be given:

"Sort"	0	determines which column the table will be sorted by. Negative values reverses the direction.
"Keep"	All	truncates the table so that only a chosen number of reflections are displayed.

- Please see the documentation of [ReflectionCheck](#) for some examples of how to set the *condition*.
- For a given reflection to be listed in the table, it has to not be extinct and also yield **True** when tested by the *condition*. Sometimes, the table may appear to not comply with the condition set by *condition*. This may be due to symmetry equivalence with one of the reflections listed in the table, and can be checked by using the setting **True** for the "SplitEquivalent" option.

Examples (7)

Basic Examples (1)

To get an overview of which crystals have available data, use the following:

In[1]:= **\$Crystals**

```
Out[1]= {ag2so4_HTP_460C, ag2so4_HTP, ag2so4_LTP_340C, ag2so4_LTP, almgzn_Model_X_sim,
  almgzn_Model_Y_sim, aluminium, caf2, cof2, copper, corund, cuwo4, cuwo4_new,
  cuwo4_new_sasaki, diamond, gaas, german, german_new, glycyL-L-alanine, mgzn2_zero,
  mnsi, nacl, nickel, oxalic, silicon, silver_460C, silver, squaric, zinc_zero}
```

As an example, let the wavelength be 0.987 Å and the crystal NaCl, which has space group $Fm\bar{3}m$ (and thus Laue class $m\bar{3}m$).

In[2]:= **StructureFactorTable**[0.987, "nacl", "m $\bar{3}$ m"]

(hkl)	Structure factor F_{hkl}	Phase ϕ_{hkl} [°]	Bragg angle θ_B [°]	Pendellösung distance Λ_0 [µm]	Darwin width $2\delta_{os}$ [µrad]
(664)	11.194	2.749	55.167	103.400	1.163
(662)	13.827	2.539	49.712	94.768	1.365
(660)	14.861	2.468	47.942	91.346	1.455
(644)	15.988	2.397	46.182	87.756	1.559
(642)	20.043	2.182	40.904	76.414	1.973
(640)	21.670	2.109	39.122	72.547	2.156
(622)	25.461	1.960	35.479	64.812	2.624
(620)	27.685	1.883	33.600	60.965	2.926
(600)	30.186	1.805	31.668	57.135	3.290
(555)	6.245	-175.750	49.268	211.720	0.615
(553)	7.705	-175.920	42.229	194.740	0.754
(551)	8.437	-175.950	38.673	187.520	0.842
Out[2]= (533)	9.098	-175.920	35.014	182.410	0.943
(531)	9.602	-175.800	31.175	180.560	1.056
(511)	9.857	-175.550	27.043	183.100	1.186
(444)	23.467	2.035	37.317	68.676	2.371
(442)	30.186	1.805	31.668	57.135	3.290
(440)	33.024	1.724	29.668	53.318	3.740
(422)	40.101	1.550	25.383	45.655	5.043
(420)	44.671	1.454	23.036	41.746	6.042
(400)	50.323	1.349	20.487	37.721	7.476
(333)	9.857	-175.550	27.043	183.100	1.186
(331)	9.926	-175.190	22.421	188.710	1.371
(311)	10.768	-175.180	16.870	180.080	1.889
(222)	57.624	1.231	17.644	33.512	9.717
(220)	67.641	1.096	14.329	29.026	13.740
(200)	82.743	0.936	10.079	24.113	23.390
(111)	18.310	-176.920	8.717	109.390	5.953

Options (5)

"Sort" (2)

This option lets you sort the table by one of the columns. It needs to take an integer value that corresponds to one of the columns of the table.

Sort by increasing Bragg angle (fourth column from the left):


```
In[1]:= StructureFactorTable[0.70931713, "silicon",
  "m3m", {h_, k_, l_} /; OddQ[k] || Divisible[h + k + l, 4], "Sort" -> 4]
```

(hkl)	Structure factor F_{hkl}	Phase ϕ_{hkl} [°]	Bragg angle θ_B [°]	Pendellösung distance Λ_0 [μm]	Darwin width $2\delta_{os}$ [μrad]
(111)	59.374	-179.620	6.495	42.129	14.885
(220)	68.226	-179.540	10.644	36.265	10.589
(311)	44.717	-179.510	12.509	54.964	5.958
(400)	57.093	-179.470	15.142	42.564	6.380
(331)	38.199	0.554	16.538	63.180	3.944
(422)	49.473	0.594	18.658	48.213	4.599
(333)	33.235	0.618	19.836	71.255	2.934
(511)	33.235	0.618	19.836	71.255	2.934
(440)	43.239	0.658	21.680	54.106	3.549
(531)	29.112	0.683	22.727	79.764	2.302
(620)	38.004	0.726	24.395	60.330	2.847
(533)	25.639	-179.250	25.355	88.734	1.867
(444)	33.582	-179.200	26.900	66.857	2.345
(551)	22.700	-179.180	27.799	98.106	1.550
(711)	22.700	0.823	27.799	98.106	1.550
(642)	29.830	-179.130	29.255	73.633	1.971
(553)	20.203	-179.100	30.107	107.800	1.312
(731)	20.203	-179.100	30.107	107.800	1.312
(800)	26.635	0.943	31.496	80.595	1.685
(733)	18.074	-179.030	32.313	117.720	1.127
(660)	23.904	-178.980	33.650	87.672	1.460
(822)	23.904	-178.980	33.650	87.672	1.460
(555)	16.251	1.047	34.440	127.760	0.982
(751)	16.251	-178.950	34.440	127.760	0.982
(840)	21.559	-178.910	35.739	94.784	1.281
(753)	14.684	1.123	36.509	137.810	0.865
(664)	19.537	1.171	37.778	101.850	1.137
(844)	17.786	1.247	39.780	108.780	1.019
(755)	12.155	1.275	40.524	157.430	0.693
(771)	12.155	1.275	40.524	157.430	0.693
(862)	16.263	1.321	41.757	115.480	0.922
(773)	11.132	1.349	42.494	166.760	0.630
(775)	9.447	-178.510	46.407	183.760	0.533
(880)	12.730	1.537	47.632	133.270	0.720
(866)	11.816	-178.390	49.603	138.090	0.674
(884)	11.001	-178.330	51.596	142.160	0.637
(777)	7.579	-178.310	52.351	202.890	0.442

Sort by decreasing value of the structure factor (first column, a negative sign is used):

```
In[1]:= StructureFactorTable[0.70931713, "silicon", "m $\bar{3}$ m",
  {h_, k_, l_} /; OddQ[k] || Divisible[h + k + l, 4], "Sort" → -1]
```

	Structure factor	Phase	Bragg angle	Pendellösung distance	Darwin width
(hkl)	F_{hkl}	ϕ_{hkl} [°]	θ_B [°]	Λ_0 [μm]	$2\delta_{os}$ [μrad]
(111)	59.374	-179.620	6.495	42.129	14.885
(220)	68.226	-179.540	10.644	36.265	10.589
(311)	44.717	-179.510	12.509	54.964	5.958
(331)	38.199	0.554	16.538	63.180	3.944
(333)	33.235	0.618	19.836	71.255	2.934
(400)	57.093	-179.470	15.142	42.564	6.380
(422)	49.473	0.594	18.658	48.213	4.599
(440)	43.239	0.658	21.680	54.106	3.549
(444)	33.582	-179.200	26.900	66.857	2.345
(511)	33.235	0.618	19.836	71.255	2.934
(531)	29.112	0.683	22.727	79.764	2.302
(533)	25.639	-179.250	25.355	88.734	1.867
(551)	22.700	-179.180	27.799	98.106	1.550
(553)	20.203	-179.100	30.107	107.800	1.312
(555)	16.251	1.047	34.440	127.760	0.982
(620)	38.004	0.726	24.395	60.330	2.847
(642)	29.830	-179.130	29.255	73.633	1.971
(660)	23.904	-178.980	33.650	87.672	1.460
(664)	19.537	1.171	37.778	101.850	1.137
(711)	22.700	0.823	27.799	98.106	1.550
(731)	20.203	-179.100	30.107	107.800	1.312
(733)	18.074	-179.030	32.313	117.720	1.127
(751)	16.251	-178.950	34.440	127.760	0.982
(753)	14.684	1.123	36.509	137.810	0.865
(755)	12.155	1.275	40.524	157.430	0.693
(771)	12.155	1.275	40.524	157.430	0.693
(773)	11.132	1.349	42.494	166.760	0.630
(775)	9.447	-178.510	46.407	183.760	0.533
(777)	7.579	-178.310	52.351	202.890	0.442
(800)	26.635	0.943	31.496	80.595	1.685
(822)	23.904	-178.980	33.650	87.672	1.460
(840)	21.559	-178.910	35.739	94.784	1.281
(844)	17.786	1.247	39.780	108.780	1.019
(862)	16.263	1.321	41.757	115.480	0.922
(866)	11.816	-178.390	49.603	138.090	0.674
(880)	12.730	1.537	47.632	133.270	0.720
(884)	11.001	-178.330	51.596	142.160	0.637

"Keep" (1)

The "Keep" option truncates the table and keeps a desired amount of reflections in the table.

Let's say that we're only interested in the top nine strongest reflections:

```
In[1]:= StructureFactorTable[0.70931713, "silicon", "m $\bar{3}$ m",
  {h_, k_, l_} /; OddQ[k] || Divisible[h + k + l, 4], "Sort" → -2, "Keep" → 9]
```

	Structure factor	Phase	Bragg angle	Pendellösung distance	Darwin width
(hkl)	F_{hkl}	ϕ_{hkl} [°]	θ_B [°]	Λ_0 [μm]	$2\delta_{os}$ [μrad]
(220)	68.226	-179.540	10.644	36.265	10.589
(111)	59.374	-179.620	6.495	42.129	14.885
(400)	57.093	-179.470	15.142	42.564	6.380
(422)	49.473	0.594	18.658	48.213	4.599
(311)	44.717	-179.510	12.509	54.964	5.958
(440)	43.239	0.658	21.680	54.106	3.549
(331)	38.199	0.554	16.538	63.180	3.944
(620)	38.004	0.726	24.395	60.330	2.847
(444)	33.582	-179.200	26.900	66.857	2.345

"SplitEquivalent" (1)

By default, only one reflection from a set of symmetry equivalent reflections is represented in the table. This can be turned off by setting "SplitEquivalent" → `True`.

```
In[1]:= StructureFactorTable[0.70931713, "silicon", "m3m",
  {h_, k_, l_} /; h == 1 && Divisible[k, 3], "SplitEquivalent" -> True]
```

	Structure factor	Phase	Bragg angle	Pendellösung distance	Darwin width
(hkl)	F_{hkl}	ϕ_{hkl} [°]	θ_B [°]	Λ_0 [μm]	$2\delta_{os}$ [μrad]
(137)	20.203	0.897	30.107	107.800	1.312
(135)	29.112	0.683	22.727	79.764	2.302
(133)	38.199	-179.450	16.538	63.180	3.944
(131)	44.717	-179.510	12.509	54.964	5.958
(131)	44.717	0.489	12.509	54.964	5.958
(133)	38.199	0.554	16.538	63.180	3.944
Out[1]= (135)	29.112	-179.320	22.727	79.764	2.302
(137)	20.203	-179.100	30.107	107.800	1.312
(137)	20.203	-179.100	30.107	107.800	1.312
(135)	29.112	0.683	22.727	79.764	2.302
(133)	38.199	0.554	16.538	63.180	3.944
(131)	44.717	-179.510	12.509	54.964	5.958
(131)	44.717	-179.510	12.509	54.964	5.958
(133)	38.199	0.554	16.538	63.180	3.944
(135)	29.112	0.683	22.727	79.764	2.302
(137)	20.203	-179.100	30.107	107.800	1.312

"CustomReflections" (1)

`StructureFactorTable` produces a list of possible reflections automatically, but this step can be omitted if desired, and a list of custom reflections inputted instead.

```
In[1]:= StructureFactorTable[0.70931713, "silicon",
  "m3m", "CustomReflections" -> {{1, 1, 1}, {3, 1, 1}, {6, 4, 2}}]
```

	Structure factor	Phase	Bragg angle	Pendellösung distance	Darwin width
(hkl)	F_{hkl}	ϕ_{hkl} [°]	θ_B [°]	Λ_0 [μm]	$2\delta_{os}$ [μrad]
Out[1]= (111)	59.374	-179.620	6.495	42.129	14.885
(311)	44.717	-179.510	12.509	54.964	5.958
(642)	29.830	-179.130	29.255	73.633	1.971

Possible Issues (1)

In some cases, there may be additional extinct reflections:

```
In[1]:= StructureFactorTable[0.70931713, "silicon", "m3m"]
```

(hkl)	Structure factor F_{hkl}	Phase ϕ_{hkl} [°]	Bragg angle θ_B [°]	Pendellösung distance Λ_0 [μm]	Darwin width $2\delta_{os}$ [μrad]
(886)	0.000	0.000	56.751	ComplexInfinity	0.000
(884)	11.001	-178.330	51.596	142.160	0.637
(882)	0.000	0.000	48.615	ComplexInfinity	0.000
(880)	12.730	1.537	47.632	133.270	0.720
(866)	11.816	-178.390	49.603	138.090	0.674
(864)	0.000	0.000	44.696	ComplexInfinity	0.000
(862)	16.263	1.321	41.757	115.480	0.922
(860)	0.000	0.000	40.771	ComplexInfinity	0.000
(844)	17.786	1.247	39.780	108.780	1.019
(842)	0.000	0.000	36.764	ComplexInfinity	0.000
(840)	21.559	-178.910	35.739	94.784	1.281
(822)	23.904	-178.980	33.650	87.672	1.460
(820)	0.000	0.000	32.582	ComplexInfinity	0.000
(800)	26.635	0.943	31.496	80.595	1.685
(777)	7.579	-178.310	52.351	202.890	0.442
(775)	9.447	-178.510	46.407	183.760	0.533
(773)	11.132	1.349	42.494	166.760	0.630
(771)	12.155	1.275	40.524	157.430	0.693
(755)	12.155	1.275	40.524	157.430	0.693
(753)	14.684	1.123	36.509	137.810	0.865
(751)	16.251	-178.950	34.440	127.760	0.982
(733)	18.074	-179.030	32.313	117.720	1.127
(731)	20.203	-179.100	30.107	107.800	1.312
(711)	22.700	0.823	27.799	98.106	1.550
(666)	0.000	0.000	42.739	ComplexInfinity	0.000
(664)	19.537	1.171	37.778	101.850	1.137
(662)	0.000	0.000	34.702	ComplexInfinity	0.000
(660)	23.904	-178.980	33.650	87.672	1.460
(644)	0.000	0.000	32.582	ComplexInfinity	0.000
(642)	29.830	-179.130	29.255	73.633	1.971
(640)	0.000	0.000	28.094	ComplexInfinity	0.000
(622)	0.000	0.000	25.669	ComplexInfinity	0.000
(620)	38.004	0.726	24.395	60.330	2.847
(600)	0.000	0.000	23.068	ComplexInfinity	0.000
(555)	16.251	1.047	34.440	127.760	0.982
(553)	20.203	-179.100	30.107	107.800	1.312
(551)	22.700	-179.180	27.799	98.106	1.550
(533)	25.639	-179.250	25.355	88.734	1.867
(531)	29.112	0.683	22.727	79.764	2.302
(511)	33.235	0.618	19.836	71.255	2.934
(444)	33.582	-179.200	26.900	66.857	2.345
(442)	0.000	0.000	23.068	ComplexInfinity	0.000
(440)	43.239	0.658	21.680	54.106	3.549
(422)	49.473	0.594	18.658	48.213	4.599
(420)	0.000	0.000	16.981	ComplexInfinity	0.000
(400)	57.093	-179.470	15.142	42.564	6.380
(333)	33.235	0.618	19.836	71.255	2.934
(331)	38.199	0.554	16.538	63.180	3.944
(311)	44.717	-179.510	12.509	54.964	5.958
(222)	0.000	0.000	13.075	ComplexInfinity	0.000
(220)	68.226	-179.540	10.644	36.265	10.589
(200)	0.000	0.000	7.505	ComplexInfinity	0.000
(111)	59.374	-179.620	6.495	42.129	14.885

Here, the silicon has space group #227 in the *International Tables for Crystallography*. For this particular case, we find that the extra reflection condition $h = 2n + 1$ or $h + k + l = 4n$ must be fulfilled. This will have to be incorporated as a *condition*:

```
In[2]:= StructureFactorTable[0.70931713, "silicon",
  "m3m", {h_, k_, l_} /; OddQ[k] || Divisible[h + k + l, 4], "Sort" -> 4]
```

(hkl)	Structure factor F_{hkl}	Phase ϕ_{hkl} [°]	Bragg angle θ_B [°]	Pendellösung distance Λ_0 [μm]	Darwin width $2\delta_{os}$ [μrad]
(111)	59.374	-179.620	6.495	42.129	14.885
(220)	68.226	-179.540	10.644	36.265	10.589
(311)	44.717	-179.510	12.509	54.964	5.958
(400)	57.093	-179.470	15.142	42.564	6.380
(331)	38.199	0.554	16.538	63.180	3.944
(422)	49.473	0.594	18.658	48.213	4.599
(333)	33.235	0.618	19.836	71.255	2.934
(511)	33.235	0.618	19.836	71.255	2.934
(440)	43.239	0.658	21.680	54.106	3.549
(531)	29.112	0.683	22.727	79.764	2.302
(620)	38.004	0.726	24.395	60.330	2.847
(533)	25.639	-179.250	25.355	88.734	1.867
(444)	33.582	-179.200	26.900	66.857	2.345
(551)	22.700	-179.180	27.799	98.106	1.550
(711)	22.700	0.823	27.799	98.106	1.550
(642)	29.830	-179.130	29.255	73.633	1.971
(553)	20.203	-179.100	30.107	107.800	1.312
(731)	20.203	-179.100	30.107	107.800	1.312
(800)	26.635	0.943	31.496	80.595	1.685
(733)	18.074	-179.030	32.313	117.720	1.127
(660)	23.904	-178.980	33.650	87.672	1.460
(822)	23.904	-178.980	33.650	87.672	1.460
(555)	16.251	1.047	34.440	127.760	0.982
(751)	16.251	-178.950	34.440	127.760	0.982
(840)	21.559	-178.910	35.739	94.784	1.281
(753)	14.684	1.123	36.509	137.810	0.865
(664)	19.537	1.171	37.778	101.850	1.137
(844)	17.786	1.247	39.780	108.780	1.019
(755)	12.155	1.275	40.524	157.430	0.693
(771)	12.155	1.275	40.524	157.430	0.693
(862)	16.263	1.321	41.757	115.480	0.922
(773)	11.132	1.349	42.494	166.760	0.630
(775)	9.447	-178.510	46.407	183.760	0.533
(880)	12.730	1.537	47.632	133.270	0.720
(866)	11.816	-178.390	49.603	138.090	0.674
(884)	11.001	-178.330	51.596	142.160	0.637
(777)	7.579	-178.310	52.351	202.890	0.442

Related Guides

- [X-Ray Diffraction Package](#)

ReflectionConditionCheck

ReflectionConditionCheck [*imgfile*, *system*, *P*₁, *P*₂, *l*, *pattern*]

plots reciprocal lattice nodes that match *pattern* in *imgfile*. See details for syntax meaning.

Details




- imgfile* must be a string that represents an image file. *system* denotes the crystal system (currently, only "Hexagonal" is supported). *P*₁ and *P*₂ are two points each containing a reciprocal lattice node and the corresponding pixel coordinate set by *CrysAlis*. Format: $P_i = \{\{h_i, k_i\}, \{x_i, y_i\}\}$. Example of such points:

```
In[1]:= {p1, p2} = {
  {{3, 0}, {983, 739}},
  {{0, 3}, {912, 862}}
};
```

- l* denotes the third Miller index and is used to check whether the image matches a given reflection condition set by *pattern*. The *pattern* must be a [Condition](#) that restricts the values of *hkl* somehow. Examples:

$\{h_, k_, l_ \} /; \text{EvenQ}[h]$	reflections with even values of <i>h</i>
$\{h_, k_, l_ \} /; \text{Divisible}[h + k, 4]$	reflections where <i>h + k</i> is divisible by 4
$\{h_, k_, l_ \} /; h = 0 \mid \mid l = 3$	reflections where either <i>h = 0</i> or <i>l = 3</i>

- There may be up to three different groups in the output data:

	Reciprocal lattice nodes <i>not</i> matching the pattern
	Reciprocal lattice nodes matching the pattern
	Weak or invalid nodes

- Please keep in mind that the algorithm filtering invalid nodes is not optimal at the moment.
- In addition to the options of [FindPixelClusters](#) and the three options [Frame](#), [ImageSize](#) and [PlotRange](#) from [Plot](#), further settings may be assigned with the following:

"CountNonInteger"	False	whether to display the number of non-integer nodes
"Threshold"	0.35	threshold for rounding Miller indices to nearest integer
"Round"	True	whether to round pixels to nearest integer when checking reciprocal nodes with the image lattice
"LoadPixelData"	False	option for loading \$PixelData from a file
"RetrieveData"	True	whether to check \$PixelData
"LatticeMethod"	"Correspondence"	method for establishing the image lattice
"Colours"	{col ₁ , col ₂ , col ₃ }	specify the colours in output

- The option "LatticeMethod" has two settings:

"Correspondence"
"Scaling"

- With "LatticeMethod" → "Correspondence", the lattice of the image is determined from the linear system for the *b* matrix:

$$\begin{pmatrix} h_1 & k_1 \\ h_2 & k_2 \end{pmatrix} \begin{pmatrix} b_{11} & b_{12} \\ b_{21} & b_{22} \end{pmatrix} = \begin{pmatrix} x_1^* & x_2^* \\ y_1^* & y_2^* \end{pmatrix}$$

- where the stars denote modified values;

$$x_i^* = x_i - mid_x \quad y_i^* = y_i - mid_y \quad \{mid_x, mid_y\} = \mathbf{ImageDimensions}[image] / 2 + 1$$

- to compensate for the difference in the origin of the pixels and the origin of the reciprocal space in the image. A basis change from b to B , the reciprocal lattice of *CrysAlis*, is then realised with:

$$\Gamma = \mathbf{Inverse}[B \cdot \mathbf{Inverse}[B] \cdot b]$$

- Finally, for any pixel coordinate $\{x, y\}$, the reciprocal lattice point associated with that coordinate is now found by computing:

$$\Gamma \cdot (\{x, y\} - (\{mid_x, mid_y\} + 1))$$

- With "LatticeMethod" \rightarrow "Scaling", the lattice basis Γ is found like with the "Correspondence" method, but with the final inversion operation substituted with a transposition. Afterwards, Γ is divided by B componentwise. The mean of the resulting components are taken to be a scaling factor c , and the lattice is instead defined by:

$$\Gamma' = \mathbf{Inverse}[c * \mathbf{Transpose}[B]]$$

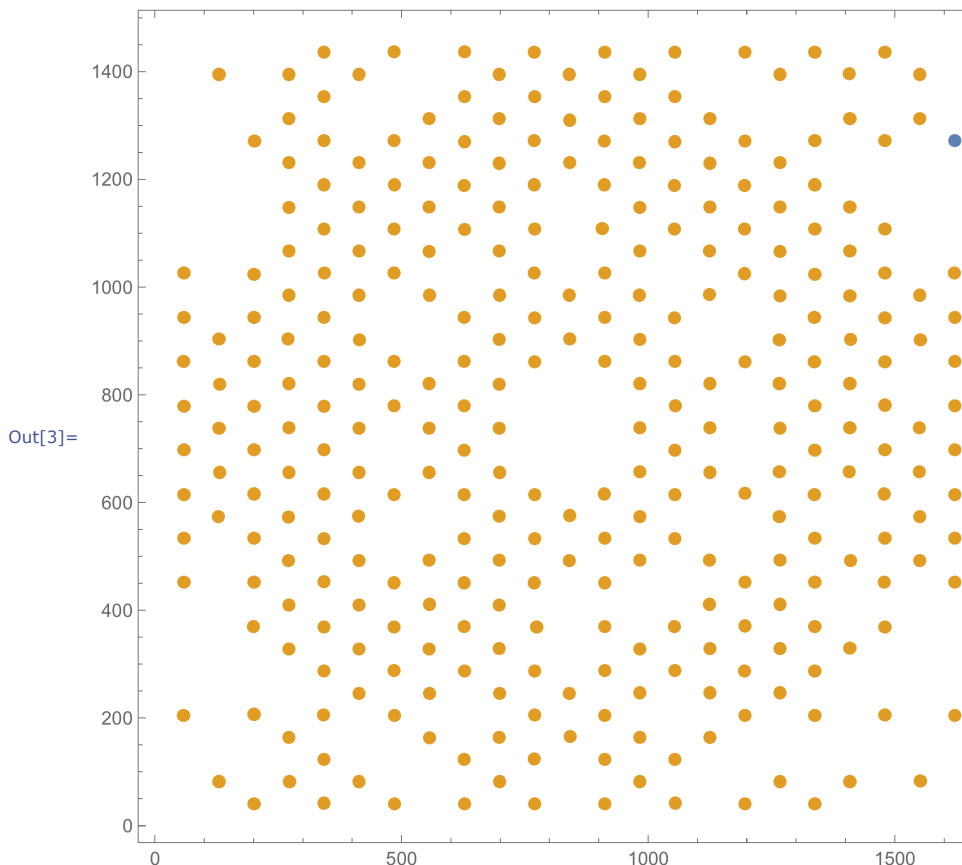
Examples (9)

Basic Examples (2)

```
In[1]:= imagel = FileNameJoin[
  {$XrayExamples, "Unwarps", "Crystal_1_(01)_290K_UnwarpTemp_20perunit_001.bmp"}];
```

```
In[2]:= {p1, p2} = {{{3, 0}, {983, 739}}, {{0, 3}, {912, 862}}};
```

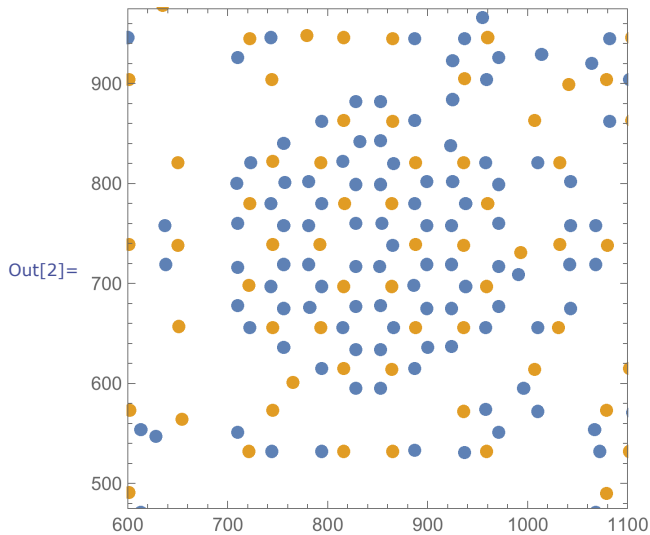
```
In[3]:= ReflectionConditionCheck[
  imagel,
  "Hexagonal",
  p1, p2,
  0,
  {h_, k_, l_} /; Divisible[h - k + l, 3],
  "DeleteSmallComponents"  $\rightarrow$  "Mean"]
```



```
In[1]:= image2 = FileNameJoin[
  {$XrayExamples, "Unwarps", "Crystal_1_(05)_165K_UnwarpTemp_20perunit_057.bmp"}];
```

Use the `PlotRange` option to zoom in on a specific region:

```
In[2]:= ReflectionConditionCheck[
  image2,
  "Hexagonal",
  {{3, 0}, {983, 739}},
  {{0, 3}, {912, 862}},
  0,
  {h_, k_, l_} /; IntegerQ[h] && IntegerQ[k],
  PlotRange -> {{600, 1100}, {475, 975}}]
```



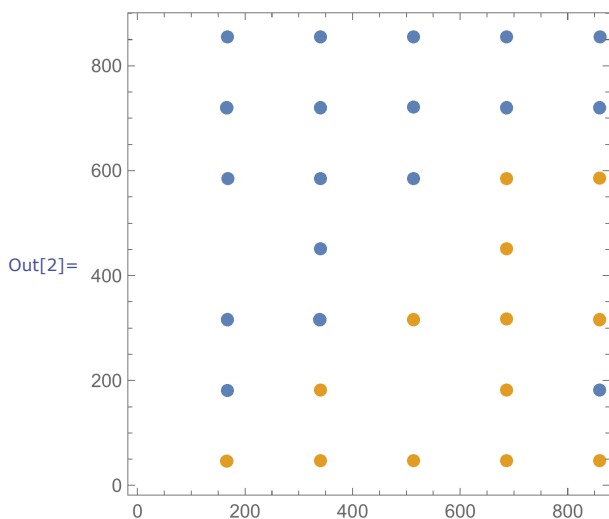
Options (7)

"CountNonInteger" (1)

```
In[1]:= image3 = FileNameJoin[{$XrayExamples, "Unwarps", "Crystal_2_(test1)_290K_autotest_4.bmp"}];
```

```
In[2]:= ReflectionConditionCheck[
  image3,
  "Hexagonal",
  {{3, 0}, {983, 739}},
  {{0, 3}, {912, 862}},
  0,
  {h_, k_, l_} /; h - k > 1,
  ImageSize -> Medium,
  "CountNonInteger" -> True]
```

ReflectionConditionCheckthreshold: 17 reflections were outside the threshold for integer determination >>

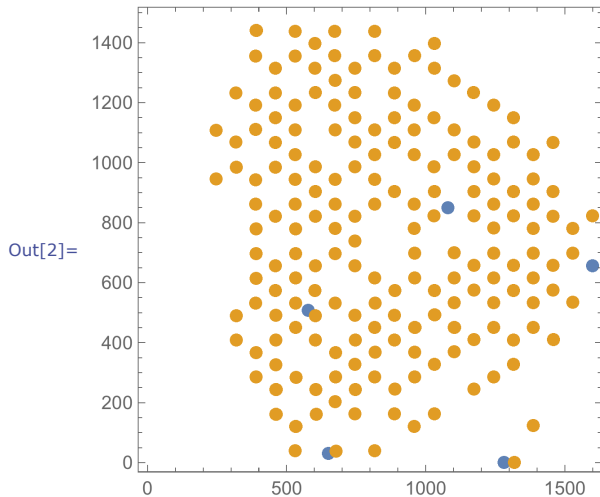


"Threshold" (2)

```
In[1]:= image3 = FileNameJoin[{$XrayExamples, "Unwarps", "Crystal_4_(01)_290K_20perunit_021.bmp"}];
```

```
In[2]:= ReflectionConditionCheck[
  image3,
  "Hexagonal",
  p1, p2,
  1, {h_, k_, l_} /; IntegerQ[h] && IntegerQ[k],
  "Threshold" → 0.25,
  "CountNonInteger" → True]
```

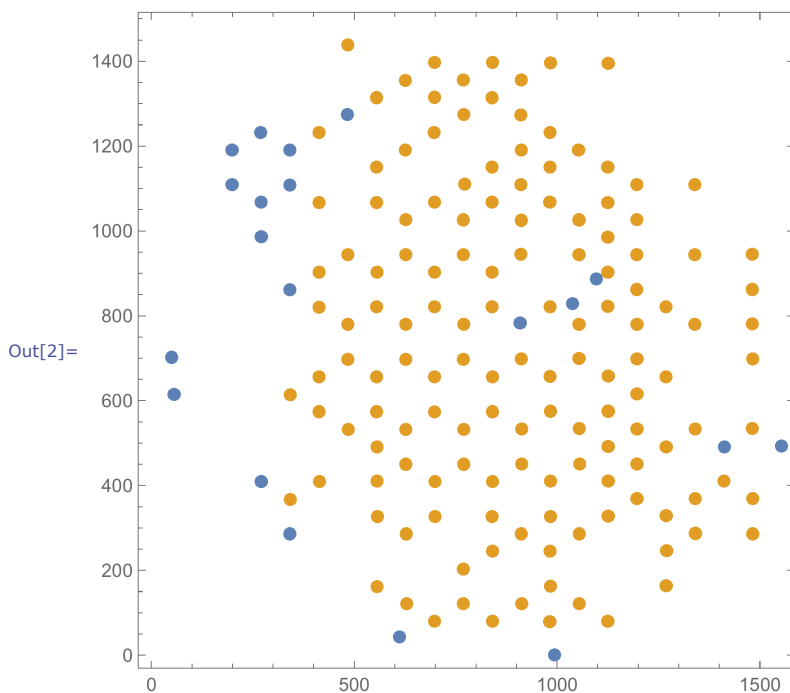
ReflectionConditionCheckthreshold: 4 reflections were outside the threshold for integer determination >>



```
In[1]:= image4 = FileNameJoin[{$XrayExamples, "Unwarps", "Crystal_4_(01)_290K_20perunit_061.bmp"}];
```

```
In[2]:= ReflectionConditionCheck[
  image4,
  "Hexagonal",
  p1, p2,
  3, {h_, k_, l_} /; IntegerQ[h] && IntegerQ[k],
  "Threshold" → 0.10,
  "CountNonInteger" → True]
```

ReflectionConditionCheckthreshold: 19 reflections were outside the threshold for integer determination >>



"Round" (1)

Once the lattice of the image has been determined, a «pixel-to-node» function ξ is defined for converting pixels to nodes.

```
In[1]:=  $\xi(x, y) : (x, y) \rightarrow (h, k)$ 
```

An inverse «node-to-pixel» function χ is also defined. The option "Round" decides whether to round the assigned pixels to nearest integer.

```
In[2]:=  $\chi(h, k) : (h, k) \rightarrow (x, y)$ 
```

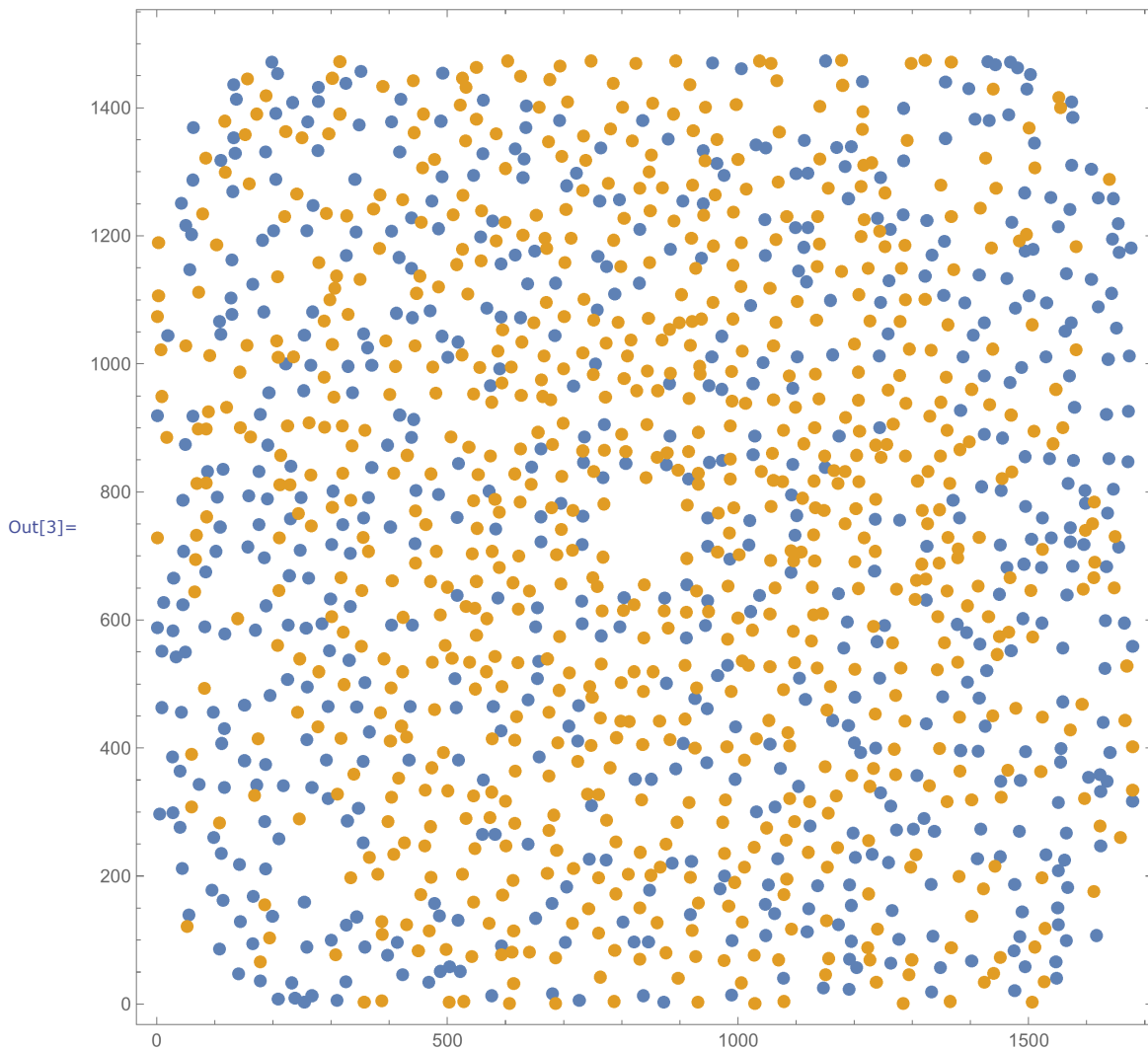
"LoadPixelData" (1)

`GeneratePixelData` may be used to map `FindPixelClusters` on a batch of images and store the data in a file. Load that file with this option.

```
In[1]:= datafile = FileNameJoin[{$XrayExamples, "Unwarps", "PixelData_example.dat"}];
```

```
In[2]:= image5 = FileNameJoin[
  {$XrayExamples, "Unwarps", "Crystal_1_(08)_100K_UnwarpTemp_20perunit_001.bmp"}];
```

```
In[3]:= ReflectionConditionCheck[
  image5,
  "Hexagonal",
  {{3, 0}, {983, 739}},
  {{0, 3}, {912, 862}},
  0,
  {h_, k_, l_} /; IntegerQ[h] && IntegerQ[k],
  "LoadPixelData" → datafile]
```



"RetrieveData" (1)

Set this option to `False` if you do not want `ReflectionConditionCheck` to check `$PixelData` for previously collected data.

Consider one of the example images:

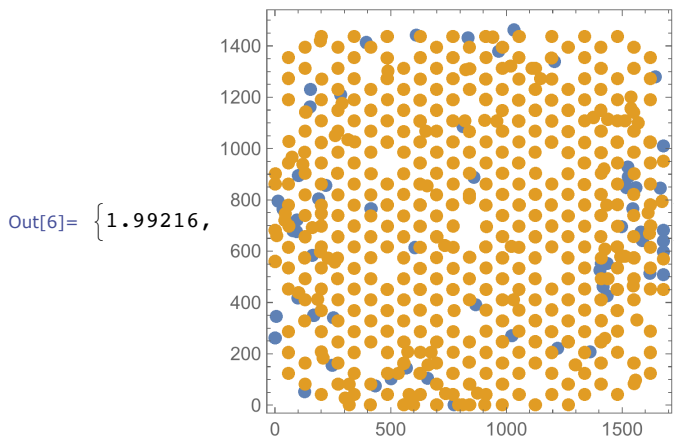
```
In[1]:= imagel = FileNameJoin[
  {$XrayExamples, "Unwarps", "Crystal_1_(01)_290K_UnwarpTemp_20perunit_001.bmp"}];
In[2]:= hash = IntegerString[FileHash[imagel], 16, 32]
Out[2]= 60942f0b0733577068956b00e2a5a54a
```

Confirm that pixel data for this image is contained in a given data file:

```
In[3]:= datafile = FileNameJoin[{$XrayExamples, "Unwarps", "PixelData_example.dat"}];
In[4]:= $PixelData = ToExpression@Import[datafile, "String"];
In[5]:= KeyExistsQ[$PixelData, hash]
Out[5]= True
```

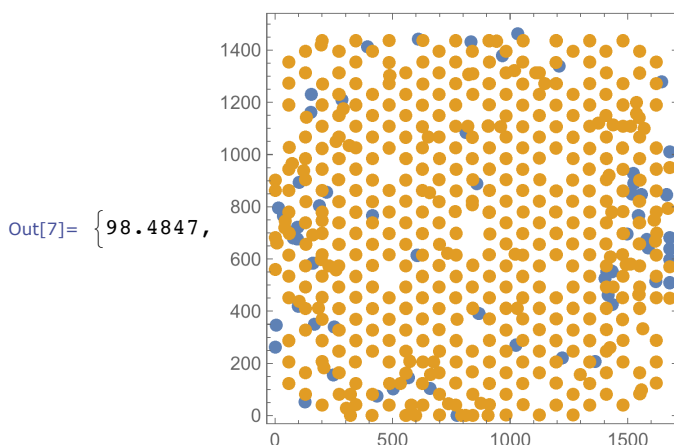
Computation where data is loaded:

```
In[6]:= Timing@ReflectionConditionCheck[imagel, "Hexagonal", p1, p2, 0,
  {h_, k_, l_} /; IntegerQ[h + k]]
```



Computation where data is *not* loaded:

```
In[7]:= Timing@ReflectionConditionCheck[imagel, "Hexagonal", p1, p2, 0,
  {h_, k_, l_} /; IntegerQ[h + k],
  "RetrieveData" → False]
```



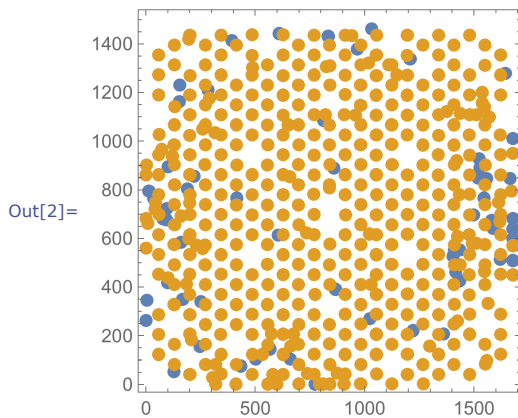
"LatticeMethod" (1)

The slight difference in the methods may for instance be seen by the number of reflections that fall outside the threshold for integer determination.

```
In[1]:= imagel = FileNameJoin[
  {$XrayExamples, "Unwarps", "Crystal_1_(01)_290K_UnwarpTemp_20perunit_001.bmp"}];
```

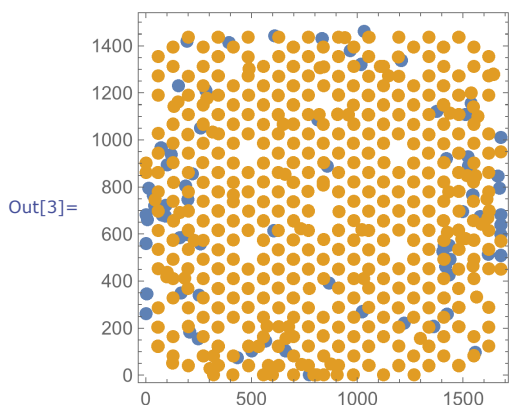
```
In[2]:= type1 = ReflectionConditionCheck[
  imagel,
  "Hexagonal",
  {{3, 0}, {983, 739}},
  {{0, 3}, {912, 862}},
  0,
  {h_, k_, l_} /; IntegerQ[h] && IntegerQ[k],
  "LatticeMethod" → "Correspondence",
  "CountNonInteger" → True]
```

ReflectionConditionCheckthreshold 58 reflections were outside the threshold for integer determination >>



```
In[3]:= type2 = ReflectionConditionCheck[
  imagel,
  "Hexagonal",
  {{3, 0}, {983, 739}},
  {{0, 3}, {912, 862}},
  0,
  {h_, k_, l_} /; IntegerQ[h] && IntegerQ[k],
  "LatticeMethod" → "Scaling",
  "CountNonInteger" → True]
```

ReflectionConditionCheckthreshold 71 reflections were outside the threshold for integer determination >>



Related Guides

- [X-Ray Diffraction Package](#)

RefinedValues

RefinedValues [*file*]

extracts the instrument parameters from a *CrysAlis* log *file*.

RefinedValues [*project*]

extracts the instrument parameters given a *CrysAlis* *project* path.

RefinedValues [*file* / *project*, "UB"]

extracts the *UB*-, *U*- and *B* matrices from the *CrysAlis* *file* or *project*.

Details

- The output is a list with four sublists. The first sublist contains information about the reflections:

initial number of reflections
final number of reflections

- The second sublist contains:

the residue parameter R_{int}

- The third sublist contains information about the unit cell:

<i>a</i> lattice paramter
<i>b</i> lattice paramter
<i>c</i> lattice paramter
α interaxial angle
β interaxial angle
γ interaxial angle

- The fourth sublist contains information about the orientation of the crystal:

crystal rotation about x-axis	Cryst. Rot. X	r1
crystal rotation about y-axis	Cryst. Rot. Y	r2
crystal rotation about z-axis	Cryst. Rot. Z	r3
crystal wobbling about x-axis	Cryst. Dance X	w1
crystal wobbling about y-axis	Cryst. Dance Y	w2
crystal wobbling about z-axis	Cryst. Dance Z	w3

- The fifth sublist contains information about the goniometer:

beam rotation about y-axis	Beam. Rot. Y	b2
beam rotation about z-axis	Beam. Rot. Z	b3
goniometer angle α	Alpha Value	a1
goniometer angle β	Beta Value	be
goniometer zero ω	Omega Offset	o0
goniometer zero θ	Theta Offset	t0
goniometer zero κ	Kappa Offset	k0
goniometer zero ϕ	Phi Offset	p0

- The sixth sublist contains information about the detector:

detector rotation about x-axis	Det. Rot. X	d1
detector rotation about y-axis	Det. Rot. Y	d2
detector rotation about z-axis	Det. Rot. Z	d3
detector offset of x-axis	Det. Offset X	x0
detector offset of y-axis	Det. Offset Y	y0
detector distance scale	Det. D. Scale	dd

- *CrysAlis* will sometimes also give the *UB* orientation matrix in the so-called *Busing & Levy* style, which utilises the *Cholesky decomposition* instead of QR decomposition. The Cholesky decomposition is an upper-triangular matrix that is also conjugate transpose of the input matrix. The *U* matrix will in any case be identical. If we let *g* denote the unit cell metric, then the *B* will be the Cholesky decomposition of the inverse of *g*.

Examples (2)

Basic Examples (2)

```
In[1]:= logfile = FileNameJoin[{$XrayExamples, "logfile.txt"}];
```

```
In[2]:= RefinedValues[logfile]
```

```
Out[2]= {{8569, 5957}, {0.003155},
{16.373108, 16.373679, 12.404242, 89.999096, 89.999335, 120.001241},
{-176.979626, 0.112673, -151.793781, 0.000000, 0.000000, 0.000000},
{0.008930, 0.000000, 50.000000, 0.000000, 0.000000, 0.000000, 0.000000, 0.000000},
{0.047939, 0.000074, -0.161940, 26.646797, 741.454074, 146.433622}}
```

Extracting the *UB* orientation matrix and its QR (orthogonal and upper-triangular) components:

```
In[1]:= logfile = FileNameJoin[{$XrayExamples, "logfile.txt"}];
```

```
In[2]:= mat = RefinedValues[logfile, "UB"]
```

```
Out[2]= {{{-0.0433835, -0.00156628, 0.00130457},
{0.0232678, 0.0491491, 0.00266427}, {0.0000971083, 0.00229504, -0.0561961}},
{{-0.881253, 0.472077, 0.023170}, {0.472641, 0.879981, 0.047369},
{0.001973, 0.052695, -0.998609}}, {{0.049229, 0.024615, -0.000001},
{0.000000, 0.042632, -0.000001}, {0.000000, 0.000000, 0.056274}}}
```

The output consists of three 3×3 matrices, the *UB*-, *U*- and *B* matrices:

```
In[3]:= Dimensions@mat
```

```
Out[3]= {3, 3, 3}
```

```
In[4]:= MatrixForm /@ mat
```

```
Out[4]= { { { -0.0433835 -0.00156628 0.00130457 }
{ 0.0232678 0.0491491 0.00266427 }
{ 0.0000971083 0.00229504 -0.0561961 }
{ -0.881253 0.472077 0.023170 }
{ 0.472641 0.879981 0.047369 }
{ 0.001973 0.052695 -0.998609 } }
, { { 0.049229 0.024615 -0.000001 }
{ 0.000000 0.042632 -0.000001 }
{ 0.000000 0.000000 0.056274 } } }
```

Related Guides

- [X-Ray Diffraction Package](#)

6.2 Appendix B – Details of the *CrysAlis* procedures

6.2.1 Silicon data processing

1. Use the *Crysis* application in the *SNBL ToolBox* to generate a `.par` file from the `.cbf` files.
2. Open *CrysAlis* version 171.37.35h.
3. A message about having got set «basic settings» may appear. Click «OK» then «OK» again.
4. Use «Browse experiments» to locate the `.par` file from step 1.
5. Go to [Lattice wizard] » Peak hunting], but click on the option button to select «Peak hunting with user settings»
 - 5.1. Set «Threshold» to 20 and «7×7 average» to 1.
 - 5.2. Click «OK» and wait for the program to find peaks.
6. Go to [Lattice wizard] » Unit cell finding] but, again, use the option button to select «Unit cell finding with options».
 - 6.1. Check the «Search known cell» box in the last setup section and write:
5.431 5.431 5.431 90.00 90.00 90.00.
 - 6.2. Click «OK»
 Go to [Lattice wizard] » Refine instrument model] but use the option button to select «Refine instrument model with user settings»
 - 6.1. Deselect «Automatic selection of parameters» near the top right corner.
 - 6.2. In the first pop-up box choose LAT_AAA.
 - 6.3. In the next pop-up box choose ANG_909090.
 - 6.4. Uncheck the box for the lattice constant *a* and edit its value to be 5.431.
 - 6.5. Uncheck the box next to ω .
 - 6.6. Check the box next to τ .
 - 6.7. Click «OK».
7. Go to [Lattice wizard] » Ewald explorer] but use the option button to select «Peak table editing».
 - 7.1. Sort the table by «intensity», in increasing value from top to bottom.
 - 7.2. Delete values that have an intensity of about 100 or lower. (A range of values can be selected by click in the first one, holding the \uparrow key, then selecting the last one. A quick way to reach the top or bottom is to use [Page Up] or [Page Down] keys, which can be combined with the \uparrow button.)
 - 7.3. Sort the table by «angles» in the «Coordinates» section at the bottom. Go through the list manually and look for listings of the same *hkl* value, but where one of them as a weak intensity. Delete the weaker listings.
 - 7.4. Select all the values and click on «Copy to Clip» and save it off in a `.dat` file. Use the label `goniometer` somewhere in the filename.
 - 7.5. In the «Coordinates» section, change to «detector» and save the new table to another `.dat` file labelled `detector` somewhere in the filename.
 - 7.6. Click on «Exit» when done
8. Go to [Lattice wizard] » Refine instrument model] but use the option «Refine instrument model with user settings».
 - 8.1. Check the box by the lattice constant *a*.
 - 8.2. Click «OK».
9. In the [Lattice wizard] click on «Save information», then «Close».
10. Go to the [Command shell] using the button in the left panel.
 - 10.1. Type `ty u` and hit \leftarrow .
 - 10.2. Locate the data for the *UB* matrix in the console. Copy it and store it in a `.dat` file. Use the label `ubmatrix` somewhere in the filename. It should be a line looking something like:

```
UM S 9.2230804E-002 4.4456168E-002 7.4967560E-002  
5.6571981E-002 -1.1356460E-001 -2.2620480E-003  
6.6334529E-002 3.5113183E-002 -1.0240130E-001
```

- 10.3. In the command shell, click on «Options RED».
- 10.4. In the program window click on the «Monochromator» tab.
- 10.5. Click on «Edit `polfac`» and set its value to 0.05. Click «OK».
- 10.6. Check the «Save to par file on exit» box in the lower left corner. Click «OK», and then «Yes» when a warning message pops up.
- 10.7. Close the commando shell.
11. Data reduction – versions 171.37.35h and 171.38.41 have issues with this step, but version 171.35.21 works.
 - 11.1. On the right-hand menu click on the text «Data reduction» and choose «Data reduction with options» (second from the top).
 - 11.2. In the «Profile fitting data reduction» window click on the «Next» button until step 5.
 - 11.3. In step 5 choose «Don't use outlier rejection». Go to the next step.
 - 11.4. In step 6 choose «Manual» in the «Finalization options» section and click on «Finish».
 - 11.5. Wait for the processing to finish (this will take some time).
12. Determining the space group – You may now choose to go back to version 171.37.35h.
 - 12.1. If the «Space group determination» window did not open upon completing the previous task, it may be executed from `[Data reduction]»Finalize]`.
 - 12.2. In the main window make sure the correct `.hkl` file is displayed and click «Apply».
 - 12.3. In the «Centering» tab make sure the «Lattice type» is set to *F*.
 - 12.4. Keep clicking «Apply» until the «Ins-File» tab appears. Set *Z* to 8 and type `Si` in the «Chemical formula».
 - 12.5. Click «Finish». The program should produce a reflection file (`.hkl`) in the directory `(Project directory)»struct»temp`.
13. Gather the relevant output files for the project (`goniometer.dat`, `detector.dat`, `ubmatrix.dat` and `<project name>.hkl`).

6.2.2 Room temperature thiourea-ferrocene treatment

1. Use the *Crysis* application in the *SNBL ToolBox* to generate a `.par` file from the `.cbf` files. No binning.
2. Open *CrysAlis* version 1.171.38.41.
3. Go to `Command shell` \gg `Options RED`.
 - 3.1. In the tab `Instrument model I` set `x` to 27 and `y` to 741.
 - 3.2. In the tab `Monochromator` set `pol fac` to 0.05.
 - 3.3. Check «Save par file on exit» and exit the commando shell.
4. Go to `Lattice Wizard` \gg `Peak hunting` and perform an automatic peak hunt.
5. Go to `Lattice Wizard` \gg `Unit cell finding` and let the program find the unit cell automatically.
6. Go to `Lattice Wizard` \gg `Refine instrument model` with users settings.
 - 6.1. Uncheck «Automatic selection of parameters». The next action depends on whether the crystal appears to be ferrocene or a thiourea-ferrocene clathrate.
 - 6.1.1. **Ferrocene:** Select the angles to be `ANG_90BE90`.
 - 6.1.2. **Thiourea-ferrocene:** Choose `LAT_AAB` and `ANG_9090120`. Uncheck `a` and `c`, and set their values to 16.3735 and 12.4041, respectively.
 - 6.2. Uncheck `w1`, `w2`, `w3` and `t0`.
 - 6.3. Press `[alt] + [E]` to reveal “hidden parameters”. Check all of `d1`, `d2`, `d3`, `x0`, `y0` and `dd` under «Detector» and click «OK».
7. Go to `Lattice Wizard` \gg `Ewald Explorer` \gg `Peak table editing` and delete reflections flagged with `wi`.
8. Go to `Lattice Wizard` \gg `Reindexation with current cell` and change the tolerance of indexation to 0.05.
 - 8.1. Go back to the peak table editing and delete reflections flagged as `wi`.
 - 8.2. Sort the table by the ϕ angle. Use the table with `PeakTableHelper` to find which registrations (that appear to be split across frames) to delete.
9. Perform a new refinement of the instrument model with user settings (all settings should be preserved).
 - 9.1. Take a screen shot of the `Lattice Wizard` \gg `Refine model` window.
 - 9.2. Go back to `Lattice Wizard` \gg `Ewald Explorer` \gg `Peak table editing`. Sort the table by «Goniometer» and save the table in a `.dat` file.
 - 9.3. Go to the `Command shell`. Type `ty u` and save the orientation matrix in a `.dat` file.
 - 9.4. Find the log file that has `red` in its file name in the log folder; $\text{Project directory} \gg \text{log} \gg \text{crysAlispro_red*.txt}$, and save it somewhere with the other `.dat`- and picture files.

Crystal	Filter	Other notes
0	—	same sample as crystal 1 (trial run)
1	—	
2	no	
3	✓	rather big with irregular shape
4	✓	
5	no	
6	no	
7	no	same sample as crystal 1
8	no	flawed
9	no	

Table 6.1: Some notes concerning the data sets.

6.2.3 Investigation of crystals 1 and 4

1. Use the *Crysis* application in the *SNBL ToolBox* to generate a `.par` file from the `.cbf` files. No binning[†].
2. Open *CrysAlis* version 1.171.38.41.
3. Go to [Command shell] » [Options RED].
 - 3.1. In the tab [Instrument model I] set:


```
d1      0.056 858 2
d2      -0.003 627 09
dd      146.391
x       26.9703
y       741.182
t0      -0.138 926
```
 - 3.2. In the tab [Instrument model II] set:


```
b2      -0.002 189 41
```
 - 3.3. In the tab [Monochromator] set:


```
polfac  0.05
```
 - 3.4. Check «Save to par file on exit» and exit the commando shell.
4. Go to [Lattice Wizard] » [Peak hunting] and perform an automatic peak hunt.
5. Go to [Lattice Wizard] » [Unit cell finding] and let the program find the unit cell automatically.
6. Go to [Lattice Wizard] » [Refine instrument model] with users settings.
 - 6.1. Uncheck «Automatic selection of parameters». The next action depends on whether the crystal appears to be ferrocene or a thiourea-ferrocene clathrate.
 - 6.1.1. **Ferrocene:** Select the angles to be ANG_90BE90.
 - 6.1.2. **Thiourea-ferrocene:** Choose LAT_AAB and ANG_9090120. Uncheck **a** and **c**, and set their values to 16.3735 and 12.4041, respectively.
 - 6.2. Uncheck **w1**, **w2**, **w3** and **t0**.
 - 6.3. Press [alt] + [E] to reveal “hidden parameters”. Move the value of **t0** to **d3**, set **t0** to zero and uncheck **t0**.
 - 6.4. Uncheck everything except the three **r** parameters and the lattice parameters. Click «OK».
7. Go to [Lattice Wizard] » [Ewald explorer] and take screenshots of:
 - the default view of the reciprocal space;
 - the views along the **a***, **b*** and **c***-axes;
8. Go to [Lattice Wizard] » [Ewald Explorer] » [Peak table editing] and delete reflections flagged with **wi**.
9. Go to [Lattice Wizard] » [Reindexation with current cell] and change the tolerance of indexation to 0.05.
10. Go back to the peak table editing and delete reflections flagged as **wi**.
11. Perform a new refinement of the instrument model with user settings (all settings should be preserved).
 - 11.1. Take a screen shot of the [Lattice Wizard] » [Refine model] window.
 - 11.2. Go back to [Lattice Wizard] » [Ewald Explorer] » [Peak table editing]. Sort the table by «Goniometer» and save the table in a `.dat` file.
 - 11.3. Go back to [Lattice Wizard] » [Ewald Explorer] and take new screenshots.
 - 11.4. Go to the [Commando shell]. Type `ty u` and save the orientation matrix in a `.dat` file.
 - 11.5. Find the log file that has **red** in its file name in the log folder; ⇨ (Project directory) » log » `crysalispro_red*.txt`, and save it somewhere with the other `.dat`- and picture files.
12. Click on «Save information» in the [Lattice Wizard] and exit *CrysAlis*.

[†] Binning data into bins of five was tried, but this resulted in reciprocal space reconstructions having lesser quality.

Miscellaneous *CrysAlis* notes and results

	Initially	After reindexation	2nd twin	Unindexed
Crystal_1_(01)_290K	97.03	99.61		
Crystal_1_(03)_200K		77.69		
Crystal_1_(04)_180K		78.14		
Crystal_1_(05)_165K	69.40	99.80	31.8	27
Crystal_1_(06)_155K	68	99.76		
Crystal_1_(07)_140K	49.44	56.90		
Crystal_1_(08)_100K	44.98	47.17	26.6	45
	43.12	27.51	29.2	43
Crystal_1_(09)_90K	45.46	50.96		
Crystal_1_(10)_100K	52.33	47.53	25.6	46
Crystal_1_(11)_140K	54.45	99.79	28.9	41
Crystal_1_(12)_155K	76.48	99.79		
Crystal_1_(13)_165K	80.74	99.86		
Crystal_1_(14)_180K	95.62	81.80		
Crystal_1_(15)_200K	86.23	99.61		
Crystal_1_(16)_240K	97.97	99.26		
Crystal_1_(17)_290K	99.06	99.14		

Table 6.2: Observations from treatment of crystal 1 data. Empty cells correspond to quantities that were not looked at. Data set 8 was redone as a check. «Initially» and «after reindexation» signify the percentage of peaks matching the current lattice. «Second twin» and «unindexed» represent the same, only for twinning analysis.

	Before transformation			After transformation		
	r1	r2	r3	r1	r2	r3
(01)_290K	-0.724 431	-9.478 273	70.788 002	-0.724 431	-9.478 273	70.788 002
(02)_240K	-0.839 393	-9.525 172	70.772 049	-0.839 393	-9.525 173	70.772 048
(03)_200K	172.164 593	5.539 002	-48.796 194	-0.914 878	-9.542 185	70.747 818
(04)_180K	-0.953 772	-9.557 753	70.719 486	-0.953 772	-9.557 754	70.719 485
(05)_165K	179.051 692	-9.572 049	70.718 081	-0.948 309	-9.572 049	70.718 080
(06)_155K	179.036 736	-9.582 367	70.747 824	-0.963 264	-9.582 368	70.747 823
(07)_140K	8.449 659	4.066 888	-169.251 108	-0.689 822	-9.346 117	70.992 250
(08)_100K	8.487 321	4.062 114	-169.185 122	-0.712 121	-9.376 132	71.058 021
(09)_90K	179.356 838	-9.340 375	71.140 806	-0.643 162	-9.340 373	71.140 806
(10)_100K	7.790 122	-5.221 809	131.499 877	-0.657 533	-9.347 437	71.091 342
(11)_140K	-179.382 023	9.335 749	-108.917 893	-0.617 977	-9.335 747	71.082 107
(12)_155K	-7.841 876	5.555 538	-48.817 986	-0.926 246	-9.555 940	70.723 515
(13)_165K	-7.839 875	5.548 454	-48.789 916	-0.920 992	-9.550 714	70.752 651
(14)_180K	-0.912 257	-9.545 419	70.756 170	-0.912 257	-9.545 419	70.756 170
(15)_200K	172.157 176	5.514 505	-48.810 913	-0.889 575	-9.536 527	70.736 579
(16)_240K	0.819 439	9.502 305	-109.212 514	-0.819 439	-9.502 306	70.787 485
(17)_290K	-172.159 359	-5.328 718	131.288 302	-0.726 817	-9.442 978	70.862 834

Table 6.3: The three rotation angles for the data sets of crystal 1, before and after transformation.

6.3 Appendix C – Miscellaneous

6.3.1 Alternative silicon intensities

Included here are alternative calculations of the silicon intensities (see subsection 3.1.2) by Thorkildsen. Intensities have been corrected by Lorentz and polarisation factors in addition to reduction in incident X-ray flux.

Si_A_0_0_0

hkl	I_{hkl}	$\sigma_{I_{hkl}}$	n_{hkl}	$i_{hkl,min}$	$i_{hkl,max}$	$\Delta(\%)$
440	23678.	767.	8	20000.	26067.	13.
400	23285.	717.	10	20471.	27499.	15.
422	22950.	563.	29	18609.	28442.	21.
620	21768.	790.	16	17991.	29273.	26.
444	20199.	428.	6	18894.	21882.	7.
220	19904.	1025.	10	15982.	25187.	23.
642	17708.	504.	8	15673.	20219.	13.
331	16167.	308.	30	12599.	18818.	19.
511	15548.	377.	33	11845.	20288.	27.
333	15531.	371.	6	13935.	16390.	8.
311	15425.	212.	42	12849.	18562.	19.
531	14370.	221.	44	12079.	17935.	20.
111	14068.	188.	16	13117.	15686.	9.
711	13062.	507.	9	10623.	14966.	17.
533	12822.	272.	16	11396.	14963.	14.
731	11906.	108.	1	11906.	11906.	0.
551	11581.	193.	14	10612.	13261.	11.

Si_B_0_0_0

hkl	I_{hkl}	$\sigma_{I_{hkl}}$	n_{hkl}	$i_{hkl,min}$	$i_{hkl,max}$	$\Delta(\%)$
422	35762.	654.	32	30036.	42000.	17.
400	34394.	655.	10	30490.	37819.	11.
220	34095.	1006.	14	30066.	40716.	16.
440	33804.	878.	15	27878.	39435.	17.
620	29475.	448.	16	26066.	34537.	14.
444	26797.	932.	6	24438.	30168.	11.
331	23583.	403.	26	20598.	28004.	16.
311	23042.	256.	42	19452.	27010.	16.
642	22724.	458.	10	20498.	25775.	12.
111	22078.	414.	16	19976.	26553.	15.
333	21678.	1047.	5	19659.	24558.	11.
511	20906.	228.	34	17222.	23336.	15.
531	18660.	185.	50	15676.	21319.	15.
533	15865.	294.	17	12782.	18413.	18.
711	13772.	166.	11	13167.	14706.	6.
551	13536.	133.	12	12850.	14147.	5.

Si_C_0_0_0

hkl	I_{hkl}	$\sigma_{I_{hkl}}$	n_{hkl}	$i_{hkl,min}$	$i_{hkl,max}$	$\Delta(\%)$
422	39737.	868.	31	32725.	50385.	22.
400	39319.	1462.	12	31795.	47530.	20.
440	38683.	1140.	10	35586.	48669.	17.
220	35137.	923.	16	30328.	44192.	20.
620	34338.	658.	18	29642.	39071.	14.
444	33479.	1862.	4	30409.	39187.	13.
642	27794.	635.	5	26035.	29700.	7.
331	26776.	373.	31	22471.	32877.	19.
311	26452.	531.	40	20906.	33946.	25.
511	25921.	418.	36	21359.	30465.	18.
333	25444.	602.	12	23377.	29627.	12.
531	23137.	315.	42	19457.	29027.	21.
111	22690.	720.	12	20090.	29449.	21.
533	20563.	499.	12	17853.	23766.	14.
551	17951.	458.	14	15039.	20912.	16.
711	17733.	447.	10	15886.	19461.	10.
731	15630.	124.	1	15630.	15630.	0.

Si_D_0_0_0

hkl	I_{hkl}	$\sigma_{I_{hkl}}$	n_{hkl}	$i_{hkl,min}$	$i_{hkl,max}$	$\Delta(\%)$
220	41324.	949.	16	35366.	46525.	14.
400	39934.	522.	10	38110.	43060.	6.
422	36129.	374.	32	32645.	40022.	10.
440	31486.	291.	8	30317.	32577.	4.
111	28420.	725.	16	23658.	31983.	15.
620	25940.	131.	17	25216.	27047.	4.
311	24992.	304.	42	21030.	28075.	14.
331	22387.	173.	36	20283.	24032.	8.
444	21312.	382.	5	20303.	22644.	5.
333	18869.	230.	11	17035.	19866.	8.
511	18725.	121.	30	16934.	19654.	7.
642	18226.	141.	5	17875.	18704.	2.
531	15374.	70.	46	14462.	16637.	7.
533	12590.	87.	14	12013.	13216.	5.
551	10423.	81.	14	10035.	11092.	5.
711	10400.	103.	12	9915.	11162.	6.
553	8860.	94.	1	8860.	8860.	0.
731	8568.	26.	2	8542.	8595.	0.

Si_E_0_0_0

hkl	I_{hkl}	$\sigma_{I_{hkl}}$	n_{hkl}	$i_{hkl,min}$	$i_{hkl,max}$	$\Delta(\%)$
422	65673.	1538.	28	48410.	81710.	25.
440	60834.	1760.	16	46177.	70178.	20.
220	60517.	2412.	14	46505.	73770.	23.
400	54701.	2192.	8	47195.	64087.	15.
620	51453.	1159.	15	44571.	59763.	15.
444	46041.	1752.	6	38516.	50700.	13.
311	41704.	833.	48	28802.	52384.	28.
331	40773.	813.	36	32410.	50325.	22.
642	39068.	1078.	12	32391.	45290.	17.
511	39033.	823.	20	32601.	44555.	15.
333	36926.	1395.	8	30621.	42529.	16.
111	35131.	1449.	16	27878.	46341.	26.
531	32311.	474.	44	24816.	37335.	19.
533	27698.	526.	18	22471.	31695.	17.
711	23527.	500.	15	20318.	26772.	14.
551	22924.	771.	8	19881.	25611.	12.
731	19317.	356.	2	18957.	19670.	2.

Figure 6.1: Silicon intensities calculated by Thorkildsen's *Mathematica* function, sorted by mean intensity.

6.3.2 Algorithm behind the `ReflectionConditionCheck` function

The procedures of this function can be broken into four main steps:

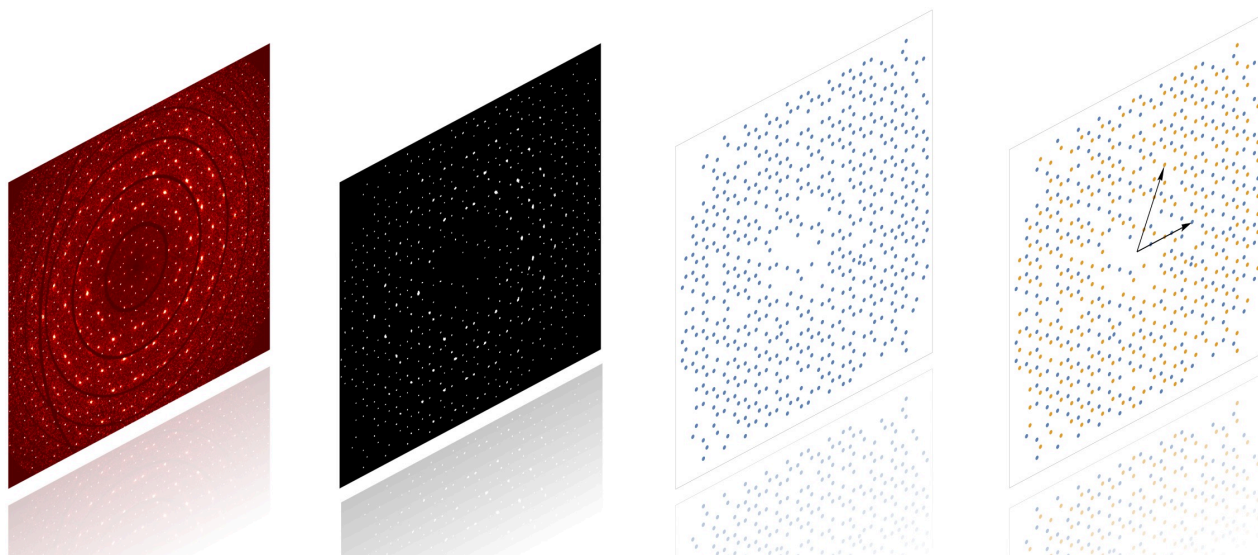


Figure 6.2: In order from left to right the first image shows a reconstruction of reciprocal space, which is the essential input to this function. The second image is a binarised version. Next is a plot of the two-dimensional list obtained from the previous image, and lastly we see reciprocal lattice superimposed on the image, representing a way to associate the points with reciprocal nodes.

The function requires four inputs:

1. An image of reciprocal space
2. The crystal system
3. Two correspondence points (will be explained shortly)
4. A reflection condition to highlight the points fulfilling this rule.

After importing the image it is binarised in order to simplify the task of converting “spots” to pixels. A challenge here is to find a balanced threshold, as having too much information in the image will take a great amount of processing time. Depending on the amount of pixels found in the binarised image, it may be further refined by removing noise with various built-in functions of *Mathematica*. `ReflectionConditionCheck` applies a suitable filtering method automatically, with threshold values based on trial and error.

The next step is the most time-consuming phase; Merging clusters of pixels to single points. This task is done by a standalone function called `FindPixelClusters`. The idea behind its algorithm is illustrated in Figure 6.3. It groups together pixels that neighbour other pixels one unit horizontally, vertically or diagonally – this is referred to as *8-connected*^[95]. When all pixels have been assigned to a cluster, each cluster is reduced to a single point by averaging the coordinates. The third picture in Figure 6.2 is an example of this result.

We now need the ability to associate any point found in the reconstructed image with the correct reciprocal node. For our purposes, it will suffice to construct a simple transformation matrix $\mathbf{P} : (x, y) \mapsto (h, k)$. Since translation has to be involved we have an affine transformation. In accordance with the *International Tables for Crystallography*, the transformations between bases is written on the form:^[96]

$$(\text{new basis}) = (\text{old basis}) \cdot \mathbf{P}, \quad (6.1)$$

where \mathbf{P} defines the *transformation matrix*. In this setting, the “old basis” is the system of pixel coordinates and the

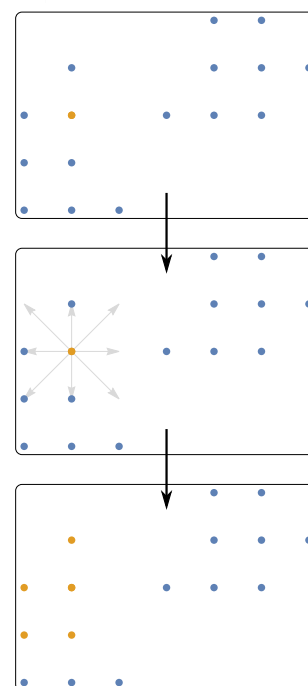


Figure 6.3: Example of how pixel clusters may look like if we zoom in. The three frames illustrate an iteration in the `FindPixelClusters` function. 8-connected pixels are joined together to eventually make a single cluster.

“new basis” the two-dimensional reciprocal hexagonal lattice used by *CrysAlis*. This reciprocal coordinate system is rotated 30° clockwise compared to the standard setting, resulting in \mathbf{a}^* pointing East and \mathbf{b}^* 60° North of East. The transformation matrix \mathbf{P} may be determined from two corresponding points in the old and new bases:

$$\mathbf{P} = \begin{bmatrix} \tilde{x}_1 & \tilde{x}_2 \\ \tilde{y}_1 & \tilde{y}_2 \end{bmatrix}^{-1} \begin{bmatrix} h_1 & h_2 \\ k_1 & k_2 \end{bmatrix}. \quad (6.2)$$

These have to be found manually by inspecting the reconstructed image in *CrysAlis*. In the case of hexagonal lattice and 0.8 Å resolution, the correspondence is found to be:

$$(3, 0)_{hk} \longleftrightarrow (983, 739)_{px} \quad (6.3a)$$

$$(0, 3)_{hk} \longleftrightarrow (912, 862)_{px} \quad (6.3b)$$

To compensate for the difference in the origin of the pixels (*CrysAlis* origin) and the origin of the reciprocal space in the image, a translation of the pixel coordinates is performed:

$$\tilde{x}_i = x_i - t_x, \quad \tilde{y}_i = y_i - t_y, \quad (6.4)$$

where (t_x, t_y) is an adjustment defined as the midpoint of the image plus one pixel unit. The pixel coordinates presented in (6.3) represent x_i and y_i in (6.4). When transforming the other way around this translation has to be reversed:

$$\tilde{h}_i = h_i + t_x, \quad \tilde{k}_i = k_i + t_y. \quad (6.5)$$

Coordinates may now be transformed back and forth by computing

$$\begin{bmatrix} h \\ k \end{bmatrix} = \mathbf{P} \begin{bmatrix} \tilde{x} \\ \tilde{y} \end{bmatrix}, \quad \begin{bmatrix} x \\ y \end{bmatrix} = \mathbf{P}^{-1} \begin{bmatrix} \tilde{h} \\ \tilde{k} \end{bmatrix}. \quad (6.6)$$

List of symbols

\square_j	If $\square = \{\mathbf{B}, \mathbf{D}, \mathbf{E}, \mathbf{H}\}$ and $j = \{\mathbf{o}, \mathbf{h}, \mathbf{g}\}$: Fourier component of \square associated with the given reciprocal lattice vector. $j = \{r, i\}$ denotes respectively the real and imaginary component of \square . (May be stacked with other indices.) 10	\mathbf{G}^{-1}	reciprocal space metric tensor. 21
A	absorption factor (correction of experimental measurements) 17	GoodF	goodness of fit. 19
a, b, c	lattice parameters/constants. 7	\mathbf{h}, \mathbf{g}	reciprocal lattice vector from the origin O of the reciprocal lattice to the reciprocal lattice node H or G ; $\mathbf{h} = \overrightarrow{OH}$, $\mathbf{g} = \overrightarrow{OG}$ etc. 7
$\mathbf{a}, \mathbf{b}, \mathbf{c}$	crystallographic vectors. 21	\mathbf{h}	reflection vector; the Miller indices hkl arranged in a column vector. 22
$\mathbf{B} (\mathbf{B}_\lambda)$	orthonormalisation matrix of reciprocal space (scaled by wavelength λ) 21	H	reciprocal lattice point or node. Its coordinates are given by a set of Miller indices, hkl 7
C	polarisation factor. 6	h, \bar{h}	either Miller index h or a reflection hkl , depending on the context. An overline indicates a reversed reflection; $\bar{h}kl$. h and \bar{h} are a <i>Friedel pair</i> 12
c	speed of light in vacuum. 12	I_{hkl}	intensity associated with Miller indices hkl 17
.cbf	crystallographic binary file 21	k	scaling factor (correction of experimental measurements) 17
CCD	charge-coupled device 24	\mathbf{K}_h	wave vector in reciprocal space associated with the reciprocal lattice vector \mathbf{h} . They were also called <i>Anregungsvektoren</i> («excitation vectors») by Ewald. ^[5] 10
\mathbf{D}	electric displacement field. 10	Lp	Lorentz-polarisation correction 17
d_{\min}	resolution; minimum interplanar spacing that may be resolved for a given wavelength and incidence angle (Bragg's law) 16	M	refinement on F or F^2 ; function to be minimised in least square procedures 19
\mathbf{E}	electric field. 10	\mathbf{n}	normal vector 13
\mathbf{e}_i	laboratory coordinate system, $i \in \{x, y, z\}$ 23	N	number of atoms in the unit cell. 7
\mathbf{e}_i^B	orthonormalised coordinate system of the unit cell, $i \in \{x, y, z\}$ 21	n	index of refraction 12
$\mathbf{e}_i^{C^*}$	crystallographic coordinate system, $i \in \{\mathbf{a}^*, \mathbf{b}^*, \mathbf{c}^*\}$ 21	n	order of reflection. 8
\mathbf{e}_i^{CA}	coordinate system used by <i>CrysAlis</i> , $i \in \{x, y\}$ 23	N_{ind}	number of independent reflections 19
ESRF	European Synchrotron Radiation Facility. 5	N_{par}	number of refined parameters 19
f', f''	corrections of the atomic scattering factor due to anomalous scattering 33	o	as an index, o indicates association with the origin of the reciprocal space. 12
$f(s)$	function for approximating scattering factors. $s = \sin(\theta)/\lambda$ 33	\mathbf{P}	matrix that transforms pixel coordinates (x, y) to Miller indices (h, k) for a given pair of correspondence points. 101
F_{obs}^2	observed intensity; follows from data reduction ($F_{\text{obs}}^2 \propto I_{\text{obs}}$) 18	P	tie point. It was also called <i>Anregungspunkt</i> («excitation point») by Ewald. ^[5] 10
$\langle F_{\text{obs}}^2 \rangle$	average intensity of a set of symmetry equivalent reflections. 18	$P(\mathbf{r})$	the Patterson function 18
F_{calc}	calculated structure factor from model 19	r_e	classical electron radius. 6
F_H	structure factor associated with reciprocal lattice node H , which has coordinates given by the Miller indices hkl in reciprocal space. 7	R_{int}	merging residual value; discrepancy among symmetry equivalent reflections. 18
f_n	atomic form factor (or atomic scattering factor) associated with atom n in the unit cell. 7	R_{sigma}	quality of observed structure factor. 18
		R_w	weighted R -factor 19
		S	goodness of fit. 19

s	shorthand for $\sin(\theta)/\lambda$	33	Λ_o	Pendellösung distance (in Laue-/transmission geometry) or extinction distance (in Bragg-/reflection geometry).....	14
SNBL	Swiss-Norwegian beamline.....	21	μ (μ_0)	permeability (permeability in vacuum).....	12
U	orthogonal rotation matrix.....	21	ν	frequency.....	12
UB	orientation matrix.....	21	$\rho_n(\mathbf{r})$	electron density distribution of atom n (evaluated at a position given by \mathbf{r}).....	7
V	unit cell volume.....	11	$\sigma_{\text{int}}(F_{\text{obs}}^2)$	standard uncertainty of intensity.....	18
w_i	weight; reciprocal of the uncertainty σ_i (may be squared).....	40	ς	scattering length. A measure of the interaction and the physical process generating the new wave.....	6
\bar{x}	weighted mean.....	40	σ_i	uncertainty of data set or measurement i	40
Δ	Laplacian. Generally defined as the divergence of the gradient.....	10	$\tilde{\sigma}_{\bar{x}}$	“external” standard deviation.....	40
ε (ε_0)	permittivity (permittivity in vacuum).....	12	$\Phi_{\mathbf{h}}$	amplitude of scattered wave (general).	6
θ	Bragg angle. Defined as the angle between the wave vector of the incident plane wave and the lattice planes.	8	χ	dielectric susceptibility.	10
λ	wavelength.....	11	χ_h	Fourier component of the dielectric susceptibility and associated with reciprocal lattice vector \mathbf{h}	11

List of figures

<p>2.1 Scattering from an incoming plane wave 6</p> <p>2.2 Elastic scattering geometry 6</p> <p>2.3 Ewald sphere 7</p> <p>2.4 Bragg diffraction 8</p> <p>2.5 Quantities involved in structure factor computation 8</p> <p>2.6 Mosaic crystal 9</p> <p>2.7 Difference between the kinematical- and the dynamical theory 9</p> <p>2.8 Dispersion surface 12</p> <p>2.9 Transmission- and reflection geometries 13</p> <p>2.10 Goniometer and diffractometer setup 23</p> <p>2.11 Initial <i>CrysAlis</i> flowchart 25</p> <p>2.12 <i>CrysAlis</i> screenshots 25</p> <p>2.13 Peak hunting wizard 25</p> <p>2.14 Additional (automatic) peak hunting method 25</p> <p>2.15 Ewald explorer 26</p> <p>2.16 Refine instrument model 26</p> <p>2.17 <i>CrysAlis</i>' «Unwarp» feature 27</p> <p>2.18 Data reduction (first four steps) 27</p> <p>2.19 Special parameters in data reduction 27</p> <p>2.20 Data reduction (last two steps) 28</p> <p>2.21 <i>SNBL Toolbox</i> main window and <i>Crysis</i> 28</p> <p>2.22 <i>SNBL Toolbox</i> – Converter 28</p> <p>2.23 Structure of ferrocene 29</p> <p>2.24 Structural formula of thiourea 30</p> <p>2.25 Perpendicular configurations of thiourea-ferrocene 30</p> <p>2.26 Phase transition plot from Sorai et al.^[3] 31</p> <p>3.1 Example of input and output of the <i>Mathematica</i> function <code>SfTable</code> 32</p> <p>3.2 Silicon reference data 35</p> <p>3.3 Input example for <code>IntensityTable</code> 35</p> <p>3.4 Intensity tables for the 0_0_0 settings 36</p> <p>3.5 Intensity tables for the Si_E_0_0_0 settings 37</p> <p>3.6 Plot of intensity data 39</p> <p>3.7 Automatic absorption corrections in <i>CrysAlis</i> 41</p>	<p>3.8 Manual absorption corrections in <i>CrysAlis</i> 42</p> <p>3.9 Flux plot 42</p> <p>3.10 Ferrocene streaks 43</p> <p>3.11 Reciprocal space reconstructions of crystal 3 43</p> <p>3.12 Crystal 3, (1<i>kl</i>) and (2<i>kl</i>) planes 44</p> <p>3.13 <i>Olex2</i> screenshot 45</p> <p>3.14 Ferrocene crystal structure 46</p> <p>3.15 Molecular axis of ferrocene 46</p> <p>3.16 Reconstructions of reciprocal space for crystal 1, room temperature 49</p> <p>3.17 smallcap 50</p> <p>3.18 Reconstructions of reciprocal space for crystal 1, room temperature 52</p> <p>3.19 Reflection splitting 53</p> <p>3.20 Distinction between 140 K and 100 K at (<i>hk</i>0) 53</p> <p>3.21 short 54</p> <p>3.22 Ring formation 54</p> <p>3.23 Intermediate reflections at (<i>h, k, 3.6</i>) and (<i>h, k, 5.6</i>) 55</p> <p>3.24 Intermediate patterns of crystal 1 57</p> <p>3.25 Complementary $l \pm 0.2$ modulations 58</p> <p>3.26 Reconstructions of reciprocal space for crystal 4, room temperature 60</p> <p>3.27 Small modulation in crystal 4 60</p> <p>3.28 Thiourea only structure 61</p> <p>3.29 Q-peaks surrounding iron atom. 62</p> <p>3.30 High-temperature phase, crystal 4 62</p> <p>3.31 High-temperature phase, crystal 4 62</p> <p>3.32 Crystal 7 images 64</p> <p>3.33 Crystal 8 64</p> <p>3.34 Reconstructions of reciprocal space for crystal 9, room temperature 65</p> <p>3.35 <code>ReflectionConditionCheck</code> applied on crystal 9 65</p> <p>3.36 Inspection of lower temperatures, crystal 9 66</p> <p>4.1 Data reduction stuck on frame 7189. Version: 171.38.41 68</p>
-----------------------------------------------------------------------------------------------------------------------------------------------------------------------------------------------------------------------------------------------------------------------------------------------------------------------------------------------------------------------------------------------------------------------------------------------------------------------------------------------------------------------------------------------------------------------------------------------------------------------------------------------------------------------------------------------------------------------------------------------------------------------------------------------------------------------------------------------------------------------------------------------------------------------------------------------------------------------------------------------------------------------------------------------------------------------------------------------------------------------------------------------------------------------------------------------------------------------------------------------------------------------------------------------------------------------------------------------------------------------------------------------------------------------------------------------------------------------------------------------------------------------------------------------------------------------------------------------------------------------------------------------------------------------------------------------------------------------------------------------------------------------------------------------------------------------------------------------------------------------------------------------------------------------------------------------------------------------------------------------------------------------------------------------------------	----------------------------------------------------------------------------------------------------------------------------------------------------------------------------------------------------------------------------------------------------------------------------------------------------------------------------------------------------------------------------------------------------------------------------------------------------------------------------------------------------------------------------------------------------------------------------------------------------------------------------------------------------------------------------------------------------------------------------------------------------------------------------------------------------------------------------------------------------------------------------------------------------------------------------------------------------------------------------------------------------------------------------------------------------------------------------------------------------------------------------------------------------------------------------------------------------------------------------------------------------------------------------------------------------------------------------------------------------------------------------------------------------------------------------------------------------------------------------------------------------------------------------------------------------------------------------------------------------------------------------------------------------------------------------------------------------------------------------------------------------------------------------------------------------------------------------------------------------------------------------------------------------------------------------------------

4.2	Different results after data reduction on silicon	68	4.10	Rotation angles of crystal 9	73
4.3	Lattice parameters, crystal 1	70	4.11	Mosaicity parameters of crystals 1, 4 and 9	74
4.4	Rotation angles, crystal 1	70	5.1	Simulation of reciprocal space	76
4.5	Lattice parameters of crystal 4	71	6.1	Silicon intensities calculated by Thorkildsen's <i>Mathematica</i> function, sorted by mean intensity.	100
4.6	Rotation angles of crystal 4	71	6.2	The steps of <code>ReflectionConditionCheck</code>	101
4.7	Lattice parameters of crystal 4 (no presetting of instrument parameters)	72	6.3	8-connectedness	101
4.8	Rotation angles of crystal 4 (no presetting of instrument parameters)	72			
4.9	Lattice parameters of crystal 9	73			

List of tables

2.1	Data reduction output files	20	3.9	Data from the solution of ferrocene	45
2.2	<i>CrysAlis</i> symbols associated with the parameters of the instrument model and short descriptions.	23	3.10	Obverse–reverse twin reflection types	51
3.1	Structure factor comparison	33	3.11	Overview for where intermediate reflections appear.	55
3.2	Darwin width comparison	34	3.12	Overview for the complementary layers (hkl_1) and (hkl_2).	57
3.3	Silicon data setting comparison	35	3.13	Structure solution of crystal 4	61
3.4	Silicon sample descriptions	36	3.14	Crystal 7 lattice parameters	64
3.5	Thiourea-ferrocene data overview	38	3.15	Structure solution of crystal 9	67
3.6	Peak table data of reflection $\overline{125}$.	39	5.1	Characteristic observations of the reciprocal space at studied temperature transitions.	75
3.7	Refined instrument parameters. The best estimates will be used when setting the instrument model in advance.	40	6.1	Notes on crystals	97
3.8	Instrument parameters from room temperature data.	40	6.2	<i>CrysAlis</i> observations for crystal 1	99
			6.3	Before and after transformation, crystal 1	99

References

- [1] A. Authier, *Dynamical Theory of X-Ray Diffraction*. Oxford University Press, 2001.
- [2] F. H. Herbstein, *Crystalline Molecular Complexes and Compounds: Structures and Principles*. Oxford University Press, 2005.
- [3] M. Sorai, K. Ogasahara, and H. Suga, "Heat capacity and phase transitions of thiourea-ferrocene channel inclusion compound," *Molecular Crystals and Liquid Crystals*, vol. 73, no. 3-4, pp. 231–254, 1981. [Online]. Available: <http://dx.doi.org/10.1080/00268948108072337>
- [4] H. B. Larsen and G. Thorkildsen, "Fys620," 2015.
- [5] A. Authier, *Early Days of X-ray Crystallography*. Oxford University Press, 2013.
- [6] S. C. Wallwork. Introduction to the calculation of structure factors. [Online]. Available: <http://www.iucr.org/education/pamphlets/3/full-text>
- [7] A. Authier, S. Lagomarsino, and B. Tanner, *X-Ray and Neutron Dynamical Diffraction – Theory and Applications*, ser. Nato Science Series B. Springer US, 1996.
- [8] J. M. Cowley, *Diffraction Physics*, 3rd ed. Elsevier Science Pub Co., 12 1995.
- [9] X-ray_crystallography - wikipedia, the free encyclopedia. [Online]. Available: https://en.wikipedia.org/wiki/X-ray_crystallography
- [10] R. G. Driggers and C. Hoffman, Eds., *Encyclopedia of Optical Engineering*, 1st ed. CRC Press, 2003, vol. 3.
- [11] S.-L. Chang, *Multiple Diffraction of X-Rays in Crystals*. Springer-Verlag Berlin Heidelberg, 1984.
- [12] D. K. Bowen and B. K. Tanner, *High Resolution X-Ray Diffractometry And Topography*. CRC Press, February 1998.
- [13] B. K. Tanner, *X-Ray Diffraction Topography*. Pergamon Press, 1976, vol. 1st.
- [14] P. P. Ewald, "Introduction to the dynamical theory of x-ray diffraction," *Acta Crystallographica Section A*, vol. 25, no. 1, pp. 103–108, Jan 1969. [Online]. Available: <http://dx.doi.org/10.1107/S0567739469000155>
- [15] Anomalous absorption - online dictionary of crystallography. [Online]. Available: http://reference.iucr.org/dictionary/Anomalous_absorption
- [16] Dynamical theory - online dictionary of crystallography. [Online]. Available: http://reference.iucr.org/dictionary/Dynamical_theory
- [17] Z. G. Pinsker, *Dynamical Scattering of X-Rays in Crystals*, 1st ed. Springer-Verlag Berlin Heidelberg, 1978.
- [18] E. Zolotoyabko, *Basic Concepts of X-Ray Diffraction*. Wiley-VCH Verlag GmbH, 2014.
- [19] E. Hecht, *Schaum's Outline of Theory and Problems of Optics*, 1st ed. McGraw-Hill, 1975.
- [20] E. R. Pike and P. C. Sabatier, *Scattering, Two-Volume Set: Scattering and inverse scattering in Pure and Applied Science*, 1st ed. Academic Press, November 2001.
- [21] P. G. Radaelli, "Lecture 5 – scattering geometries," Clarendon Laboratory, Department of Physics, Oxford University.
- [22] Dynamical theory of diffraction - wikipedia, the free encyclopedia. [Online]. Available: https://en.wikipedia.org/wiki/Dynamical_theory_of_diffraction

- [23] Charles galton darwin - wikipedia, the free encyclopedia. [Online]. Available: https://en.wikipedia.org/wiki/Charles_Galton_Darwin
- [24] K. Lonsdale, "Extinction in x-ray crystallography," *Mineralogical Magazine*, vol. 28, no. 196, pp. 14–25, March 1947.
- [25] J. Als-Nielsen and D. McMorrow, *Elements of Modern X-ray Physics*, 2nd ed. Wiley, April 2011.
- [26] D. W. Bruce, D. O'Hare, and R. I. Walton, *Structure from Diffraction Methods*, 1st ed., ser. Inorganic Materials Series. Wiley, June 2014.
- [27] M. De Graef and M. E. McHenry, *Structure of Materials: An Introduction to Crystallography, Diffraction and Symmetry*. Cambridge University Press, 2007.
- [28] Reflection multiplicity. [Online]. Available: <http://pd.chem.ucl.ac.uk/pdnn/symm2/multj.htm>
- [29] (2016, February) Symmetry in crystallograph notes. [Online]. Available: <http://xrayweb.chem.ou.edu/notes/symmetry.html>
- [30] E. Martz, "Proteopedia, life in 3d." [Online]. Available: http://proteopedia.org/wiki/index.php/Resolution#What_Limits_Resolution.3F
- [31] checkif problem with 'completeness' - xrayforum.co.uk. [Online]. Available: <http://www.xrayforum.co.uk/viewtopic.php?t=1150>
- [32] J. Harp, "Biomolecular crystallography facility." [Online]. Available: <http://www.structbio.vanderbilt.edu/xray/tutorials/flash/mosaic.php>
- [33] Mosaicity - wikipedia, the free encyclopedia. [Online]. Available: <https://en.wikipedia.org/wiki/Mosaicity>
- [34] J. W. Pflugrath, "The finer things in X-ray diffraction data collection," *Acta Crystallographica Section D*, vol. 55, no. 10, pp. 1718–1725, Oct 1999. [Online]. Available: <http://dx.doi.org/10.1107/S090744499900935X>
- [35] Data collection. [Online]. Available: http://www-structmed.cimr.cam.ac.uk/Course/Basic_collection/Datacol.html
- [36] M. Reidulff, "Phase Stability and Point Defects in InMnO₃," Master's thesis, NTNU, 2014.
- [37] Phase transition - wikipedia, the free encyclopedia. [Online]. Available: https://en.wikipedia.org/wiki/Phase_transition
- [38] Glossary of tem terms | jeol ltd. [Online]. Available: <http://www.jeol.co.jp/en/words/emterms/>
- [39] "Structure determination - online dictionary of crystallography," April 2016. [Online]. Available: http://reference.iucr.org/dictionary/Structure_determination
- [40] J. P. Glusker and K. N. Trueblood, *Crystal Structure Analysis*, ser. IUCR Texts on Crystallography. Oxford University Press, July 2010, no. 14.
- [41] G. Thorkildsen and H. B. Larsen, "Absorption and Weighted Path Lengths in Cylinders and Spheres," *Acta Crystallographica Section A*, vol. 54, no. 2, pp. 186–190, Mar 1998. [Online]. Available: <http://dx.doi.org/10.1107/S0108767397012531>
- [42] D. Eisenberg and D. Crothers, *Physical Chemistry: with Applications to the Life Sciences*. The Benjamin–Cummings Publishing Company, 1979.
- [43] G. Oszlányi and A. Sütö, "The charge flipping algorithm," *Acta Crystallographica Section A*, vol. 64, no. 1, pp. 123–134, Jan 2008. [Online]. Available: <http://dx.doi.org/10.1107/S0108767307046028>
- [44] P. Müller, R. Herbst-Irmer, A. L. Spek, T. R. Schneider, and M. R. Sawaya, *Crystal Structure Refinement: A Crystallographer's Guide to SHELXL*, P. Müller, Ed. Oxford University Press, 2010.
- [45] G. M. Sheldrick, "SHELXT – Integrated space-group and crystal-structure determination," *Acta Crystallographica Section A*, vol. 71, no. 1, pp. 3–8, Jan 2015. [Online]. Available: <http://dx.doi.org/10.1107/S2053273314026370>

- [46] O. V. Dolomanov, L. J. Bourhis, R. J. Gildea, J. A. K. Howard, and H. Puschmann, “OLEX2: a complete structure solution, refinement and analysis program,” *Journal of Applied Crystallography*, vol. 42, no. 2, pp. 339–341, Apr 2009. [Online]. Available: <http://dx.doi.org/10.1107/S0021889808042726>
- [47] Rigaku Oxford Diffraction, (2015), *CrysAlisPro Software system, version 1.171.38.41*, Rigaku Corporation, Oxford, UK.
- [48] *CrysAlisPro Instruction Manual*, 5th ed., Rigaku Oxford Diffraction, Rigaku Corporation, 9009 New Trails Drive, The Woodlands, TX 77381, USA, December 2015.
- [49] G. M. Sheldrick. Shelxl instructions. [Online]. Available: http://shelx.uni-ac.gwdg.de/SHELX/shelxl_html.php#WGHT
- [50] Olex2, “Olex2 and the weighting scheme.” [Online]. Available: <https://www.youtube.com/watch?v=G1lhFU1ur4>
- [51] E. Bykova, “Single-crystal x-ray diffraction at extreme conditions in mineral physics and material sciences,” Ph.D. dissertation, Universität Bayreuth, 2015.
- [52] V. Dyadkin, P. Pattison, V. Dmitriev, and D. Chernyshov, “A new multipurpose diffractometer PILATUS@SNBL,” *Journal of Synchrotron Radiation*, vol. 23, no. 3, pp. 825–829, May 2016. [Online]. Available: <http://dx.doi.org/10.1107/S1600577516002411>
- [53] W. A. Paciorek, M. Meyer, and G. Chapuis, “On the geometry of a modern imaging diffractometer,” *Acta Crystallographica Section A*, vol. 55, no. 3, pp. 543–557, May 1999. [Online]. Available: <http://dx.doi.org/10.1107/S0108767398015037>
- [54] G. Thorkildsen and H. B. Larsen, “Angle calculations for the huber kappa-goniometer and the pilatus pixel detector at the swiss-norwegian beamlines [draft],” Department of Mathematics and Natural Science, Stavanger University, N-4036 Stavanger, Norway, September 2015.
- [55] E. Prince, *Mathematical Techniques in Crystallography and Materials Science*, 2nd ed. Springer Berlin Heidelberg, 1994.
- [56] W. R. Busing and H. A. Levy, “Angle calculations for 3- and 4-circle X-ray and neutron diffractometers,” *Acta Crystallographica*, vol. 22, no. 4, pp. 457–464, Apr 1967. [Online]. Available: <http://dx.doi.org/10.1107/S0365110X67000970>
- [57] T. Higashi, “The processing of diffraction data taken on a screenless Weissenberg camera for macromolecular crystallography,” *Journal of Applied Crystallography*, vol. 22, no. 1, pp. 9–18, Feb 1989. [Online]. Available: <http://dx.doi.org/10.1107/S0021889888009562>
- [58] “Kappa goniometers series 515.” [Online]. Available: <http://www.xhuber.de/en/product-groups/1-positioning-devices/12-rotation/kappa-goniometers/>
- [59] S. Brockhauser, R. B. G. Ravelli, and A. A. McCarthy, “The use of a mini- κ goniometer head in macromolecular crystallography diffraction experiments,” *Acta Crystallographica Section D*, vol. 69, no. 7, pp. 1241–1251, Jul 2013. [Online]. Available: <http://dx.doi.org/10.1107/S0907444913003880>
- [60] G. S. Henderson, D. R. Neuville, and R. T. Downs, Eds., *Spectroscopic Methods in Mineralogy and Material Sciences*, ser. Reviews in Mineralogy and Geochemistry. Walter de Gruyter, November 2014, no. 78.
- [61] J. M. Mancheño, “Some notes on x-ray diffraction data collection,” May 2014.
- [62] D. W. Bennett, *Understanding Single-Crystal X-Ray Crystallography*. Wiley-VCH Verlag GmbH, 2010.
- [63] V. Dyadkin, *SNBL Toolbox Swiss-Norwegian Beam Lines at the ESRF, version 0.5*, Grenoble, France.
- [64] Ferrocene - wikipedia, the free encyclopedia. [Online]. Available: <https://en.wikipedia.org/wiki/Ferrocene>
- [65] S. A. Miller, J. A. Tebboth, and J. F. Tremaine, “114. dicyclopentadienylyron,” *J. Chem. Soc.*, pp. 632–635, 1952. [Online]. Available: <http://dx.doi.org/10.1039/JR9520000632>
- [66] Fulvalene - wikipedia, the free encyclopedia. [Online]. Available: <https://en.wikipedia.org/wiki/Fulvalene>

- [67] (2014, July) Milestone 10 : Nature milestones in crystallography. [Online]. Available: <http://www.nature.com/milestones/milecrystal/full/milecrystal10.html>
- [68] Metallocene - wikipedia, the free encyclopedia. [Online]. Available: <https://en.wikipedia.org/wiki/Metallocene>
- [69] J. D. Dunitz, L. E. Orgel, and A. Rich, "The crystal structure of ferrocene," *Acta Crystallographica*, vol. 9, no. 4, pp. 373–375, Apr 1956. [Online]. Available: <http://dx.doi.org/10.1107/S0365110X56001091>
- [70] J. W. Edwards, G. L. Kington, and R. Mason, "The thermodynamic properties of ferrocene. part 1.-the low-temperature transition in ferrocene crystals," *Trans. Faraday Soc.*, vol. 56, pp. 660–667, 1960. [Online]. Available: <http://dx.doi.org/10.1039/TF9605600660>
- [71] B. T. M. Willis, "Three-dimensional neutron diffraction study of ferrocene," *Acta Crystallographica*, vol. 13, no. 12, p. 1088, Dec 1960. [Online]. Available: <http://dx.doi.org/10.1107/S0365110X60002430>
- [72] T. F. Koetzle, *Chemical crystallography at the High Flux Beam Reactor*, Jan 1978. [Online]. Available: <http://www.osti.gov/scitech/servlets/purl/6781848>
- [73] F. Takusagawa and T. F. Koetzle, "A neutron diffraction study of the crystal structure of ferrocene," *Acta Crystallographica Section B*, vol. 35, no. 5, pp. 1074–1081, May 1979. [Online]. Available: <http://dx.doi.org/10.1107/S0567740879005604>
- [74] D. Paliwoda, K. Kowalska, M. Hanfland, and A. Katrusiak, "U-turn compression to a new isostructural ferrocene phase," *The Journal of Physical Chemistry Letters*, vol. 4, no. 23, pp. 4032–4037, 2013. [Online]. Available: <http://dx.doi.org/10.1021/jz402254b>
- [75] P. Seiler and J. D. Dunitz, "A new interpretation of the disordered crystal structure of ferrocene," *Acta Crystallographica Section B*, vol. 35, no. 5, pp. 1068–1074, May 1979. [Online]. Available: <http://dx.doi.org/10.1107/S0567740879005598>
- [76] P. Seiler and J. D. Dunitz, "Low-temperature crystallization of orthorhombic ferrocene: structure analysis at 98 K," *Acta Crystallographica Section B*, vol. 38, no. 6, pp. 1741–1745, Jun 1982. [Online]. Available: <http://dx.doi.org/10.1107/S0567740882007080>
- [77] J. Berár, G. Calvarin, D. Weigel, K. Chhor, and C. Pommier, "New low-temperature crystalline phase of ferrocene: Isomorphous to orthorhombic ruthenocene," *The Journal of Chemical Physics*, vol. 73, no. 1, pp. 438–441, 1980. [Online]. Available: <http://scitation.aip.org/content/aip/journal/jcp/73/1/10.1063/1.439894>
- [78] P. Štěpnička, *Ferrocenes: Ligands, Materials and Biomolecules*. John Wiley & Sons, Ltd., 2008.
- [79] J. M. Bermudez-Garcia, S. Yanez-Vilar, S. Castro-Garcia, M. A. Senaris-Rodriguez, and M. Sanchez-Andujar, "New properties in old systems: cooperative electric order in ferrocene and ammonia-borane," *RSC Adv.*, vol. 5, pp. 83 818–83 824, 2015. [Online]. Available: <http://dx.doi.org/10.1039/C5RA12506E>
- [80] F. J. Zuñiga, G. Madariaga, W. A. Paciorek, J. M. Pérez-Mato, J. M. Ezpeleta, and I. Etxebarria, "Modulated structure of thiourea," *Acta Crystallographica Section B*, vol. 45, no. 6, pp. 566–576, Dec 1989. [Online]. Available: <http://dx.doi.org/10.1107/S0108768189007846>
- [81] I. Takahashi, A. Onodera, and Y. Shiozaki, "Structural changes of thiourea in connection with its phase transitions: reappraisal of rigidity and libration of the molecule," *Acta Crystallographica Section B*, vol. 46, no. 5, pp. 661–664, Oct 1990. [Online]. Available: <http://dx.doi.org/10.1107/S0108768190006012>
- [82] K. D. M. Harris, "Meldola lecture: understanding the properties of urea and thiourea inclusion compounds," *Chem. Soc. Rev.*, vol. 26, pp. 279–289, 1997. [Online]. Available: <http://dx.doi.org/10.1039/CS9972600279>
- [83] M. D. Lowery, R. J. Wittebort, M. Sorai, and D. N. Hendrickson, "Dynamics of ferrocene in a thiourea inclusion matrix," *Journal of the American Chemical Society*, vol. 112, pp. 4214–4225, May 1990.

- [84] E. Hough and D. G. Nicholson, "X-ray crystallographic studies on ferrocene included in a thiourea host lattice," *J. Chem. Soc., Dalton Trans.*, pp. 15–18, 1978. [Online]. Available: <http://dx.doi.org/10.1039/DT9780000015>
- [85] M. G. B. Drew, A. Lund, and D. G. Nicholson, "Molecular modelling studies on the thiourea/ ferrocene clathrate," *Supramolecular Chemistry*, vol. 8, no. 3, pp. 197–212, 1997. [Online]. Available: <http://dx.doi.org/10.1080/10610279708034937>
- [86] T. C. Gibb, "Anisotropic relaxation of the electric field gradient tensor in the 57 fe mossbauer spectra of a thiourea-ferrocene clathrate," *Journal of Physics C: Solid State Physics*, vol. 9, no. 13, p. 2627, 1976. [Online]. Available: <http://stacks.iop.org/0022-3719/9/i=13/a=022>
- [87] R. Clement, R. Claude, and C. Mazieres, "Clathration of ferrocene and nickelocene in a thiourea host lattice," *J. Chem. Soc., Chem. Commun.*, pp. 654–655, 1974. [Online]. Available: <http://dx.doi.org/10.1039/C39740000654>
- [88] Cornell university chess database. [Online]. Available: <http://www.chess.cornell.edu/oldchess/operatns/xrclcdwn.htm>
- [89] E. Prince, Ed., *Mathematical, Physical and Chemical Tables*, 3rd ed., ser. International Tables for Crystallography. Kluwer Academic Publishers, 2004, vol. C.
- [90] D. Waasmaier and A. Kirfel, "New analytical scattering-factor functions for free atoms and ions," *Acta Crystallographica Section A*, vol. 51, no. 3, pp. 416–431, May 1995.
- [91] D. T. Cromer and D. A. Liberman, "Anomalous dispersion calculations near to and on the long-wavelength side of an absorption edge," *Acta Crystallographica Section A*, vol. 37, no. 2, pp. 267–268, Mar 1981. [Online]. Available: <http://dx.doi.org/10.1107/S0567739481000600>
- [92] T. Hahn, Ed., *Space-Group Symmetry*, 5th ed., ser. International Tables for Crystallography. Kluwer Academic Publishers, 2002, vol. A.
- [93] "Twinning - ccp4 wiki." [Online]. Available: http://strucbio.biologie.uni-konstanz.de/ccp4wiki/index.php/Twinning#Twinning_by_Reticular_Merohedry
- [94] R. Herbst-Irmer and G. M. Sheldrick, "Refinement of obverse/reverse twins," *Acta Crystallographica Section B*, vol. 58, no. 3 Part 2, pp. 477–481, Jun 2002. [Online]. Available: <http://dx.doi.org/10.1107/S0108768102001039>
- [95] Pixel connectivity - wikipedia, the free encyclopedia. [Online]. Available: https://en.wikipedia.org/wiki/Pixel_connectivity
- [96] M. M. Julian, *Foundations of Crystallography with Computer Applications*, 2nd ed. CRC Press Inc., October 2014.

Index

Symbols

8-connected 101

A

absorption 14
absorption factor 17
affine transformation 101
Anregungspunkt *see* tie point
asymmetry ratio 13
atomic form/scattering factor 7

B

binning (data) 41
black box 68
Bloch wave 10
Born approximation 7
Borrmann fan 9
Bragg angle 8
Bragg's law 8, 8

C

centrosymmetric 16
channel *see* tunnel inclusion compound
charge flipping 18
clathrate compound 30
coarse (rotational increment) 16
completeness 16
continuous phase transition *see* second-order phase transition
Cp *see* cyclopentadienyl
CrysAlis 5, 21, 98
Crysis *see* SNBL ToolBox
cyclopentadienyl 29

D

Darwin plateau 13
Darwin width 8, 13, 14
data reduction 19, 27
data subset 21
dielectric susceptibility 10
direct methods 17
discrepancy index *see* *R*-factor
dispersion surface 12
dual space methods 18
dynamical theory of diffraction 10
 fundamental equations 11

E

eclipsed conformation 29
electric dipole radiation 6
electron density distribution 7
estimated standard deviation *see* standard uncertainty
Ewald sphere 7
Ewald's construction 8
external standard deviation 40
extinction distance 13
extinction factor 17

F

ferrocene 29

fine (rotational increment) 16
first-order phase transition 17
Fourier method 18
Friedel pair 103
Friedel's law 16
full reflection 16
fundamental equations 11

G

geometrical theory 7
Glycyl-L-alanine 5
Grundgleichungen
 *see* fundamental equations
guest *see* inclusion compound

H

host *see* inclusion compound

I

ideally imperfect crystal 9
inclusion compound 30
incommensurate structure 17
index of refraction 12
indexing (diffraction pattern) 16
instrument centre 23
interplanar spacing 8

K

kinematical approximation 7
kinematical theory of diffraction 7

L

laboratory frame 23
Laue class 16
Laue point 12
Lorentz point 12
Lorentz-polarisation correction 17

M

Max von Laue 7
merging residual value 18
metallocene 29
metric tensor (of reciprocal space) 33
modulated crystal structure 17
mosaic crystal 9
mosaicity 16
multiple scattering 9

O

Olex2 45
optical field 10
order of reflection 8
order-disorder transition 17
orientation matrix 21
orthogonal rotation matrix 21
orthonormalisation matrix 21
outlier (reflection) 16

P

partial reflection 16

Patterson function 17
Patterson synthesis 18
peak table 25
Pendellung effect 14
Pendellösung distance 8, 13
pentfulvalene 29
permeability 12
permittivity 12
phase transition 17
phase velocity 12
PILATUS 21
primary extinction 9, 14

Q

Q (peak) 45

R

R-factor 18
reciprocal lattice vector 7
reciprocal space metric tensor 21
redundancy 16
reflection (spot on diffraction pattern) 16
reliability index *see* *R*-factor
residual factor *see* *R*-factor
residual factor (intensities) 26
resolution 16
resolution sphere 18
resonance factors 11
reticular merohedry 50
rotation (oscillation) method 21

S

sandwich compounds 29
satellite reflection 17
scattering
 scattering process 6
scattering coefficient 33
scattering length 6
scattering vector 6
second-order phase transition 17
secondary extinction 14
secondary extinction extinction 9
SHELXL 18
SHELXS 18, 45
SHELXT 18
SNBL ToolBox 21
SNBL Toolbox 28
soft host 30
solving the structure *see* structure determination
 sphere of reflection *see* Ewald sphere
staggered conformation 29
standard uncertainty 18
structure determination 17
structure factor 7
superlattice 17
Swiss-Norwegian beamline 21

T

thick (diffractogram) 16

thin	16
thiourea	30
thiourea-ferrocene	30
tie point	10
transformation matrix	101
tunnel inclusion complex	30
twisted conformation	29
two-beam case	11

U	
um c	47
unique reflection	16
unit cell	6
unwarp	27
urea	30
V	
versatile host	30

W	
wave field	10
wave vector	10
wavelet	6, 10
weighted mean	40
weighting scheme	19
X	
XPREP	20
xx monitorinifromrunlist	42

